

Four-hundred Very Metal-Poor Stars Studied with LAMOST and Subaru. II. Elemental abundances

HAINING LI,¹ WAKO AOKI,^{2,3} TADAFUMI MATSUNO,^{4,3,2} QIANFAN XING,⁵ TAKUMA SUDA,⁶
NOZOMU TOMINAGA,^{2,3,7,8} YUQIN CHEN,⁵ SATOSHI HONDA,⁹ MIHO N. ISHIGAKI,² JIANRONG SHI,⁵
JINGKUN ZHAO,⁵ AND GANG ZHAO⁵

¹*Key Lab of Optical Astronomy, National Astronomical Observatories, Chinese Academy of Sciences (CAS)*

A20 Datun Road, Chaoyang, Beijing 100101, China

²*National Astronomical Observatory of Japan*

2-21-1 Osawa, Mitaka, Tokyo 181-8588, Japan

³*Department of Astronomical Science, School of Physical Sciences, The Graduate University of Advanced Studies (SOKENDAI)*

2-21-1 Osawa, Mitaka, Tokyo 181-8588, Japan

⁴*Kapteyn Astronomical Institute, University of Groningen*

Landleven 12, 9747 AD Groningen, The Netherlands

⁵*Key Lab of Optical Astronomy, National Astronomical Observatories, Chinese Academy of Sciences*

A20 Datun Road, Chaoyang, Beijing 100101, China

⁶*Department of Liberal Arts, Tokyo University of Technology, Nishi Kamata 5-23-22, Ota-ku, Tokyo 144-8535, Japan*

⁷*Department of Physics, Faculty of Science and Engineering, Konan University*

8-9-1 Okamoto, Kobe, Hyogo 658-8501, Japan

⁸*Kavli Institute for the Physics and Mathematics of the Universe (WPI), The University of Tokyo, 5-1-5*

Kashiwanoha, Kashiwa, Chiba 277-8583, Japan

⁹*Nishi-Harima Astronomical Observatory, Center for Astronomy, University of Hyogo*

407-2, Nishigaichi, Sayo-cho, Sayo, Hyogo 679-5313, Japan

(Received; Revised; Accepted)

Submitted to ApJ

ABSTRACT

We present homogeneous abundance analysis of over 20 elements for 385 very metal-poor (VMP) stars based on the LAMOST survey and follow-up observations with the Subaru Telescope. It is the largest high-resolution VMP sample (including 363 new objects) studied by a single program, and the first attempt to accurately determine evolutionary stages for such a large sample based on *Gaia* parallaxes. The sample covers a wide metallicity range from $[\text{Fe}/\text{H}] \lesssim -1.7$ down to $[\text{Fe}/\text{H}] \sim -4.3$, including over 110 objects with $[\text{Fe}/\text{H}] \leq -3.0$. The expanded coverage in evolutionary status makes it possible to define abundance trends respectively for giants and turnoff stars. The newly obtained abundance data confirm most abundance trends found by previous studies, but also provide useful update and new sample of outliers. The Li plateau is seen in

$-2.5 < [\text{Fe}/\text{H}] < -1.7$ in our sample, whereas the average Li abundance is clearly lower at lower metallicity. Mg, Si, and Ca are overabundant with respect to Fe, showing decreasing trend with increasing metallicity. Comparisons with chemical evolution models indicate that the over-abundance of Ti, Sc, and Co are not well reproduced by current theoretical predictions. Correlations are seen between Sc and α -elements, while Zn shows a detectable correlation only with Ti but not with other α -elements. The fraction of carbon-enhanced stars ($[\text{C}/\text{Fe}] > 0.7$) is in the range of 20 – 30% for turnoff stars depending on the treatment of objects for which C abundance is not determined, which is much higher than that in giants ($\sim 8\%$). Twelve Mg-poor stars ($[\text{Mg}/\text{Fe}] < 0.0$) have been identified in a wide metallicity range from $[\text{Fe}/\text{H}] \sim -3.8$ through -1.7 . Twelve Eu-rich stars ($[\text{Eu}/\text{Fe}] > 1.0$) have been discovered in $-3.4 < [\text{Fe}/\text{H}] < -2.0$, enlarging the sample of r-process-enhanced stars with relatively high metallicity.

Keywords: methods: data analysis — stars: Population II — stars: abundance

1. INTRODUCTION

Stars lacking metals have long been regarded as fossil records of the early evolution of the Galaxy and preserve important clues to the first generation of stars in the universe. Low-metallicity stars with $[\text{Fe}/\text{H}] < -2.0$, -3.0 , and -4.0 ¹ are referred to as very metal-poor (VMP), extremely metal-poor (EMP), and ultra metal-poor (UMP) stars, respectively (Beers & Christlieb 2005). Detailed chemical abundance patterns of these objects can be compared to theoretical models and constrain the nucleosynthesis of early generations of supernovae (Nomoto et al. 2013), while their observed abundance trends along metallicities provide essential information about the chemical history of the Milky Way (Frebel & Norris 2015). Extending the overall abundance analysis to a large sample of VMP and EMP stars allow us to examine nucleosynthetic yields to constrain the detailed physics of these events, such as progenitor stellar masses, rotation rates, masses of the compact remnant (neutron stars or black holes), explosion energies, mixing efficiencies of ejecta, etc. (Heger & Woosley 2010; Limongi & Chieffi 2012; Tominaga et al. 2014; Limongi & Chieffi 2018; Wanajo 2018; Jones et al. 2019). These yields are important for understanding the chemical enrichment and initial condition of the early Milky Way.

In the past two decades, abundance patterns of VMP/EMP stars have been studied extensively through high-resolution spectroscopic observations for several hundred VMP stars, including the samples of First Stars (Cayrel et al. 2004; Bonifacio et al. 2009) (hereafter FS), the Most Metal-poor Stars (Norris et al. 2013; Yong et al. 2013) (hereafter Y13), and other follow-up studies on metal-poor stars selected from survey projects (e.g., Barklem et al. 2005; Aoki et al. 2013a; Cohen et al. 2013; Roederer et al. 2014; Jacobson et al. 2015). Such analyses have led to better understanding about the abundance trends of VMP stars, and also obtained a number of important discoveries such as first discoveries of hyper metal-poor stars with metallicities below $[\text{Fe}/\text{H}] \sim -5.0$ (Christlieb et al. 2002; Frebel et al. 2005), objects with unprecedentedly low iron abundance of $[\text{Fe}/\text{H}] < -7.0$ (Keller et al. 2014) or total metal content (Caffau et al. 2011), and stars with extreme abundance patterns.

¹ The standard notations $[X/Y] = \log(N_X/N_Y) - \log(N_X/N_Y)_\odot$ and $\log A(X) = \log(N_X/N_H) + 12$ for elements X and Y are adopted in this work.

Meanwhile, larger number of VMP/EMP stars have made us realize that there exists a large scatter in the observed elemental abundance ratios among these old stars, indicating rather stochastic chemical enrichment at the early stage. An example is the large fraction of carbon-enhanced metal-poor (CEMP) stars that do not present enhancement in heavy elements, i.e., CEMP-no stars (Aoki et al. 2002). Dominating the most metal-poor stars, the surface abundances of the majority of CEMP-no stars are believed to reflect the abundances of natal gas where they were born. However, the origin of the carbon-excess in these stars are still in debate, with proposed scenarios including rotating massive stars (Maeder et al. 2015), faint supernova (Umeda & Nomoto 2005), and inhomogeneous metal-mixing (Hartwig & Yoshida 2019). Enhancement of carbon by binary mass transfer from the former AGB stars in which s-process is not efficient is also proposed (Suda et al. 2004). More recent observations have revealed that some CEMP-no stars can also be enhanced in intermediate-mass elements such as Na, Mg, Al, Si, etc. (e.g., Bonifacio et al. 2018; Aoki et al. 2018), which could be a useful constraint on the mechanisms that produce the C enhancement in CEMP-no stars. Another sign of stochastic chemical enrichment is the discovery of VMP/EMP stars showing clearly lower $[\alpha/\text{Fe}]$ ratios compared to the typical halo stars (Cohen et al. 2013; Caffau et al. 2013; Bonifacio et al. 2018). Some objects could have been enriched by more than one first generation of supernova (Hartwig et al. 2019; Salvadori et al. 2019). A possible signature of supernovae by very massive stars is also suggested (Aoki et al. 2014).

The above mentioned remarkable abundance patterns observed in VMP/EMP stars are usually considered as typical features of ultra-faint dwarf galaxies and some classical dwarf galaxies (Tolstoy et al. 2009; Venn et al. 2012; Salvadori et al. 2015). Increasing evidence for accretion of small stellar systems in the formation of the Milky Way halo has indeed been obtained; stellar streams such as Sagittarius stream (Ibata et al. 1994) and kinematic substructures including Gaia-Enceladus, Sequoia, Thamnos, and the Helmi streams are considered to be signatures of past galaxy accretions (e.g., Helmi et al. 1999, 2018; Koppelman et al. 2019). However, most of these systems have mean metallicities with $[\text{Fe}/\text{H}] > -2.0$ (e.g., Naidu et al. 2020; Zhao & Chen 2021; Ruiz-Lara et al. 2022), and the presence of the aforementioned kinematic substructures is less prominent at metallicities below $[\text{Fe}/\text{H}] \sim -2.0$ (see e.g., Fig. 2 of Myeong et al. 2018). Though there have been a few studies on (limited number of stars in) substructures with lower metallicities (e.g., Roederer & Gnedin 2019; Yuan et al. 2020; Aguado et al. 2021), the assembly history of VMP/EMP stars is still far less clear compared to stars with $[\text{Fe}/\text{H}] > -2.0$. Interestingly, Sestito et al. (2019) has found out that some ultra metal-poor stars orbit close to or within the plane of the Galactic disk, which has been later on confirmed with a much larger VMP star sample (Sestito et al. 2020), and is reproduced by high-resolution cosmological simulations (Sestito et al. 2021). Such observations raise challenge to the conventional models where metal-poor stars should be much older than the Galactic plane. Hereby, after the launching of *Gaia* mission (Gaia Collaboration et al. 2016), combination of spectroscopic observations and accurate parallax and proper motions provided by *Gaia* have made it possible to investigate the chemo-dynamical structure and evolution of the Milky Way in more detail, through multi-dimensional database of VMP/EMP stars.

For previous studies that have focused on VMP/EMP stars, the number of program stars studied by individual work is usually from about a few dozens to at most a few hundred, which is still much smaller than the sample of stars with higher metallicity (i.e., disk stars) measured by recent large spectroscopic surveys (e.g., Gaia/ESO survey: Gilmore et al. 2012, GALAH: De Silva et al.

2015). Detailed chemical abundances of VMP stars have been provided by more recent efforts such as the R -Process Alliance (RPA, Holmbeck et al. 2020) and high-resolution follow-up observations of the Pristine survey (e.g., Venn et al. 2020) and the SkyMapper survey (e.g., Jacobson et al. 2015; Yong et al. 2021a). However, the samples of VMP stars in these studies include a few dozen to over one hundred VMP stars, e.g., about 150 VMP stars in the RPA database. Hence, a large sample of homogeneously observed and analyzed VMP stars are very much in need.

Decades of studies have allowed us to recognize that the most metal-poor stars are rare objects to find, and thus studies of chemical abundances of VMP and EMP stars have to take advantages from wide field spectroscopic surveys. Such efforts include the early objective prism surveys such as the HK Survey (Beers et al. 1985, 1992) and the Hamburg/ESO Survey (Christlieb et al. 2008), low-resolution spectroscopic surveys (e.g., SEGUE, the Sloan Extension for Galactic Understanding and Exploration; Yanny et al. 2009), and photometric survey projects including the SkyMapper survey (Keller et al. 2007) and the Pristine survey (Starkenburg et al. 2017). However, existing candidate samples are either limited in their number of stars, or comprise stars that are too faint for efficient high-resolution follow-up spectroscopy with 4-10 meter telescopes. As a result, the number of EMP/UMP stars with high-resolution follow-up is still not sufficiently large for statistical investigations of the most metal-poor stars.

LAMOST (Large sky Area Multi-Object fiber Spectroscopic Telescope)² has completed its first five-year low-resolution spectroscopic survey from 2012 through 2017 (LAMOST-I), and released more than seven million spectra of stars in the Milky Way in its fifth data release (DR5). This huge database of spectra provides a great opportunity to explore the various stellar components of the Galaxy (Zhao et al. 2006, 2012; Liu et al. 2015), including searches for VMP stars over a large area of sky. One advantage of the LAMOST sample of stars is that they cover a range in apparent magnitude suitable for efficient follow-up high-resolution spectroscopic observations with 4–10 meter telescopes. In addition, the wavelength coverage (3700 – 9100 Å) and resolving power ($R \sim 1800$) of LAMOST spectra allow for quite reliable estimation of the stellar parameters including effective temperatures and metallicities. The LAMOST database has been provided a great opportunity to search for large number of VMP stars (Aguado et al. 2017; Li et al. 2015c, 2018b).

To further extend previous efforts and obtain a large homogeneous sample of VMP stars, a joint project was initiated to obtain high-resolution spectra for over 400 VMP star candidates selected from the LAMOST survey, using the High Dispersion Spectrograph (HDS) equipped at the Subaru Telescope. The “snapshot” spectra with $R = 36,000$ have been obtained for the main sample, while for a few interesting objects with $[\text{Fe}/\text{H}] < -4.0$ or with peculiar elemental abundances, spectra with higher SNR and/or resolving power ($R = 60,000$) were then obtained for more detailed analysis, e.g., for two UMP stars (Li et al. 2015a), a bright EMP r-II star (Li et al. 2015b), etc.

Detailed description about target selection and observations of the LAMOST/Subaru VMP sample is provided in Aoki et al. (hereafter Paper I), in which radial velocities and interstellar reddening are also reported. This is the second paper of the series, presenting a homogeneous chemical abundance analysis for this LAMOST/Subaru VMP star sample. The outline of the paper is as follows: analysis of stellar parameters as well as elemental abundances are described in § 2, interpretations about the abundance results including the observed abundance trend, and comparison with theoretical models

² <http://www.lamost.org/public/>

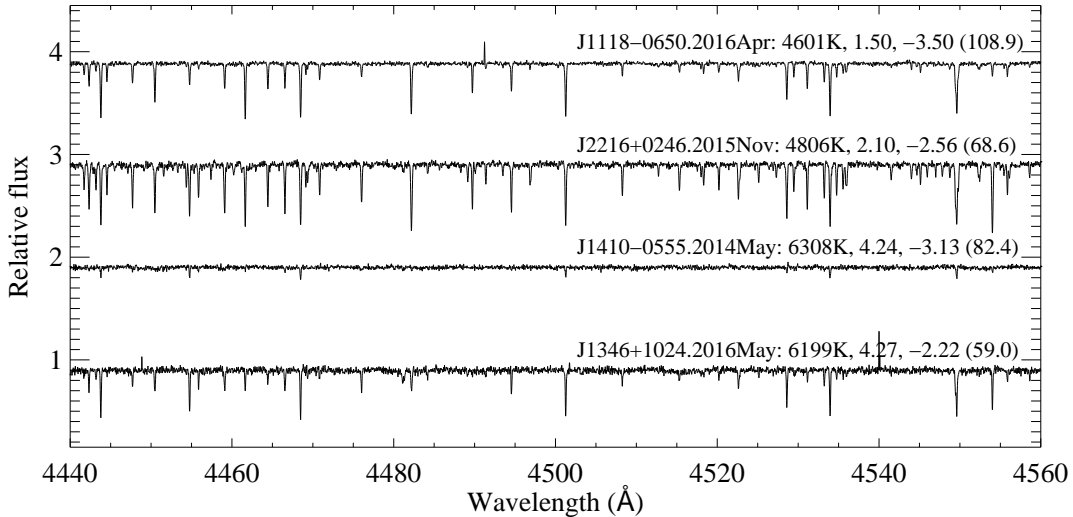


Figure 1. Four normalized Subaru/HDS spectra nearby 4500 Å, from top to bottom respectively for EMP red giant, VMP red giant, EMP turnoff, and VMP turnoff stars. Stellar parameters (T_{eff} , $\log g$, and $[\text{Fe}/\text{H}]$) for each object have been labelled with the object name, and corresponding spectral SNR has also been shown in parenthesis.

are presented in § 3, which also includes discussions on various categories of chemically peculiar objects. A brief summary is given in § 4.

2. OBSERVATIONS AND ANALYSIS OF PROGRAM STARS

The program stars were first selected from LAMOST DR1 through DR5. More than 15,000 candidates of VMP stars have been initially selected based on metallicities derived from LAMOST low-resolution spectra out of over 4.9 million spectra with signal-to-noise ratio (SNR) higher than 15 in the g -band, using two independent methods, i.e., template matching of observed flux and line index matching (readers may refer to Li et al. (2018b) for more details). To focus on relatively bright (e.g., $g < 13.0$) VMP targets or most probable EMP candidates ($[\text{Fe}/\text{H}] < -3.0$ derived in both methods), over 400 of the above VMP candidates were selected for high-resolution followed-up observation using the Subaru/HDS. The obtained “snapshot” spectra with $R = 36,000$ cover a wavelength coverage of 4000–6800 Å, which were taken with exposure times of 10–20 minutes in most cases during seven observing runs from May 2014 to August 2017. Readers can find more details about the sample and observations in Paper I. The original sample includes 420 objects (with 445 spectra). In order to obtain sufficient spectral quality to derive reliable parameters and elemental abundances, spectra with SNR higher than 10 per pixel (~ 25 per resolution element) around 4500 Å, or those in which more than 10 Fe I lines are detected, have been selected for the following analysis. This results in 411 spectra (385 unique stars) for estimation of stellar parameters and elemental abundances. Figure 1 shows sample Subaru/HDS spectra for four program stars, respectively representing VMP and EMP red giants, and also VMP and EMP turnoff stars.

2.1. Equivalent width measurements

The equivalent widths (EWs) of atomic lines were then measured for all 411 selected spectra, based on a linelist compiled from literature (Aoki et al. 2013b, and Mashonkina et al. 2010), fitting

Table 1. Literatures for the comparison purpose

	EW ^a	T_{eff} ^b	$\log g$ ^c	Figures ^d
Cayrel et al. (2004)	G	phot.	ion.	2 & 10
Honda et al. (2004a,b)	G	phot.	ion.	11
Lai et al. (2008)	V	phot.	iso.	2 & 10
Hollek et al. (2011)	V	ex.	ion.	2 & 11
Cohen et al. (2013)	G	phot.	iso.+ion.	2 & 10
Li et al. (2015a)	G	ex.	ion.	11
Matsuno et al. (2017b)	G	Balmer	Balmer	11
Sakari et al. (2018)	G	ex.	ion.	2 & 11
Li et al. (2018a)	G	ex.	ion.	12

A summary of the methods adopted in literatures.

^aG: Gaussian profile is assumed for equivalent widths measurements. V: Voigt profiles are assumed for a part of the lines.

^bThe method of temperature determination. phot: photometric temperature, ex.: temperature from excitation balance of neutral iron lines, Balmer: temperature from Balmer line profiles.

^cThe method of $\log g$ determination. ion.: $\log g$ from ionization balance between neutral and singly-ionized iron, iso.: $\log g$ estimated using relations between T_{eff} and $\log g$ from isochrones, Balmer: $\log g$ from Balmer line profiles.

^dReference to figures that compare equivalent widths, and stellar parameters and abundances.

^e(3D) NLTE correction by Amarsi et al. (2016) was applied.

a Gaussian profile for corresponding single and unblended atomic absorption lines using an IDL code Tame (Kang & Lee 2012).

There have been 26 targets observed more than once in our program. Their spectra could be useful to check the consistency of the reduced spectra taken under different condition, stability of our EW measurements, and the measurement uncertainty in EWs due to noise. The systematic offset between multiple EW measurements is negligible (no larger than 0.03 mÅ), demonstrating the consistency of the reduced spectra and our EW measurements. The scatter is usually smaller than 0.20 mÅ, which is comparable to the typical uncertainty of EW measurements.

Figures 2 shows comparisons of EWs measured in the present work with literature that has more than two stars in common with our study (Table 1). Note that some studies adopt Voigt profile fitting, while others assume Gaussian profiles for all the lines. This information is also included in Table 1. In general, there is a good agreement between our measurements and those from literature.

Two stars that are in common with Sakari et al. (2018) show small but significant offset in EWs ($\frac{|\langle \Delta \log \text{EW} \rangle|}{\sigma(\Delta \log \text{EW})/\sqrt{N}} > 8$) for both stars. The difference is seen over the entire wavelength range. We note that we did not find any sign of problems on sky subtraction during the visual inspection of

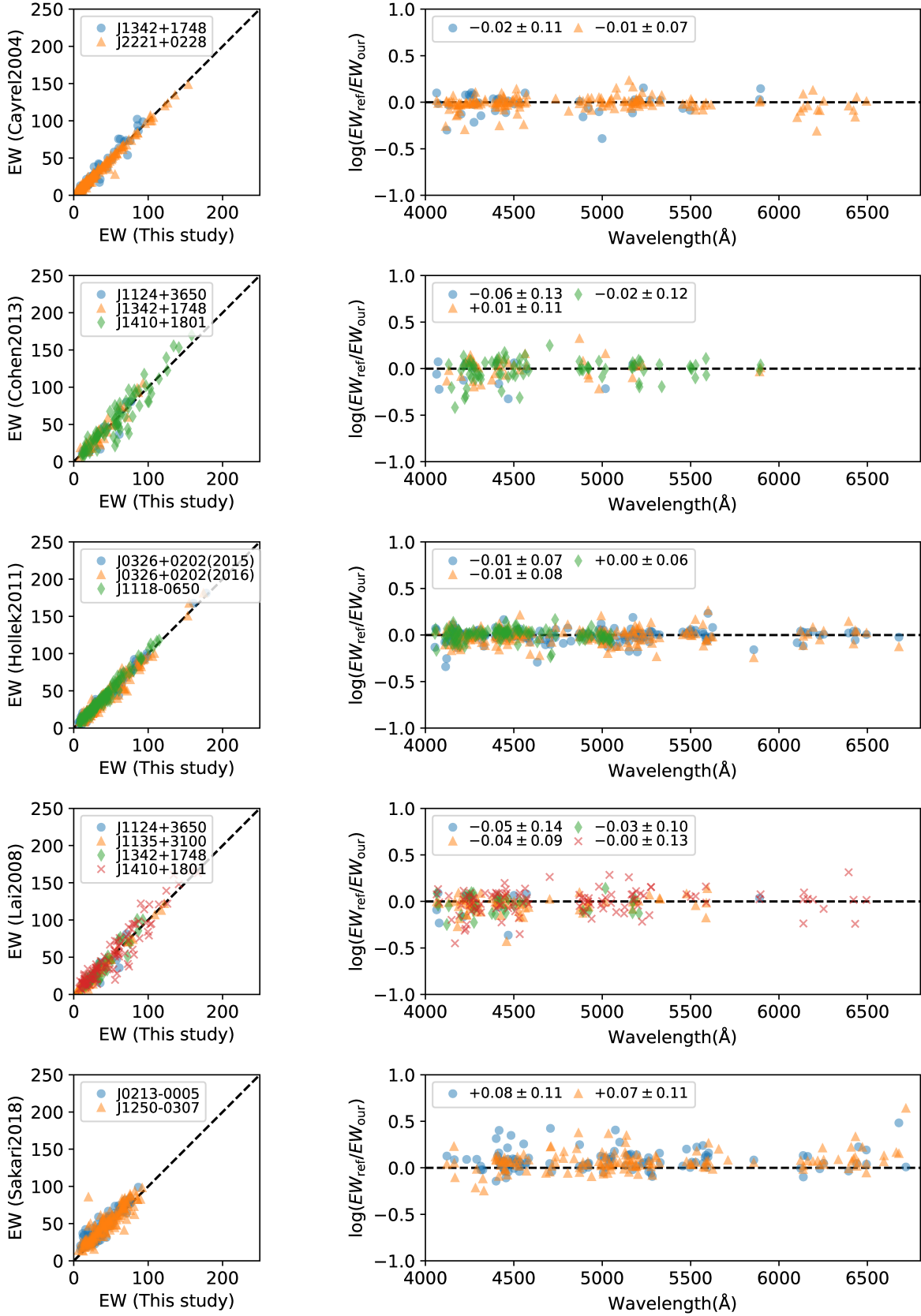


Figure 2. Comparison of equivalent widths between our study and literature. The literature was selected to have more than one star in common with our study. The average logarithmic difference of equivalent widths and the standard deviation are presented in the right panels.

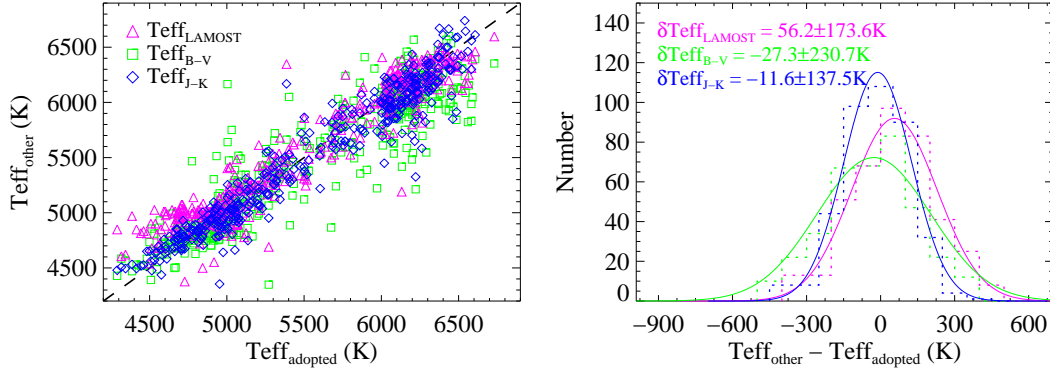


Figure 3. Left: Comparison between the adopted T_{eff} and those derived from LAMOST spectra (pink triangles), and that based on $(J - K)_0$ (blue diamonds) and $(B - V)_0$ (green squares). The one-to-one line is plotted for reference. Right: Distribution of the T_{eff} difference, together with a best-fit Gaussian to indicate the typical difference and scatter. Same colors to the left panel are used for the three sets of T_{eff} measurements.

the reduced spectra for the two objects. We also note that our measured equivalent widths are in agreement with other studies ($\frac{|\langle \Delta \log \text{EW} \rangle|}{\sigma(\Delta \log \text{EW})/\sqrt{N}} < 5$).

2.2. Determination of stellar parameters

In Paper I, we describe high-resolution spectroscopic observations of over 400 program stars obtained using Subaru/HDS, including sample selection, radial velocity measurements, and discussion on binarity. Our sample consists of 363 newly discovered and analyzed metal-poor stars, together with 22 objects whose abundances have already been published in previous studies.

Since our sample covers a relatively wide metallicity range and evolutionary status, we have adopted the calibration for effective temperatures from Alonso et al. (1996) and Alonso et al. (1999), based on the dereddened color $(V - K)_0$, obtained from V magnitude coming from APASS, K magnitude transformed from 2MASS K_s , and the extinction estimated from Green (2018). These data are given in Paper I. The T_{eff} estimated from different colors are compared in Figure 3. We find good correlations between the adopted T_{eff} and those from colors with offset about 50 K or less. The scatter is large for the T_{eff} from $B - V$, which is most sensitive to the metallicity and molecular features.

It is known that the Fe abundances derived from Fe I lines can suffer relatively large NLTE (e.g., Amarsi et al. 2016), and that the number of Fe II lines could be very limited in spectra of VMP stars, which makes it difficult to derive the surface gravity by forcing the Fe I and Fe II lines to result in consistent Fe abundance. Therefore, we adopt the surface gravity derived using parallax data for our sample when reliable data are available.

For 315 objects, the $\log g$ are derived from reliable parallax ($\text{err_parallax}/\text{parallax} < 0.2$) measurements by Gaia DR2 (Gaia Collaboration et al. 2018), based on the following equation:

$$\log g = \log g_{\odot} + \log \frac{M}{M_{\odot}} + 4 \log \frac{T_{\text{eff}}}{T_{\text{eff}\odot}} + 0.4(M_{\text{bol}} - M_{\text{bol}\odot}) \quad (1)$$

where M_{bol} refers to the bolometric magnitude, and a fixed stellar mass of $0.8 M_{\odot}$ has been adopted for our calculation. Quantitative tests have shown that adopting different stellar mass for each object would only result in a 0.01 difference in $\log g$ on average.

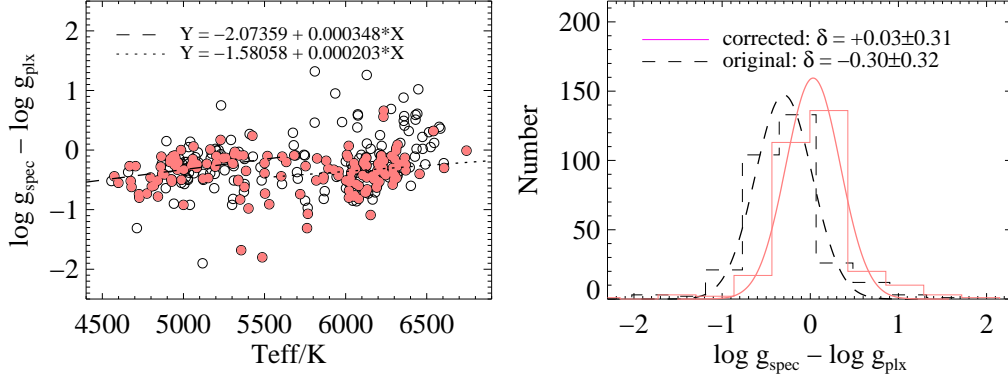


Figure 4. Left: The difference between the spectroscopic $\log g_{\text{spec}}$ and parallax-derived $\log g_{\text{plx}}$ along T_{eff} for all 315 objects which have reliable parallax measurements. Open circles indicate objects with lower spectral quality ($S/N < 50$), while filled circles for objects with $S/N > 50$. The $\log g$ corrections are derived by linear fitting to the data in two T_{eff} ranges (dashed and dotted lines). Right: Distribution of the difference between $\log g_{\text{plx}}$ vs $\log g_{\text{spec}}$ (dashed) and the corrected $\log g$ (solid) for all 315 objects which have reliable parallax measurements. Gaussian profile has been fit to estimate the typical difference and scatter.

For the rest of the sample for which Gaia DR2 have not provided (reliable) parallax measurements, the $\log g$ were first determined using the spectroscopic method, i.e., forcing the Fe I and Fe II lines to derive similar iron abundances, and then the spectroscopic $\log g$ ($\log g_{\text{spec}}$) were corrected to the parallax-derived scale adopting the following procedure. Using the 315 objects which have reliable parallax-derived $\log g$, the correction is determined by linear fittings of the difference between their $\log g_{\text{spec}}$ and the parallax-derived $\log g_{\text{plx}}$ as a function of T_{eff} . As shown in the left panel of Fig. 4, the correction is separately fitted by cooler (giant) stars and warmer (turnoff) stars, respectively covering $T_{\text{eff}} < 5700$ K (dashed line) and $T_{\text{eff}} > 5300$ K (dotted line). For objects located in the overlapping region $5300 \text{ K} < T_{\text{eff}} < 5700 \text{ K}$, an average of the corrected $\log g$ has been adopted. We note that only spectra with SNR higher than 50 (filled circles) are used in the fitting to derive the correction, which ensures reliable measurements of iron lines (especially Fe II) and thus robust $\log g_{\text{spec}}$. It can be seen from the right panel of Fig. 4 that the systematic offset between $\log g_{\text{spec}}$ and $\log g_{\text{plx}}$ has been removed after the correction, whereas the dispersion does not change significantly.

The dependence of the $\log g$ difference (before correction) has been examined against the other two atmospheric parameters, i.e., $\log g$ and $[\text{Fe}/\text{H}]$, as presented in Figure 5. No distinct correlation with either parameter is found, confirming that the adopted $\log g$ correction is applicable to objects with various evolutionary status and metallicities. It is noticed that slightly larger difference between the two sets of $\log g$ is found for EMP turnoff stars with relatively lower S/N spectra (open circles). This is an expected result, as the number of Fe II lines significantly decreases for warmer objects or those with lower metallicities, which leads to larger uncertainties of the spectroscopically derived $\log g_{\text{spec}}$.

After deriving the empirical $\log g$ correction, it has been adopted to the $\log g_{\text{spec}}$ measured from the 70 objects that do not have $\log g_{\text{plx}}$, so as to obtain their final $\log g$ values. The distribution of the final adopted T_{eff} and $\log g$ of the whole sample are shown in Figure 6. It can be seen that the majority of the 70 objects for which the $\log g$ correction has been adopted are located on the giant branch, i.e., they are more distant objects and thus do not have (reliable) parallax measurements compared with relatively nearby turnoff stars. In general, adopting the final stellar parameters,

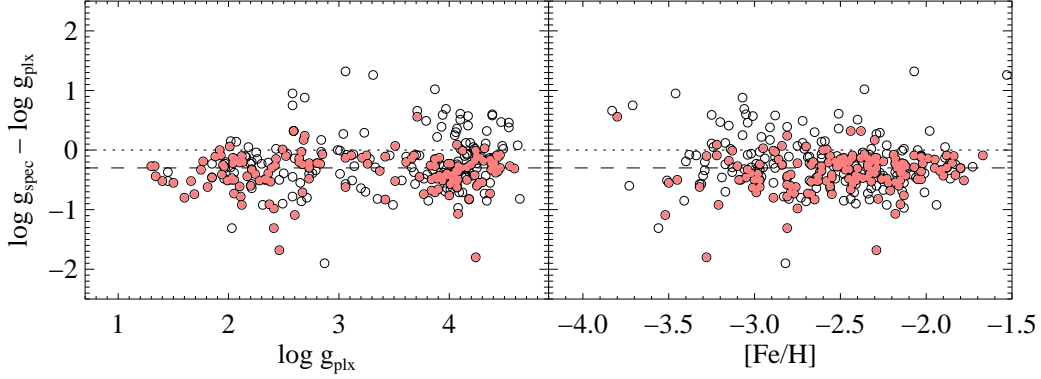


Figure 5. Variation of the difference between the parallax-derived and spectroscopic $\log g$ along different $\log g$ (left) and metallicity (right) for all program stars with reliable parallax measurements. Symbols are the same as in Figure 4. The dotted and dashed lines refer to a zero difference and the average difference, respectively, between the two sets of $\log g$ for our sample.

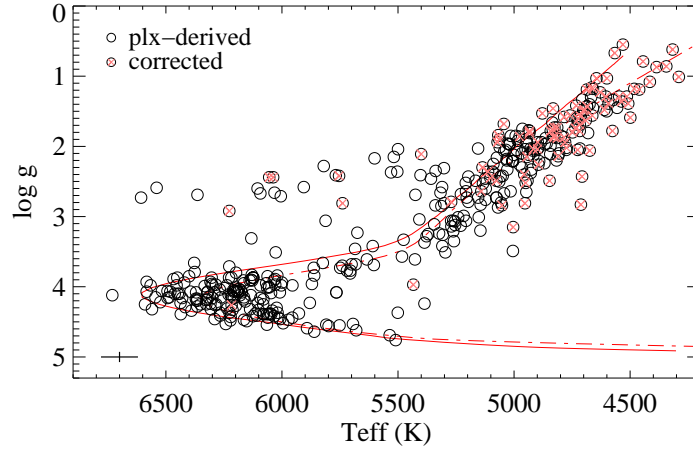


Figure 6. The distribution of the program stars in the T_{eff} vs. $\log g$ diagram. Open circles refer to the 315 objects with $\log g$ derived from the Gaia parallax, while circle+crosses represent targets with $\log g$ derived from the empirical corrections as described in the text. The solid and dashed-dotted lines respectively stand for the Y^2 isochrone for $[\text{Fe}/\text{H}] = -3.0$ and -2.0 .

stars align on the theoretical isochrone (the solid and dashed lines in Figure 6), confirming robust estimation of parameters and the effective correction on $\log g$.

Since the number of measured Fe I lines of the analyzed sample stars (10–170 lines) is significantly larger than that of Fe II (0–20 lines), the average abundance obtained from Fe I lines is adopted as the final value of the metallicity. The resulted metallicities confirm that over 93% of the measured objects are with $[\text{Fe}/\text{H}] < -2.0$. The remaining 7% objects are still metal-poor, e.g., the median and average metallicities of these objects are -1.86 and -1.79 , respectively, and there is only one exception with $[\text{Fe}/\text{H}] > -1.5$. Most of these less metal-poor (7%) objects are turnoff stars, for which estimation based on low-resolution spectra tends to underestimate metallicities compared to giants. The overall result demonstrates the reliability in the estimation of metallicities based on

LAMOST low-resolution spectra, which enables a quite efficient selection of targets for the follow-up high-resolution spectroscopy with the Subaru Telescope. The microturbulence velocities of all program stars have been derived using the traditional spectroscopic method, i.e., by forcing Fe I lines with different equivalent widths to result in similar iron abundances. With the above stellar parameters derived, the luminosity is then estimated for each objects based on: $\log L = \log L_{\odot} - (\log g - \log g_{\odot}) + (\log M - \log M_{\odot}) + 4(\log T_{\text{eff}} - \log T_{\text{eff}\odot})$, where the final $\log g$ (parallax-derived plus spectroscopic-corrected) values have been adopted (Table 2).

Table 2. Basic information and stellar Parameters of the Program Stars.

ID	Observational info.				Adopted parameters (Subaru measurement)											LAMOST measurement		
	R.A. deg.	Decl. deg.	RV km s ⁻¹	SNR ^a	T_{eff} K	σT_{eff} K	$\log g$	$\sigma \log g$	[Fe/H]	σ [Fe/H]	ξ km s ⁻¹	$\sigma \xi$ km s ⁻¹	$\log(L/L_{\odot})$	$\sigma \log(L/L_{\odot})$	$f_{\log g}^b$	T_{eff} (K)	$\log g$	[Fe/H]
J0002+0343	0.645994	3.727085	-91.4	23.7	6207	110	4.16	0.05	-3.02	0.24	1.19	0.30	0.307	0.060	plx	6361	4.30	-3.4
J0003+1556	0.795383	15.933828	-185.5	32.2	5302	45	2.31	0.08	-2.23	0.11	2.11	0.12	1.883	0.081	plx	5289	1.09	-2.6
J0006+0123	1.657593	1.395354	-65.9	44.1	5675	53	3.23	0.04	-2.27	0.11	1.52	0.08	1.081	0.043	plx	5500	2.52	-2.6
J0006+1057	1.571676	10.961624	-312.4	20.9	4691	38	1.63	0.14	-3.15	0.14	2.51	0.11	2.350	0.140	spec	5012	1.72	-3.2
J0013+2350	3.463742	23.846972	-259.2	41.4	6093	120	3.98	0.04	-2.26	0.09	1.49	0.10	0.455	0.054	plx	6238	3.91	-2.2
J0022+4254	5.510848	42.916500	-183.3	23.2	6566	133	3.98	0.06	-2.99	0.25	0.96	0.30	0.585	0.072	plx	6250	4.04	-3.4
J0023+2023	5.795711	20.392651	-126.0	37.3	5197	68	2.79	0.05	-3.29	0.09	1.53	0.11	1.368	0.054	plx	5250	2.55	-3.1
J0023+3558	5.916771	35.967957	-303.0	38.0	5145	82	3.20	0.06	-2.56	0.09	1.35	0.08	0.941	0.065	plx	4960	3.36	-3.1
J0025+2305	6.432368	23.093561	-229.6	48.3	6308	144	3.93	0.04	-2.81	0.10	1.99	0.17	0.565	0.059	plx	6152	3.26	-3.4

^aThe SNR is estimated from the normalized Subaru/HDS spectra around 4500 Å.

^bFlag of estimation of $\log g$, where “plx” refers to program stars whose $\log g$ have been estimated based on the reliable parallax, while “spec” refers to those based on empirical correction from the spectroscopic estimation. See the main text in § 2 for details.

NOTE—The table is published in its entirety in the machine-readable format. A portion is shown here for guidance regarding its form and content.

We have estimated the uncertainty of stellar parameters for individual spectra, which are presented in Table 2 together with the final adopted stellar parameters. The uncertainty of the T_{eff} has been derived from propagation of errors which mainly include photometric uncertainties in V and K magnitudes, and uncertainty in extinction estimations. The uncertainty of the $\log g$ could be divided into two categories: for those with parallax-derived $\log g$, the uncertainty has been estimated from error propagation of Equation 1, which mainly comes from the uncertainty of parallax measurements and photometry, and also includes uncertainties of T_{eff} . The typical uncertainty of parallax-derived $\log g$ is about 0.07 dex. Note that we have adopted a fixed stellar mass of $0.8 M_{\odot}$, which may result in another ~ 0.04 dex uncertainty in the derived $\log g$ if a 10% uncertainty in the stellar mass is adopted. For objects whose $\log g$ is derived from the corrected spectroscopic estimation, the uncertainty (on average 0.19 dex) comes from the scatter of abundances derived from Fe II lines (especially in cases with less than 8 Fe II lines), the non-negligible NLTE effect on abundances derived from Fe I lines for VMP stars, and the uncertainty from the empirical correction (shown in Figure 4) of the adopted $\log g$.

2.3. Elemental abundances

With EWs and stellar parameters obtained above, elemental abundances were then derived for the program stars. For abundance analysis of all species, the 1D plane-parallel, hydrostatic model atmospheres of the ATLAS NEWODF grid of Castelli & Kurucz (2003) has been adopted, assuming a mixing-length parameter of $\alpha_{\text{MLT}} = 1.25$, no convective overshooting, and local thermodynamic equilibrium (LTE). This grid of model atmospheres is also applied to the analysis of carbon-enhanced metal-poor stars in our sample. The impact of carbon-excess on 1D model atmospheres is not significant in main sequence turnoff stars and relatively warm red giants where molecular features are not strong, whereas it could be large in 3D models (Gallagher et al. 2017). Christlieb et al. (2004) investigate the effect of non-solar abundance ratios on model atmospheres for their study of the hyper metal-poor star HE 0107–5240 with large carbon-excess. They discuss that the effect of abundance changes is not very significant for stars with extremely low metallicity, because of the dominant role of hydrogen as opacity source and electron donor (see also Collet et al. 2006). Our sample includes a few cool giants with relatively high metallicity and carbon abundances, for which analysis using model atmospheres with carbon excess might be useful to derive more accurate abundances in future work. We use an updated version of the abundance analysis code MOOG (Snedden 1973), which treats continuous scattering as a source function which sums both absorption and scattering (Sobeck et al. 2011).

The lithium and carbon abundances of the program stars were respectively derived by matching the synthetic spectra of Li I 6707.8 Å doublet and the CH A-X band around 4300–4330 Å to the observed ones. The Li subordinate line at 6103.6 Å was used in cases of extremely Li-enhanced objects.

For 19 other elements (Na, Mg, Si, Ca, Sc, Ti, V, Cr, Mn, Fe, Co, Ni, Zn, Sr, Y, Zr, Ba, La, and Eu), the abundances were computed from the measured equivalent widths using model atmospheres (see below) with the derived stellar parameters. If the elemental abundance was derived from a single line, or if the derived abundances deviated by more than 3σ from the average values computed for an atomic species from multiple lines, the abundances were examined with spectral synthesis. For most of the used lines, synthetic spectra with abundances derived from the measured equivalent widths match the observed spectra well. However, for lines that suffer from blending or problems in setting the continuum level, the observed spectral line was not properly reproduced by synthetic spectra with

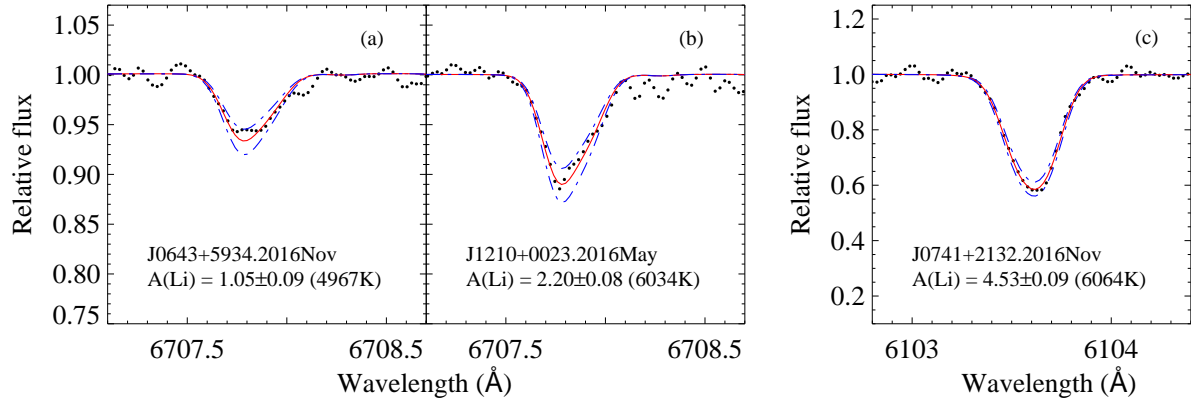


Figure 7. Examples of spectral fitting of Li 6708 Å line for a giant (a) and for a turnoff star (b) which present normal lithium abundances, and of Li 6103 Å line for a Li-rich star (c) whose Li 6708 Å line becomes saturated under LTE models. The observed spectrum is shown with dots, and the best fit and 1σ uncertainty has been respectively shown in solid and dashed lines.

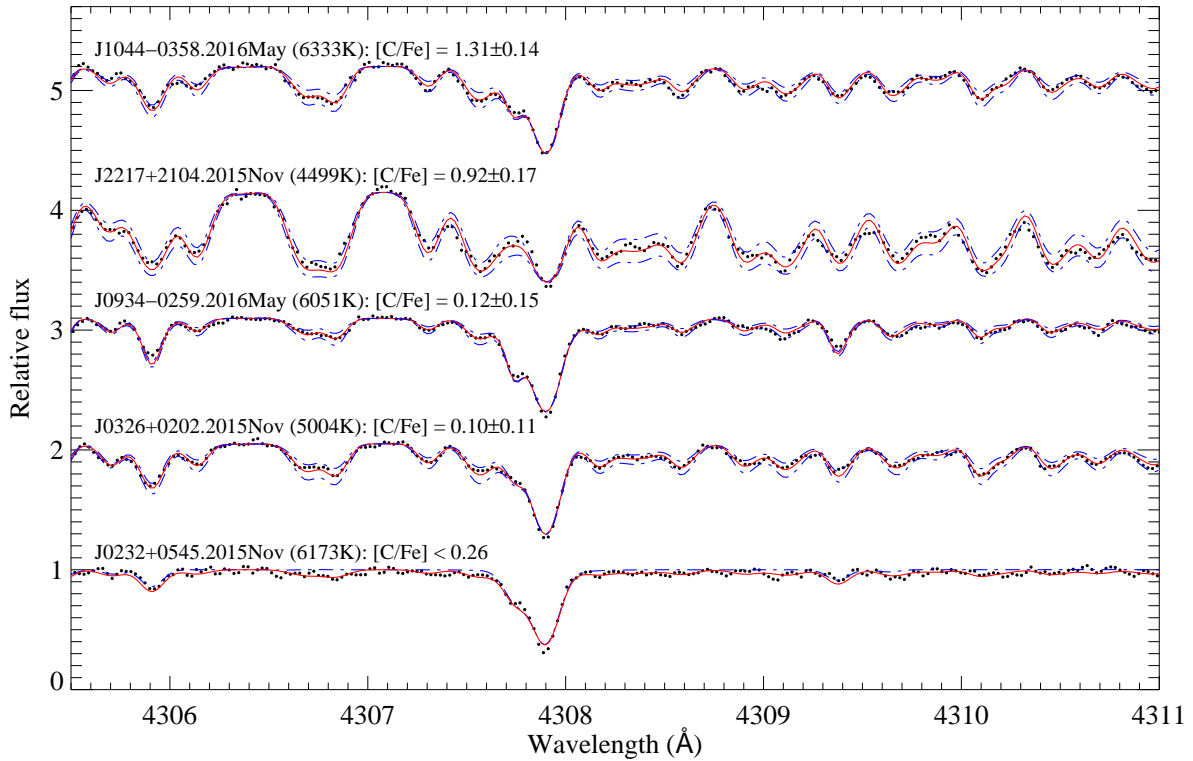


Figure 8. Examples of spectral fitting of the CH-band around 4310 Å. The top four spectra respectively represent CEMP (turnoff and giant) and non-CEMP (turnoff and giant). Definition of symbols are the same as Figure 7. The bottom spectrum shows the upper limit (solid line), while the dashed line stands for the case with no carbon.

the abundance derived from equivalent widths. In such cases, the abundance derived from spectral synthesis was adopted. Hyper-fine structure and isotopic splitting have been considered for Sr, Ba, La, and Eu (Borghs et al. 1983; McWilliam et al. 1995; Lawler et al. 2001a,b). Note that the above mentioned analysis is expected to be subject to systematic uncertainties from NLTE effects. The NLTE effects on spectral features will be studied by more detailed analysis for a sub-sample with relatively high-SNR in a separate work of the series.

The derived abundances (upper-limits) of the program stars are listed in Table 3, which also includes the number of lines that have been used for deriving the abundance, N , together with the abundance error as described in the following text. The photospheric solar abundances of Asplund et al. (2009) are adopted when calculating the $[X/Fe]$ abundance ratios.

2.4. Abundances uncertainties

The errors of the derived abundances of the sample were estimated from two aspects: the uncertainties in measurements and in the determination of stellar parameters. The error due to the uncertainty of measurement was estimated from the standard deviation σ_X of abundances derived from individual lines and the number of lines N_X , as $\sigma_X/\sqrt{N_X}$. This estimate provides a kind of random error also including the uncertainties of gf values of spectral lines. When the number of adopted atomic lines is smaller than four, the larger of $\sigma_X/\sqrt{N_X}$ and $\sigma(\text{FeI})/\sqrt{N_X}$ was then adopted. The columns of $\sigma(N)$ and N in Table 3 standard deviation of abundances derived from individual lines and the number of adopted lines for corresponding species.

The abundance errors due to uncertainties of the stellar parameters were estimated from changes of abundances by individually varying T_{eff} , $\log g$, and $[\text{Fe}/\text{H}]$ according to 1σ parameter uncertainties. In Table 3, columns σT_{eff} , $\sigma \log g$, $\sigma[\text{Fe}/\text{H}]$, and $\sigma \xi$ summarize corresponding quantities in abundance $[X/Fe]$ uncertainties for the program stars, and the total error derived by adding individual errors in quadrature is given in the column of “Total”. We note that the effect of σT_{eff} more or less cancels in $[X/\text{H}]$ and $[\text{Fe}/\text{H}]$ in many cases, resulting in smaller errors in $[X/Fe]$ than that in $[\text{Fe}/\text{H}]$.

Table 3. Abundances and abundance error estimations for six sample stars

J1346+1024 (plx_logg, TO VMP)										J0934-0108 (plx_logg, RGB VMP)								
Ion	log ϵ (X)	[X/Fe]	σT_{eff} 77 K	$\sigma \log g$ 0.02	σ [Fe/H] 0.10	$\sigma \xi$ 0.12 km s $^{-1}$	σ (N)	Total	N	log ϵ (X)	[X/Fe]	σT_{eff} 44 K	$\sigma \log g$ 0.04	σ [Fe/H] 0.09	$\sigma \xi$ 0.05 km s $^{-1}$	σ (N)	Total	N
LiI	2.21	...	-0.01	-0.00	-0.00	0.01	0.10	0.10	1	1.00	...	0.00	0.00	0.00	0.01	0.09	0.09	1
C	6.51	0.30	0.09	-0.00	0.02	0.01	0.10	0.14	1	6.17	0.08	0.04	-0.01	0.02	0.01	0.09	0.10	1
NaI	3.91	-0.11	0.01	-0.01	-0.00	-0.03	0.07	0.08	2	3.68	-0.22	0.01	-0.01	0.00	-0.01	0.06	0.07	2
MgI	5.80	0.42	-0.01	-0.00	-0.00	-0.00	0.10	0.10	8	5.50	0.24	-0.02	0.00	0.00	-0.00	0.09	0.09	5
SiI	0	5.71	0.54	0.00	0.00	0.00	-0.01	0.09	0.09	1
CaI	4.53	0.41	-0.01	-0.00	0.01	0.01	0.09	0.09	23	4.27	0.27	-0.02	0.00	0.00	0.00	0.08	0.08	24
ScII	1.17	0.24	-0.02	0.01	0.01	0.00	0.14	0.14	10	1.00	0.19	-0.03	0.02	0.01	0.00	0.11	0.12	11
TiII	3.31	0.58	-0.03	0.01	-0.00	-0.01	0.13	0.13	28	2.98	0.37	-0.03	0.01	0.01	-0.01	0.10	0.11	33
VI	0	1.59	-0.00	0.00	0.00	0.00	0.01	0.09	0.09	1
CrI	3.26	-0.16	0.01	-0.00	0.01	-0.01	0.09	0.09	6	3.05	-0.25	0.00	-0.01	0.00	-0.01	0.05	0.05	10
MnI	0	2.64	-0.45	-0.01	0.00	0.00	0.01	0.05	0.05	3
FeI	5.28	0.00	-0.00	-0.00	-0.00	-0.00	0.10	0.10	107	5.16	-0.00	0.00	0.00	0.00	0.00	0.09	0.09	159
FeII	5.47	0.19	-0.05	0.01	-0.00	-0.00	0.13	0.14	11	5.25	0.09	-0.05	0.01	0.00	-0.00	0.10	0.11	17
CoI	2.99	0.22	0.01	-0.00	-0.00	0.00	0.07	0.07	2	3.01	0.36	0.00	-0.01	0.00	-0.02	0.05	0.06	3
NiI	4.15	0.15	-0.01	-0.00	0.01	0.01	0.23	0.23	3	3.88	0.00	-0.01	0.00	0.00	0.01	0.09	0.09	14
ZnI	0	2.41	0.19	-0.04	0.01	0.00	0.01	0.06	0.08	2
SrII	1.08	0.43	-0.00	-0.00	-0.00	-0.07	0.16	0.17	2	0.46	-0.07	-0.01	0.00	0.00	-0.03	0.13	0.13	2
YII	0.23	0.24	-0.03	-0.00	-0.00	0.00	0.16	0.16	2	-0.51	-0.38	-0.03	0.01	0.01	0.00	0.14	0.14	2
ZrII	0	0.24	0.00	-0.02	0.02	0.01	0.01	0.06	0.07	2
BaII	-0.02	0.02	-0.01	-0.00	-0.00	-0.03	0.08	0.09	3	-0.37	-0.21	-0.01	0.01	0.01	-0.01	0.04	0.04	4
LaII	0	-0.90	0.34	-0.02	0.01	0.01	0.01	0.26	0.26	3
EuII	0	-1.35	0.47	-0.02	0.02	0.01	0.01	0.06	0.07	2
J1410-0555 (plx_logg, TO EMP)										J1733+2633 (plx_logg, RGB EMP)								
Ion	log ϵ (X)	[X/Fe]	σT_{eff} 80 K	$\sigma \log g$ 0.02	σ [Fe/H] 0.14	$\sigma \xi$ 0.20 km s $^{-1}$	σ (N)	Total	N	log ϵ (X)	[X/Fe]	σT_{eff} 45 K	$\sigma \log g$ 0.04	σ [Fe/H] 0.11	$\sigma \xi$ 0.10 km s $^{-1}$	σ (N)	Total	N
LiI	2.13	...	-0.01	0.00	0.00	0.02	0.14	0.14	1	0.96	...	0.00	0.00	0.00	0.02	0.11	0.11	1
C	6.97	1.67	0.07	0.00	0.02	0.02	0.14	0.16	1	5.58	0.43	0.04	-0.01	0.02	0.02	0.11	0.12	1
NaI	3.45	0.34	0.00	0.00	0.01	-0.02	0.10	0.10	2	2.60	-0.36	-0.01	0.00	0.00	0.00	0.08	0.08	2
MgI	5.38	0.91	-0.01	0.00	0.00	0.00	0.09	0.09	6	4.93	0.61	-0.01	-0.01	0.00	0.00	0.09	0.09	6

Table 3 continued on next page

Table 3 (continued)

SiI	0	5.00	0.77	0.00	0.00	0.01	0.02	0.11	0.11	1
CaI	3.63	0.42	-0.02	0.00	0.00	0.01	0.19	0.19	9	3.42	0.36	-0.02	0.00	0.00	0.01	0.12	0.12	13
ScII	0.46	0.44	-0.02	0.01	0.00	0.01	0.23	0.23	2	0.24	0.37	-0.03	0.01	0.00	0.00	0.08	0.09	9
TiII	2.12	0.30	-0.03	0.00	0.00	0.01	0.14	0.14	10	2.06	0.39	-0.02	0.01	0.01	0.01	0.11	0.11	24
VI	0	0
CrI	2.28	-0.23	0.00	0.00	0.00	0.01	0.12	0.12	5	1.96	-0.40	0.01	0.00	0.01	0.00	0.08	0.08	5
MnI	0	0
FeI	4.37	0.00	0.00	0.00	0.00	0.00	0.14	0.14	42	4.22	-0.00	0.00	0.00	0.00	0.00	0.11	0.11	95
FeII	4.39	0.02	-0.05	0.00	0.00	0.01	0.18	0.19	4	4.25	0.03	-0.04	0.02	0.01	0.02	0.11	0.12	12
CoI	2.53	0.67	0.01	0.00	0.01	0.02	0.10	0.10	2	2.01	0.30	0.01	-0.01	0.00	0.01	0.09	0.09	2
NiI	0	2.88	-0.06	0.00	0.00	0.00	0.01	0.11	0.11	1
ZnI	0	0
SrII	-0.11	0.15	-0.01	0.01	0.00	-0.03	0.10	0.10	2	-1.12	-0.71	-0.01	0.01	0.00	-0.01	0.08	0.08	2
YII	0	0
ZrII	0	0
BaII	-1.05	-0.10	-0.01	0.01	0.01	0.02	0.10	0.10	2	-2.22	-1.12	-0.01	0.01	0.01	0.02	0.08	0.08	2
LaII	0	0
EuII	0	0
J1432+3755 (corrected_logg, RGB EMP)										J1102+0102 (corrected_logg, RGB VMP)								
Ion	log ϵ (X)	[X/Fe]	σT_{eff} 24 K	$\sigma \log g$ 0.05	σ [Fe/H] 0.14	$\sigma \xi$ 0.10 km s $^{-1}$	σ (N)	Total	N	log ϵ (X)	[X/Fe]	σT_{eff} 45 K	$\sigma \log g$ 0.07	σ [Fe/H] 0.09	$\sigma \xi$ 0.05 km s $^{-1}$	σ (N)	Total	N
LiI	0	0.99	...	0.01	0.00	0.00	0.01	0.09	0.09	1
C	4.95	-0.25	0.04	-0.10	0.02	0.01	0.14	0.18	1	6.08	-0.03	0.04	-0.09	0.03	0.01	0.09	0.14	1
NaI	3.12	0.11	-0.00	-0.01	-0.01	-0.05	0.10	0.11	2	4.20	0.28	0.02	-0.02	0.01	-0.00	0.09	0.09	2
MgI	4.86	0.49	-0.01	-0.01	-0.01	-0.01	0.12	0.12	8	5.48	0.20	-0.02	-0.01	-0.01	-0.00	0.09	0.09	6
SiI	4.83	0.55	-0.01	-0.01	-0.01	-0.01	0.14	0.14	1	5.43	0.24	0.00	0.00	0.00	-0.01	0.09	0.09	1
CaI	3.43	0.32	-0.01	-0.01	0.00	-0.00	0.09	0.09	17	4.22	0.20	-0.02	0.00	0.00	0.00	0.10	0.10	23
ScII	0.00	0.08	-0.02	0.01	0.00	-0.01	0.10	0.10	12	0.98	0.15	-0.03	0.02	0.01	0.00	0.12	0.13	13
TiII	2.06	0.34	-0.02	0.01	0.00	-0.02	0.11	0.11	32	3.07	0.44	-0.04	0.02	0.01	-0.01	0.14	0.15	33
VI	0.64	-0.06	-0.00	0.00	0.00	0.01	0.14	0.14	1	1.47	-0.14	0.01	0.00	0.00	0.01	0.09	0.09	1
CrI	2.11	-0.30	-0.00	-0.01	-0.01	-0.01	0.17	0.17	9	3.06	-0.26	0.01	-0.01	-0.01	-0.01	0.09	0.09	10
MnI	1.79	-0.41	-0.00	0.00	0.00	0.01	0.11	0.11	2	2.57	-0.54	0.00	0.00	0.00	0.01	0.05	0.05	3
FeI	4.27	0.00	0.00	0.00	0.00	0.00	0.14	0.14	149	5.18	-0.00	0.00	0.00	0.00	0.00	0.09	0.09	147
FeII	4.41	0.14	-0.03	0.02	0.01	0.01	0.08	0.09	15	5.33	0.15	-0.06	0.02	0.01	-0.01	0.07	0.10	15
CoI	2.03	0.27	0.01	0.00	0.00	-0.01	0.10	0.10	3	2.91	0.24	0.02	0.00	0.00	-0.02	0.20	0.20	3

Table 3 continued on next page

Table 3 (*continued*)

NiI	3.05	0.06	-0.01	0.00	0.00	0.01	0.12	0.12	10	3.82	-0.08	-0.01	0.00	0.00	0.01	0.12	0.12	15
ZnI	1.51	0.18	-0.02	0.01	0.00	0.01	0.22	0.22	2	2.43	0.19	-0.04	0.02	0.01	0.01	0.06	0.08	2
SrII	-0.41	-0.05	-0.01	0.01	-0.01	-0.08	0.10	0.13	2	0.69	0.14	-0.01	0.00	0.01	-0.01	0.10	0.10	2
YII	-1.44	-0.42	-0.02	0.01	0.00	-0.00	0.11	0.11	3	-0.31	-0.20	-0.03	0.03	0.01	0.01	0.18	0.19	4
ZrII	-0.39	0.26	-0.02	0.01	0.00	-0.00	0.14	0.14	2	0.50	0.24	-0.03	0.02	0.01	0.00	0.21	0.21	2
BaII	-1.88	-0.83	-0.01	0.01	0.00	-0.01	0.17	0.17	4	-0.27	-0.13	-0.02	0.01	0.01	-0.02	0.05	0.06	4
LaII	0	0
EuII	0	-1.36	0.44	-0.02	0.03	0.01	0.00	0.07	0.08	2

NOTE—The table of elemental abundances and abundance errors for all program stars is published in its entirety in the machine-readable format. Six example objects are shown here for guidance regarding the level of errors and the content of the table.

Since our program stars cover a rather wide range in the evolutionary status as well as metallicities, and include two sets of $\log g$ estimations, we consider the following cases when selecting example stars to present the typical abundance uncertainties for the whole sample: VMP/EMP stars, giant/turnoff stars which shall present different line numbers and strengths, parallax-derived $\log g$ and spectroscopic-corrected $\log g$. However, one should note that, as indicated in Figure 4, the spectroscopic-corrected $\log g$ case is in general only adopted on giants; therefore, six example targets have been selected to present the typical abundance uncertainties, as given in Table 3. It should be noted that, for species whose abundances have been derived from strong lines (e.g., resonance lines for Sr and Ba), the systematic error caused by uncertainties in microturbulent velocities is rather significant.

2.5. Giants and turnoff stars

To make sure that there is no significant offset between abundances derived for turn-off stars and giants due to technical problems in the abundance analysis, we here compare the elemental abundances of several key elements with relatively small internal scatters, including α -elements (Mg, Si, Ca, and Ti) and iron-group elements (Fe, Cr, Mn, Ni, Co, and Zn). For these elements, the surface abundances are expected to be unchanged through the evolution from turnoff stars to giants. The comparison of the derived abundances for giants (red circles) and turnoff stars (blue circles) are shown in Figure 9. In general, there is no systematic difference between the abundance distribution of giants and turnoff stars, while there are two exceptions, i.e., Mg and Cr, where offsets can be found in the abundance trends between giants and turnoff stars, and could mostly be explained by the NLTE effects. For Mg, the average $[\text{Mg}/\text{Fe}]$ for giants is about 0.1 dex higher than that of turnoff stars (see § 3.1.3). Such difference has also been discovered in the FS sample (as shown in Fig. 4 in Bonifacio et al. 2009), though they have found much larger discrepancies where EMP turnoff stars have 0.2 \sim 0.3 dex lower $[\text{Mg}/\text{Fe}]$ than EMP giants. The abundance difference observed in our sample is on average consistent with the NLTE correction difference between giants and turnoff stars at $[\text{Fe}/\text{H}] < -2.0$ (e.g., Osorio & Barklem 2016). According to Sobeck et al. (2007), a systematic difference between giants and turnoff stars for Cr is caused by metallicity dependence of Cr I lines probably due to the NLTE effect (see § 3.1.5). The dependence on effective temperatures is also reported and discussed in Suda et al. (2011). Note that for Si, Mn, and Zn, the number of turnoff stars at low metallicity is insufficient for this comparison.

2.6. Comparison with literature

For 22 stars in our sample, we have found high-resolution spectroscopic analyses compiled by the SAGA database (Suda et al. 2008, 2011; Yamada et al. 2013; Suda et al. 2017). Figures 10–12 present comparisons of stellar parameters and abundances for individual objects that are in common between the present study and literatures. The literatures considered here have measured abundances for multiple elements and have more than one common stars with our sample. Readers may refer to Table 1 for the methods adopted in the literature to derive stellar parameters.

There are generally good agreements in effective temperatures between our study and literatures that adopt photometric temperature (Cayrel et al. 2004; Honda et al. 2004a; Cohen et al. 2013; Lai et al. 2008). Poor agreements ($|\Delta T_{\text{eff}}| > 200$ K) are found for J2221+0228 (CS 29502–042) from Cayrel et al. (2004). We adopt $E(B - V) = 0.09$ for this object which is in the top 10 percentile from the largest among our sample. Because of this large extinction, the photometric temperature

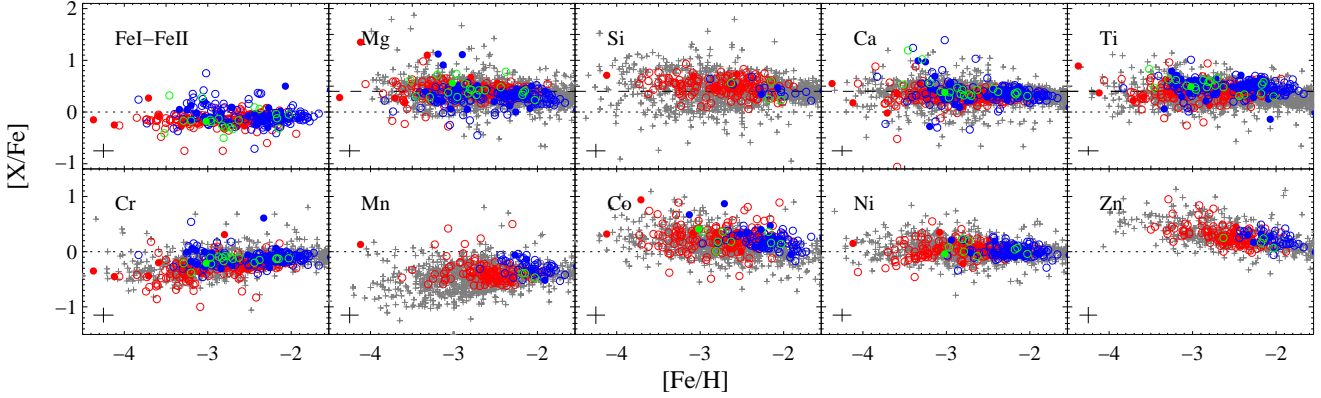


Figure 9. Distribution of α -element (Mg, Si, Ti, and Ca) and iron-group (Cr, Mn, Ni, Co, and Zn) abundances for the program stars (open and filled circles) along metallicities. Red, blue, and green symbols respectively refer to giants, turnoff, and horizontal-branch stars (defined as in Table 4), while CEMP and non-CEMP stars are shown with filled and open circles, respectively. Literature results obtained from the SAGA database are presented with pluses for comparison.

estimate could be more likely affected by the uncertainty in $E(B - V)$, the extinction law, and the choice of color from which temperatures are estimated. The corresponding $E(B - V)$ value in the literature is set to 0.00. The different $E(B - V)$ assumed is at least partially the reason for the discrepancy.

Literature that estimates effective temperatures from excitation balance of Fe I lines reports lower values than this study (Hollek et al. 2011). This systematic offset between spectroscopic and photometric temperatures has been known and is considered to be due to NLTE effects (e.g., Frebel et al. 2013; Amarsi et al. 2016). Sakari et al. (2018) adopts the same method but with line-by-line/mpstar $\langle 3D \rangle$ NLTE corrections by Amarsi et al. (2016), which, in fact, mitigates the offset. Li et al. (2015a) and Li et al. (2018a) also estimated temperature using Fe I lines, but their T_{eff} 's are in good agreement with the present study thanks to the correction by Frebel et al. (2013) that has been applied in these studies.

A good agreement is found in comparisons with the results of Matsuno et al. (2017b). They derived T_{eff} based on the high-resolution spectra making use of the profiles of the Balmer line wings that depend on T_{eff} and $\log g$ of the stars. Such T_{eff} scale is not dependent on Fe I lines.

Comparisons of surface gravity reveal a large scatter in $\Delta \log g$. Our $\log g$ values for these objects are determined using *Gaia* DR2 parallax, which could be more direct and reliable method than others (see § 2.2). Since the literature work is done before *Gaia* DR2, they had to rely on ionization balance of Fe or theoretical isochrones that provide a relation between T_{eff} and $\log g$. Since both methods introduce a strong correlation between the estimated T_{eff} and $\log g$, the large scatter reflects not only the difference in the method to determine $\log g$ but also the difference in adopted T_{eff} . In addition, ionization balance of Fe can be affected by the NLTE effect, which can introduce additional systematic errors.

Figures 10–12 shows that the offset in metallicity, especially $[\text{Fe}/\text{H}]$ from Fe I lines ($[\text{Fe I}/\text{H}]$), correlates with that in T_{eff} ; underestimated T_{eff} leads to underestimated $[\text{Fe}/\text{H}]$. An available number of Fe I lines in a spectrum is usually large enough that the choice of lines or the choice of oscillator strengths hardly affect the derived abundances. Instead, systematic uncertainties introduced by

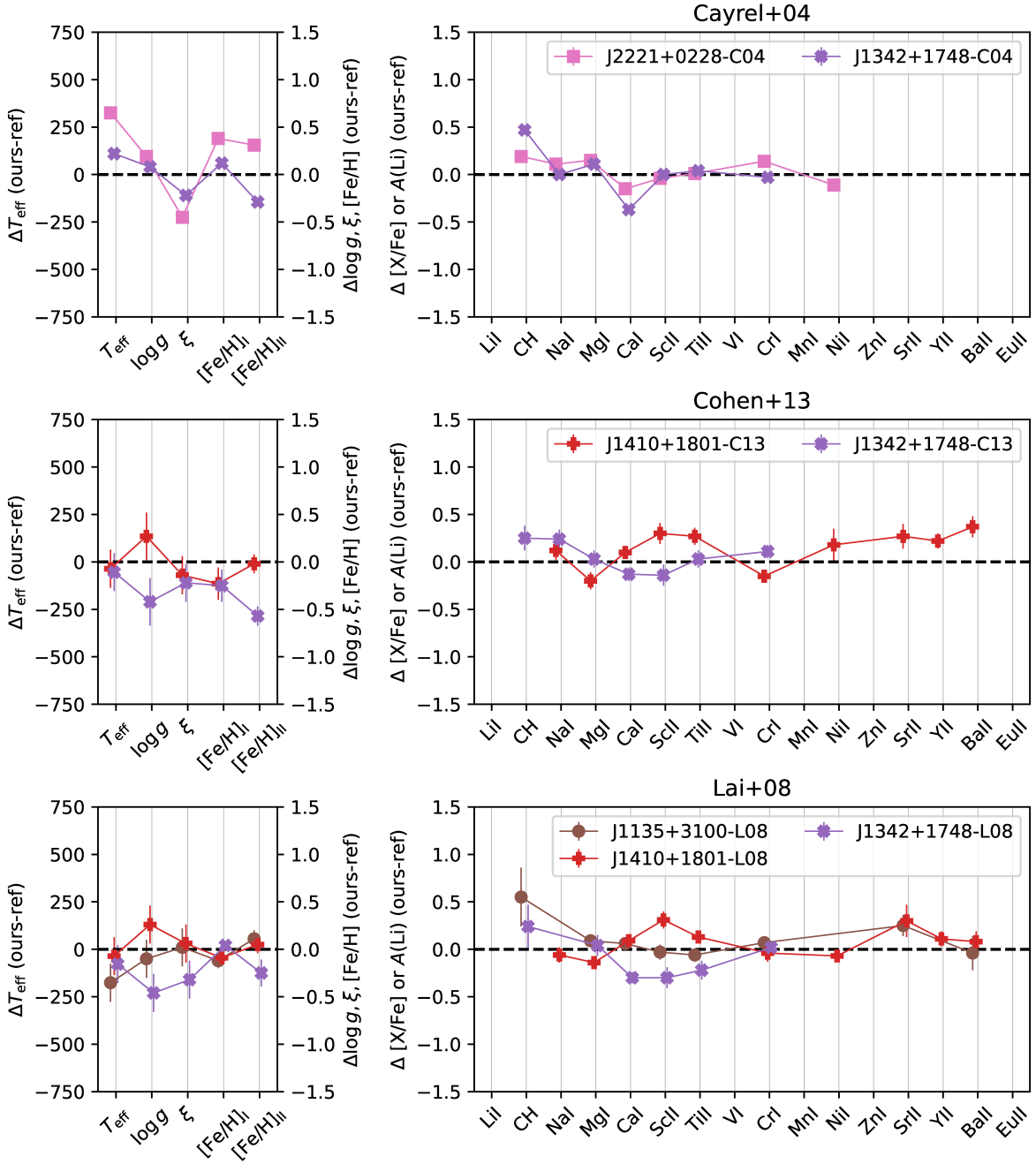


Figure 10. Stellar parameters and chemical abundance comparison with Cayrel et al. (2004), Cohen et al. (2013), and Lai et al. (2008). The same objects in different studies are shown with the same symbol in this figure. See Table 1 for the analysis methods adopted in the literature.

uncertain stellar parameters become the dominant source of uncertainties since the choice of stellar parameters affects the ionization and excitation states of Fe lines (see also Table 3).

The typical difference between the abundances from this work and those from literature ($|\Delta([X/\text{Fe}])|$) is < 0.13 and < 0.22 dex for 50% and 68%, respectively, of the sample presented in Figures 10–12. This level of difference is explained by the scatter seen in the comparisons of equivalent widths (Figures 2) and the possible offset of stellar parameters as discussed above. A

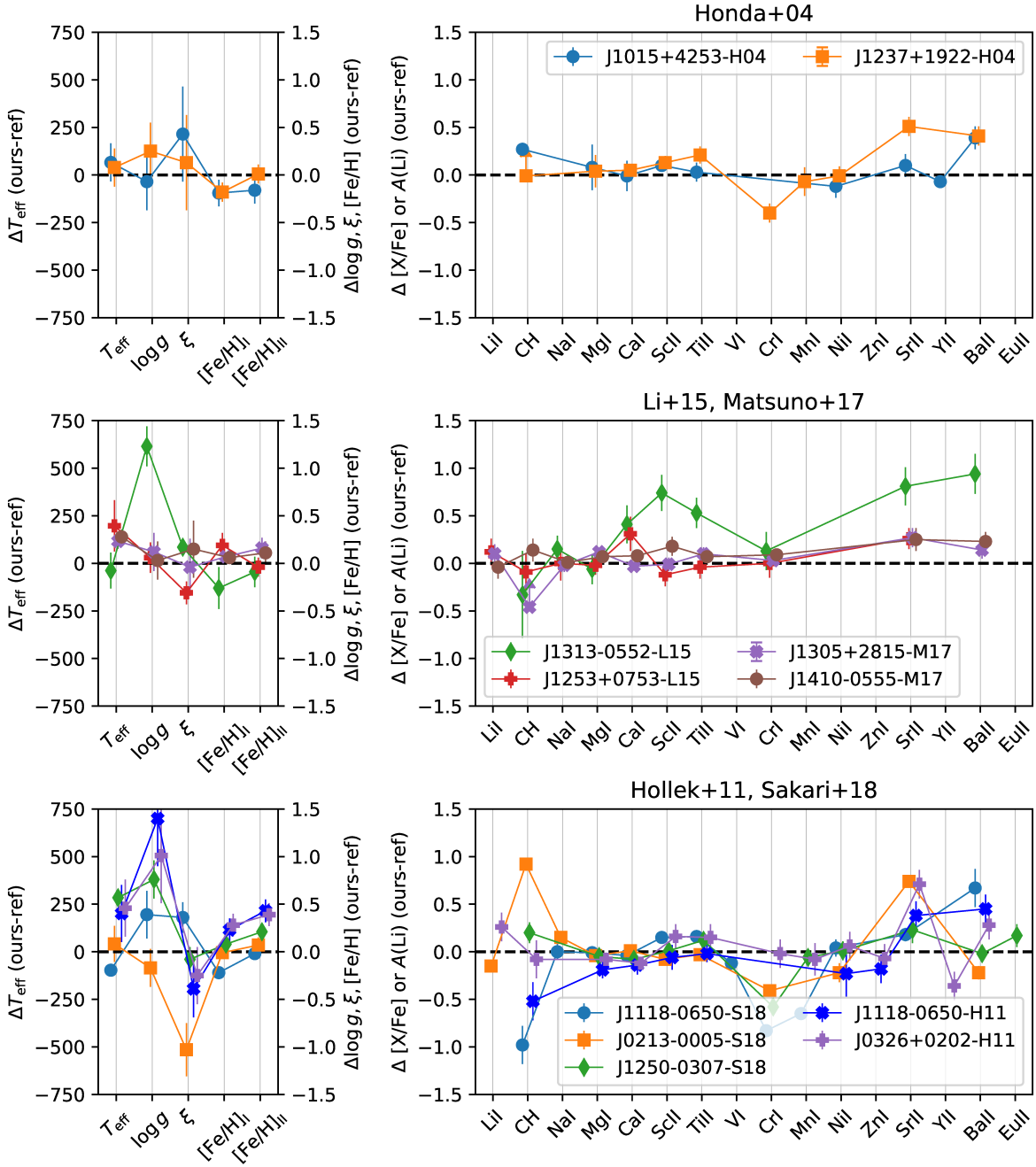


Figure 11. Same as Figure 10 but for comparisons with Honda et al. (2004a,b), Li et al. (2015a), Matsuno et al. (2017b), Hollek et al. (2011), and Sakari et al. (2018). Note that the same spectra from Li et al. (2015a) and Matsuno et al. (2017b) are used for the analysis in this paper. Unlike Figure 10, the same symbol does not correspond to the same object in this figure.

reason for large discrepancies found in some species is the difference of the spectral lines adopted for the analysis. For example, for the Li-rich VMP stars reported by Li et al. (2018a), quite different Na abundances have been derived for a few objects as shown in the bottom panel of Figure 12. This is because, for these objects, the subordinate Na lines at 5682 Å and 5688 Å are detectable and thus the resonance NaD lines are not included in abundance estimation, while, for the purpose of a uniform

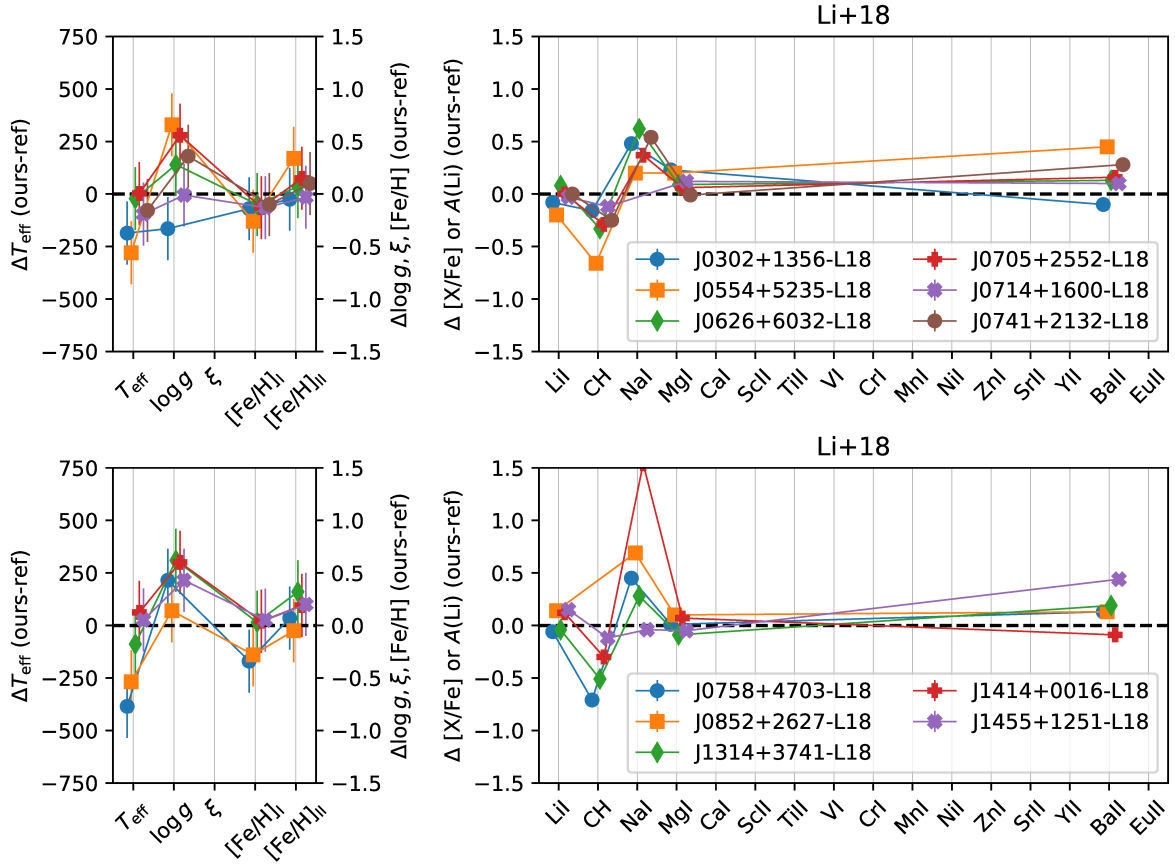


Figure 12. Same as Figure 10 but for comparisons with Li et al. (2018a). Note that the same spectra are used for the analysis in this paper and in Li et al. (2018a). Unlike Figure 10, the same symbol does not correspond to the same object in this figure.

analysis in this work, NaD lines have been used for all objects whenever they are measurable. The differences are mainly caused by the NLTE effect on the NaD lines. Indeed, the NLTE Na abundances derived from this work result in better agreement with those derived by Li et al. (2018a). We note that the relatively large differences are also seen in the abundance of Sr, which could be mainly due to its sensitivity to changes in microturbulent velocity (as discussed in § 2.4), and also affected by the choice of different atomic data.

3. INTERPRETATION OF THE RESULTS

3.1. Abundance trends of large sample of VMP stars

Elemental abundances of stars are characterized by the nucleosynthesis history before the formation of the stars and, hence, a large sample of Galactic VMP stars covering a wide metallicity range can provide important clues in understanding the synthesis of elements by early generations of stars and chemical evolution in stellar systems that have been formed in the Milky Way.

The observed abundance trends of $[X/Fe]$ along metallicities for individual species are presented in Figures 14, 15, 18, and 19 separately for Li and three groups of elements (light, iron-peak, and heavy). Figures 13 and 16 will be discussed in the subsections on Li and C abundances, respectively. Note that for the observed Li abundance trend (Figure 14), fittings are separately derived for the two metallicity ranges divided at $[Fe/H] = -2.5$, and objects that show enhancement in Li are excluded for deriving

Table 4. Definition of different classes of program stars

Class	Definition	Number	Symbol	Figure
Red Giant Branch (RGB)	$T_{\text{eff}} < 5500 \text{ K}$	194	red	Figure 9, 14, 15 through 23
Horizontal Branch (HB)	$T_{\text{eff}} \geq 5500 \text{ K} \ \& \ \log g < 3.0$	19	green	Figure 9, 14, 15 through 23
Turnoff (TO)	$T_{\text{eff}} \geq 5500 \text{ K} \ \& \ \log g \geq 3.0$	172	blue	Figure 9, 14, 15 through 23
C-Enhanced (CEMP)	Aoki et al. (2007) criteria	49	filled	Figure 9, 14, 15 through 23
non-CEMP ^a	not a confirmed CEMP	336	open	Figure 9, 14, 15 through 23

^aThis number does not exclude program stars whose C abundances have not been measured or with upper limits.

the trend. For abundance trends (slope, average, dispersion, etc.) presented in Figures 15, 18, and 19, only program stars with SNR higher than 50 which is about the average SNR of our program stars (open circle + crosses) are adopted for the fitting, while those with relatively low SNR are also shown (open circles) in the figures for completeness. During the following discussions, the sample has been divided into six categories, i.e., non-CEMP and CEMP giants, non-CEMP and CEMP horizontal branch stars, and non-CEMP and CEMP turnoff stars, as defined in Table 4. Compared to the “general trend” of elemental abundances of the so-called “normal population” among VMP and EMP stars, CEMP stars frequently present anomalous abundance patterns. Although the origins of carbon-excess would not be unique, the anomaly of the abundance patterns in CEMP stars would arise as the descendants of peculiar progenitors or as the contamination of their surface abundances with carbon. In this paper, the general abundance trend for each species is evaluated based on non-CEMP stars (whose spectral SNR is better than 50), while the CEMP objects are presented separately. Note that we here adopt the criterion of CEMP stars of Aoki et al. (2007) including the effect of the evolution on the red giant branch, represented by the luminosity: $[\text{C}/\text{Fe}] \geq +0.7$ for stars with $\log(L/L_{\odot}) \leq 2.3$; and $[\text{C}/\text{Fe}] \geq 3.0 - \log(L/L_{\odot})$ for more luminous objects.

3.1.1. Lithium

Among all the elements, lithium is of special importance as it is with primordial origin in metal-poor stars and is considered as a key diagnostic to constrain our understanding of the Big Bang nucleosynthesis, as well as low-mass star formation and evolution in the early Milky Way. It has long been a problem that the primordial lithium abundance predicted by the standard Big Bang nucleosynthesis (Cyburt et al. 2016; Fields et al. 2020) is nearly 0.5 dex higher than what has been observed in the oldest stars of the Galaxy as the Spite plateau (Spite & Spite 1982; Charbonnel & Primas 2005).

The trend of the Li abundances at lower metallicity is still unclear compared to the above metallicity range. It has been reported that significant fraction of stars show Li abundance below the Spite plateau value at $[\text{Fe}/\text{H}] < -2.5$ (e.g. Thorburn 1994; Norris et al. 1994; Ryan et al. 1999; Asplund et al. 2006; Aoki et al. 2009a), which is called meltdown of the Li Spite plateau for EMP stars (Sbordone et al. 2010). It is important to precisely understand how the Li abundance is distributed to understand astrophysical origin of this trend. The observational evidence is, however, sometimes confusing and contradicting each other. For example, while Meléndez et al. (2010) suggest that stars form another plateau at $[\text{Fe}/\text{H}] < -2.5$ with $A(\text{Li}) \sim 2.18$, which is lower than the Spite plateau value (~ 2.27 in their studies), Sbordone et al. (2010) detect a strong positive correlation between the lithium abundance and metallicity with a slope of 0.30 with $2 - 3\sigma$ of significance. Although Matsuno et al. (2017a) suggest that stars have almost constant Li abundance at $[\text{Fe}/\text{H}] < -3.5$ with

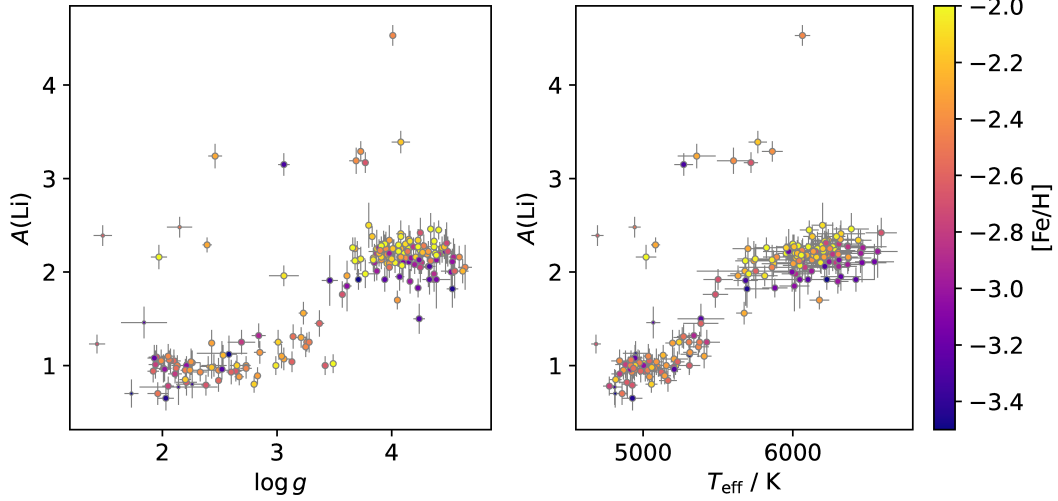


Figure 13. Li abundance of stars as a function of surface gravity and temperature. The color represent its iron abundance. Stars whose surface gravity relies on Fe I/Fe II ionization balance are shown with smaller symbols. Horizontal branch stars ($T_{\text{eff}} > 5500$ K and $\log g < 3.0$) do not appear in this figure because Li is not detected in these stars.

Table 5. The observed abundance trend of lithium

SNR > 50								
species	giant				turnoff			
	A	B	scatter	mean	A	B	scatter	mean
			dex	dex			dex	dex
A(Li)	1.11±0.79	0.05±0.30	0.26	1.03	2.56±0.08	0.17±0.03	0.08	2.18
[Fe/H] > -2.5	0.78±0.92	-0.09±0.39	0.07	1.02	2.12±0.16	-0.05±0.08	0.07	2.23
[Fe/H] < -2.5	1.01±0.64	0.02±0.23	0.18	1.03	2.61±0.58	0.20±0.20	0.08	2.04
SNR > 30								
species	giant				turnoff			
	A	B	scatter	mean	A	B	scatter	mean
			dex	dex			dex	dex
A(Li)	1.00±0.20	0.00±0.08	0.14	1.04	2.54±0.06	0.16±0.03	0.08	2.17
[Fe/H] > -2.5	1.00±0.45	0.00±0.19	0.10	1.03	2.29±0.13	0.04±0.06	0.07	2.22
[Fe/H] < -2.5	1.29±0.45	0.10±0.16	0.18	1.05	2.06±0.48	0.00±0.16	0.11	2.07

NOTE—The columns A and B correspond to the intercept and slope of the linear fitting of $A(\text{Li}) = A + B \times [\text{Fe}/\text{H}]$ as shown in Figure 14

$A(\text{Li}) \sim 1.9$, [Bonifacio et al. \(2018\)](#) and [Aguado et al. \(2019\)](#) reported higher Li abundance for stars with $[\text{Fe}/\text{H}] \sim -4.0$ and $[\text{Fe}/\text{H}] < -6.1$.

It is clearly seen in Figure 14 that the turnoff stars in our sample distribute around the plateau at $[\text{Fe}/\text{H}] \sim -2$. On the other hand, it shows a decreasing trend with decreasing metallicity from $A(\text{Li})=2.1$ dex at $[\text{Fe}/\text{H}] \sim -2.5$ to $A(\text{Li})=1.8$ dex at $[\text{Fe}/\text{H}] \sim -4.0$. These apparent features are consistent with previous findings, i.e., the Li meltdown at $[\text{Fe}/\text{H}] < -2.5$.

In the top panels of Figure 14 and Table 5, all non-CEMP (and not Li-enhanced) stars with spectral quality of $\text{SNR} > 50$ have been used to derive the abundance trend. For the turnoff stars,

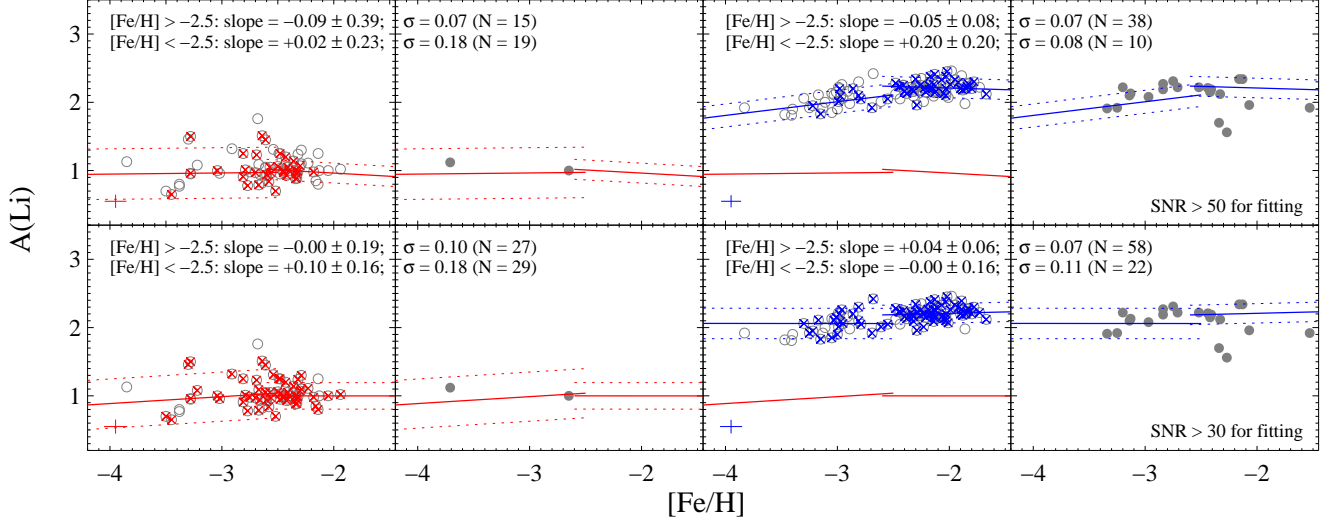


Figure 14. The abundance trend along metallicities is shown for lithium. The four columns, from the left to right, respectively refer to non-CEMP giants, CEMP giants, non-CEMP turnoff stars, and CEMP turnoff stars, as defined in Table 4. Open circles represent the non-CEMP objects, while filled circles for the CEMP stars. The typical error is shown in the lower left corner. Li-rich objects are not included in this plot or fitting. All non-CEMP objects which are not enhanced in lithium and have better spectral quality with $\text{SNR} > 50$ (top panels) and $\text{SNR} > 30$ (bottom panels) are marked with crosses and used to fit the abundance trend (red and blue solid lines), while the red and blue dotted lines show the 2σ scatter. In both cases, a segmented fitting has been derived respectively for the two metallicity regions divided at $[\text{Fe}/\text{H}] \sim -2.5$, which allows sufficient number of objects in both regions. The fitted trend for giants is also shown in panels of turnoff stars for comparison. There are no horizontal-branch stars in this plot, since Li is not detected for these objects. See the main text in 3.1.1 for more details.

the average of $A(\text{Li})$ is 2.23 for the plateau at $[\text{Fe}/\text{H}] > -2.5$, presenting no significant slope ($\Delta A(\text{Li})/\Delta[\text{Fe}/\text{H}] = -0.05$), which well agrees with the result from Meléndez et al. (2010). However, unlike their conclusion of almost no slope for both plateaus, a rather steep slope of 0.20 is found for our sample in the metallicity range between $[\text{Fe}/\text{H}] \sim -3.5$ and -2.5 , which agrees well with what has been found by Sbordone et al. (2010). It should be noted, however, that the significance of such a slope is around 1σ for our sample (Table 5). Moreover, if we loosen the requirement of spectral quality to $\text{SNR} > 30$ (bottom panels in Figure 14), the slope in $[\text{Fe}/\text{H}] < -2.5$ obtained by segmented fitting is unclear for the lower metallicity region in our study, presumably because most metal-poor stars are not well covered in our sample than previous studies that have focused on the measurements of Li abundances. There have been a number of other efforts on exploring the observed lithium plateau using extremely metal-poor stars (Matsuno et al. 2017a; Bonifacio et al. 2018; Aguado et al. 2019, e.g.); however, since their metallicity range ($[\text{Fe}/\text{H}] < -3.5$) is not sufficiently covered in our sample, comparisons with these studies are not discussed here.

It should be noticed that the derived lithium abundances are rather sensitive to the adopted stellar parameters, especially the effective temperature; therefore it is not surprising to find different slope or plateau among studies using different methods to derive stellar parameters, which makes a uniform sample with consistent data and methods very important when discussing the observed lithium trend. In summary, based on our sample, we confirm that there exists a flat Li plateau at $[\text{Fe}/\text{H}] > -2.5$,

and the average Li abundance is clearly lower when it comes to $[\text{Fe}/\text{H}] < -2.5$. However, the trend of $A(\text{Li})$ as a function of $[\text{Fe}/\text{H}]$ in the extremely low metallicity region is still unclear. Future follow-up studies with higher-quality spectra for EMP and UMP turnoff stars found by this study would be helpful to clarify the trend. Just to clarify, the following discussion is based on the trend derived from the case of $\text{SNR} > 50$.

The scatter of $A(\text{Li})$ around the slope in $[\text{Fe}/\text{H}] < -2.5$ is 0.08 dex, and that around the average value in $[\text{Fe}/\text{H}] > -2.5$ is 0.07 dex. These are similar to the level of scatter found by Meléndez et al. (2010) which derives 0.05 and 0.04 for the two metallicity ranges. Such small scatter around the plateau or slope provides a strong constraint on the scenarios to explain the discrepancy between predictions of the primordial Li abundance and the observed values, in particular scenarios that assume depletion of Li inside stars we are observing or during the star formation processes.

Several mechanisms have been proposed to explain the discrepancy between the Spite plateau and the expectation from the standard Big Bang nucleosynthesis by invoking atomic diffusion and turbulent mixing (Richard et al. 2005; Korn et al. 2006), Li-destruction during the pre-main-sequence phase (Fu et al. 2015), possible effect of chromospheric activity on the Li abundance measurement (Takeda 2019). There is also an observational indication that all the metal-poor stars observed in the current universe have experienced some Li depletion as their temperatures are not high enough (Gao et al. 2020). Although these studies have provided possible explanations for the discrepancy between the Spite plateau and the standard Big Bang nucleosynthesis, the breakdown of the Spite plateau at low metallicity needs further tuning of the models. For instance, although atomic diffusion is predicted to change the surface Li abundance differently for stars with different metallicity (Richard 2012), it is not yet clear how the metallicity plays a role when it is combined with turbulent mixing, which is considered to be needed to reproduce the constant Li abundance found for turnoff stars at $-2.5 < [\text{Fe}/\text{H}] < -1.6$.

The decreasing trend of $A(\text{Li})$ with decreasing metallicity in $[\text{Fe}/\text{H}] < -2.5$ is found for both non-CEMP and CEMP turnoff stars, suggesting that the depletion of lithium shall not be relevant to the origin of carbon enhancement, which is in agreement with what has been suggested by Matsuno et al. (2017b). We note that stars for which the Li resonance line is not detected are not plotted in the diagram. Most of them are CEMP-s stars that would be affected by mass accretion from the companion AGB stars (Masseron et al. 2012). Hence, the trend found for CEMP stars here is primarily based on CEMP-no stars.

Li abundance of giants also contains information about the Li-depletion during stellar evolution. Figure 13 shows $A(\text{Li})$ as a function of $\log g$ and T_{eff} . Here we adopt $\log g$ as the primary indicator of the evolutionary status from main-sequence to red giants, as the $\log g$ values are well determined for most objects thanks to the parallaxes provided by *Gaia*. As stars leave the main-sequence, their surface Li abundances decrease due to the dilution caused by the first dredge-up in the evolutionary stage of $3 \lesssim \log g \lesssim 4$. We note that the Li line is not detected in the horizontal branch stars with $\log g \sim 3$ and $T_{\text{eff}} > 5500$ K which would have already experienced Li-depletion in the red giant phase (see below). Comparing the Li abundance between the turnoff stars and giants observed in our sample, the degree of depletion can be as large as 1.0~1.2 dex, suggesting that the surface material is diluted by the first dredge-up by about 15 times. This is consistent with the theoretical models of low-mass stars that deplete surface lithium abundances by ~ 1.5 dex (Iben 1967). Li abundance of giants remains more or less constant after the first dredge-up up to the RGB bump (e.g., Lind et al.

2009), which is also seen in Figure 13. This indicates that Li is not further destroyed at this stage. Instead the Li abundance is mainly determined by the total Li content of the stellar surface and the maximum depth of the surface convective layer during the first dredge-up (e.g., Mucciarelli et al. 2012). It is also clear from Figures 14 and 13 that Li abundances do not show a distinctive trend in giants with metallicity down to $[\text{Fe}/\text{H}] \sim -3.5$: The average Li abundances in the two metallicity ranges of $[\text{Fe}/\text{H}] > -2.5$ and $[\text{Fe}/\text{H}] < -2.5$ are almost identical (1.02 and 1.04, respectively). This result is not inconsistent with the breakdown of the Spite plateau seen among turnoff stars if their surface lithium has been depleted by diffusion or gravitational settling (e.g., Richard et al. 2005). The Li abundance of these lower red giant branch stars are similar to the values seen in stars in globular clusters with similar evolutionary status (e.g., Lind et al. 2009; Mucciarelli et al. 2018).

Further decrease of Li is found in more evolved stars along the red giant branch above the RGB bump ($\log g \lesssim 2$), which suggests extra mixing. The Li line is not detected in most of these stars in our sample though the detection limit is lower in stars with low temperatures, indicating that their $A(\text{Li})$ is clearly lower than the values of red giants below the RGB bump.

As found in Figure 13, the Li abundances show a rapid drop at $\log g = 3.5 - 3.7$, and settle down to $A(\text{Li}) = 1.0 - 1.2$ at $\log g \approx 3.2$. This range is well covered by studies for globular cluster stars. The $\log g$ values corresponding to this transition well agrees with that found for the globular cluster NGC 6397 (Lind et al. 2009). There are three objects in the transition stage in our sample (J0006+0123, J0600+2301 and J0834+2307) that have T_{eff} of 5400 – 5650 K and $\log g = 3.2 - 3.4$.

Figures 13 contain stars with unusually high Li abundance. We have excluded these Li-rich objects in previous discussions on the plateaus and the general trend. These low-metallicity Li-rich stars are already reported in Li et al. (2018a). With updated $\log g$ estimates utilizing the *Gaia* DR2 parallax measurements, we confirm our previous findings that Li-rich stars are found at all evolutionary stage including a main-sequence turnoff star (Figure 13).

Recent studies of Li-enhanced stars in metal-rich evolved stars have reported that most Li-enhanced objects are found in clump stars rather than in red giant branch stars (e.g., Kumar et al. 2020; Yan et al. 2021). By contrast, at low metallicity, Li-rich objects distribute in a wide range of evolutionary status. Moreover, no Li-enhanced object is found in horizontal branch stars, which are metal-poor counterpart of clump stars, in our sample, although the sample size of such stars is still small (21 objects). This indicates that the mechanism of Li enhancement in very metal-poor stars could be different from that in Li-rich stars with high metallicity.

3.1.2. Carbon

Here we investigate stars excluding carbon-enhanced stars, which are discussed separately later in this section. As can be seen from top panels in Fig. 15, the distribution of the abundance ratios of $[\text{C}/\text{Fe}]$ exhibits two remarkable features: the average values for non-CEMP giants and turnoff stars are around the solar abundance, and the observed dispersion is larger than that of other light elements.

Decreases of carbon abundances in red giants have been reported for field and globular cluster stars, in particular objects above the red giant bump (e.g., Gratton et al. 2000; Shetrone et al. 2019). Hence, we need to discuss carbon abundances in red giants and main-sequence turn-off stars separately. Figure 15 shows the abundances for turnoff stars and giants in different panels. The carbon abundance ratios in turn-off stars would provide better constraint on chemical evolution models. However, the CH molecular bands are weak in general in turnoff stars and are only measurable in

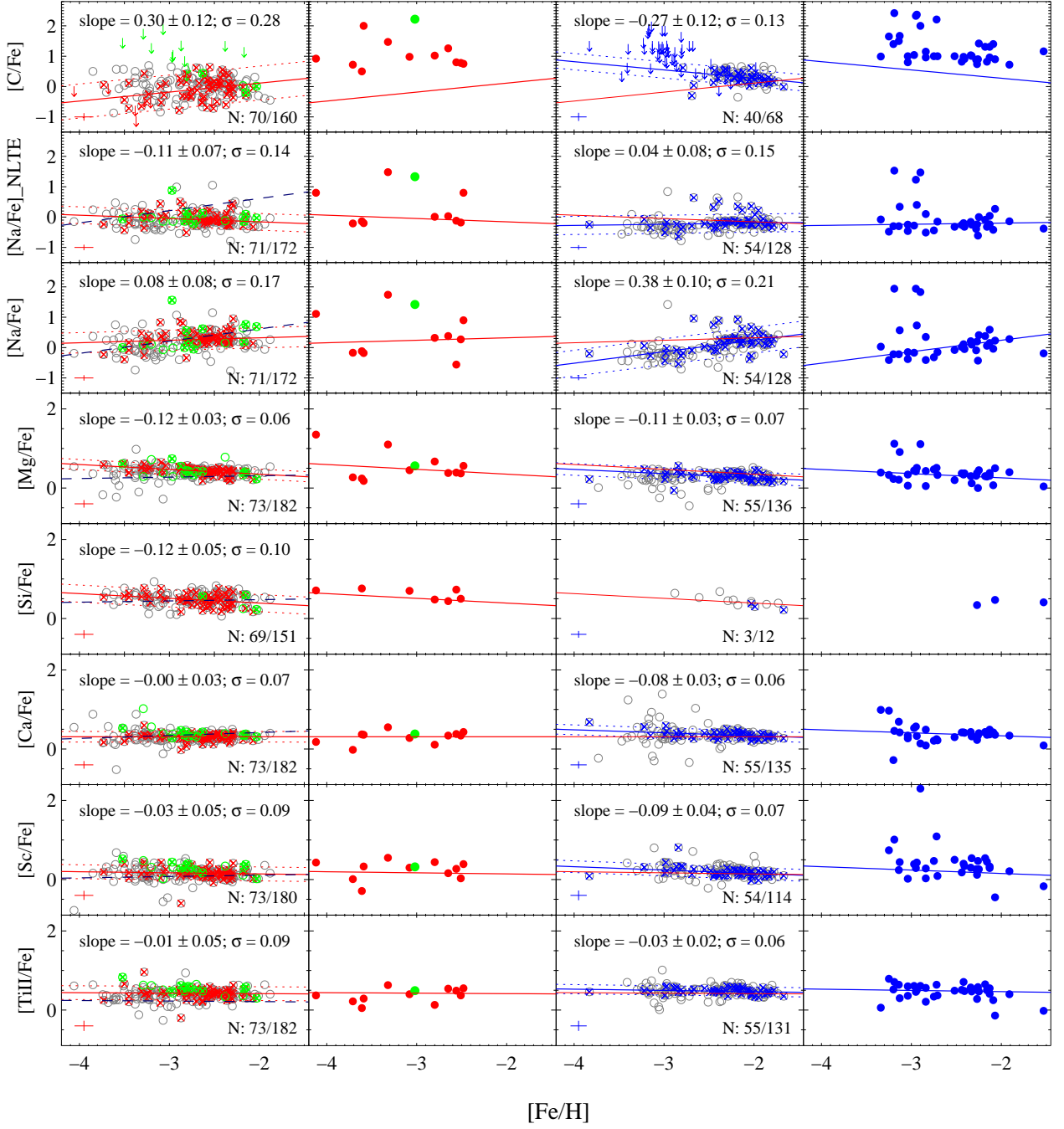


Figure 15. Abundance trend along metallicities for light elements. The four columns from the left to right respectively refer to non-CEMP giants (open circle), CEMP giants (red filled circle), non-CEMP turnoff stars (open circle), and CEMP turnoff stars (blue filled circle). Only program stars with $\text{SNR} > 50$ (open circle with cross) in the panels of non-CEMP giants and turnoff stars have been used to fit the trends (red and blue solid lines), while the red and blue dotted lines show the 2σ scatter. Horizontal-branch stars are also shown with green symbols in the panels of giants for reference. Slope of the fitting and the standard deviation (σ) around the fitting is shown in each panel. The two numbers in the lower right corner correspond to the number of objects with $\text{SNR} > 50$ (numerator) and all objects with measurement (denominator). The fitted trend for giants is also shown in panels of turnoff stars for comparison. Observational trends from the FS sample (dark blue dashed lines) are also presented for comparison. The steep slope found for $[\text{C}/\text{Fe}]$ of non-CEMP turnoff stars would be due to incompleteness of the sample (see text).

stars with relatively high C abundance. This limits the metallicity range for which the abundance trend is investigated, and also results in significant bias of the abundance trend because objects with higher $[C/Fe]$ are sampled at lower metallicity.

Figure 16 shows the $[C/H]$ values obtained for our sample as a function of T_{eff} . The line indicates the C abundances that produces CH molecular absorption with 3% depth in a high resolution spectra at the G-band estimated by the spectrum synthesis, which is the typical detection limit in our spectral data. If stars have $[C/Fe] \gtrsim 0$, their carbon abundance could be measured for giants ($T_{\text{eff}} < 5500$ K) with $[Fe/H] > -3.5$, whereas many warm stars could be missed, in particular for lower metallicity ($[Fe/H] < -3$).

Hence, although turnoff stars in our sample show decreasing trend in $[Fe/H]$ with increasing metallicity with a slope of -0.34 (Figure 15), this could be due to the incompleteness of the sampling of stars with lower metallicity. On the other hand, since the C abundances are measured in 95% of giant stars, the increasing trend of $[C/Fe]$ with increasing metallicity is not due to the temperature dependent detection limit of the CH band (see also §3.4).

The average carbon abundance for giants are about 0.4 dex lower than that for turnoff stars at a metallicity of $[Fe/H] \sim -2.5$. Such difference has also been noticed in the FS sample (Bonifacio et al. 2009). They suspect that it may be caused by the granulation (3D) effects. A quite thorough discussions on the 3D correction on C abundances in metal-poor stars have been presented by Norris & Yong (2019), which indicate that for VMP/EMP giants, the correction will slightly increase the C abundance (no more than 0.1 dex), while for turnoff and dwarf stars, it will decrease the abundance by 0.3-0.4 dex; therefore, adopting 3D correction could partially explain the observed discrepancy. This is, however, not sufficient for fully explaining the observed difference in our sample. The difference between giants and turnoff stars could be affected by the difference of the detection limit at least in our study, as inspected above. This indicates that there could be turnoff stars with lower $[C/Fe]$ than the current results. Another factor that affects the average $[C/Fe]$ values is the evolutionary effect in highly evolved red giants in which carbon could be significantly depleted by extra mixing (Spite et al. 2006; Aoki et al. 2007).

The giant stars in our sample present larger scatter (almost twice) in $[C/Fe]$ values than that of turnoff stars, as well as that in abundance ratios of other elements (e.g., Mg). This could partially be caused by the mixing during stellar evolution of low-mass stars along the giant branch, where carbon abundances could have been altered by the CNO cycle (i.e., C transformed into N). Indeed, C/H ratios are lower on average in cooler giants (Figure 16), in which larger effects of internal mixing are expected (e.g., Spite et al. 2005). We note that Placco et al. (2014b) apply corrections of carbon abundances taking into account the depletion due to CN processing on the upper red giant branch. We do not apply the corrections in this work, but include the effect in the criterion of CEMP stars.

3.1.3. α elements

All the four measured α elements Mg, Si, Ca, and Ti are enhanced relevant to Fe at similar level, where the averages of $[Mg/Fe]$, $[Si/Fe]$, $[Ca/Fe]$, and $[Ti/Fe]$ (for non-CEMP stars with spectral SNR > 50) are 0.42, 0.47, 0.30, and 0.40, respectively for giants, and 0.29, 0.30, 0.36, and 0.48 for turnoff stars. The ~ 0.1 dex offset of the $[Mg/Fe]$ between giants and turnoff stars has been discussed in § 2.5, and could be attributed to the different NLTE effect on Mg abundances between giants and turnoff stars. For $[Si/Fe]$, turnoff stars with measured Si abundances are very limited in number and only covers $[Fe/H] \sim -2.0$, which makes it impossible to compare with that for giants. We inspect

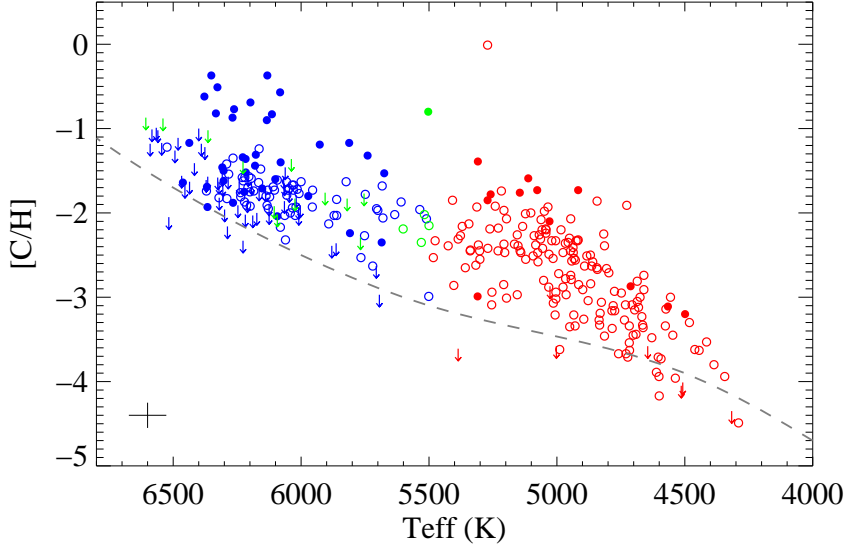


Figure 16. $[C/H]$ as a function of the effective temperature for the program stars. Red, blue, and green symbols refer to giant, turnoff, and horizontal-branch stars as defined in Table 4. The filled and open symbols respectively represent CEMP and non-CEMP stars, and the downward arrows refer to the upper limits. The dashed line indicates the value of $[C/H]$ for which the depth of the CH G-band reaches to about 3% below the local continuum, as a function of temperature, estimated from synthetic spectra.

stars having very high or low abundances of α elements separately in § 3.5. These α -peculiar objects are shown in Figure 15, but most of the α -deficient objects are excluded in the above statistics due to limited SNR of corresponding spectra, and while most α -enhanced objects are also C-enhanced and thus are neither included in the statistics.

Since there is only one line of Si around 4103 Å detectable in our spectra, which is blended with the wing of H δ for warmer stars, we could derive Si abundances mostly for giants, and only for 15 turnoff and four horizontal-branch stars. The standard deviation around the average abundance ratio is not larger than 0.1 dex for all the four species, which is as small as the measurement uncertainties. The abundance ratios for giants and turnoff stars are in good agreement with previous LTE measurements (e.g., FS sample, Y13 sample, Reggiani et al. 2017), though they are derived from different samples and analyses.

The observed abundance ratios of $[Ca/Fe]$ and $[Ti/Fe]$ in general agree well between giants and turnoff stars. Such agreement has been found for Ca in previous studies, e.g. FS sample (as shown with the purple line), Y13 sample, etc. On the other hand, Bonifacio et al. (2009) have found that the $[Ti/Fe]$ values in turnoff stars are 0.2 dex higher than those of EMP giants, which cannot be explained by uncertainties in atomic data or stellar parameters. The trends obtained by fitting to our sample support the direction of these differences, however, as shown in Tables 6 and 7, the observed discrepancies are negligible for our sample stars in the region of $[Fe/H] > -2.5$ and about 0.1 dex at $[Fe/H] \leq -2.5$. Both works have used Ti II and Fe I lines to derive the abundance ratio of $[Ti/Fe]$. A difference is that the $\log g$ has been determined based on parallaxes for our sample, while the FS sample is based on the ionization balance of Fe and Ti lines for the giant, and on the ionization balance of Fe for the turnoff/dwarf. This would lead to different Ti II and Fe I abundances, and thus

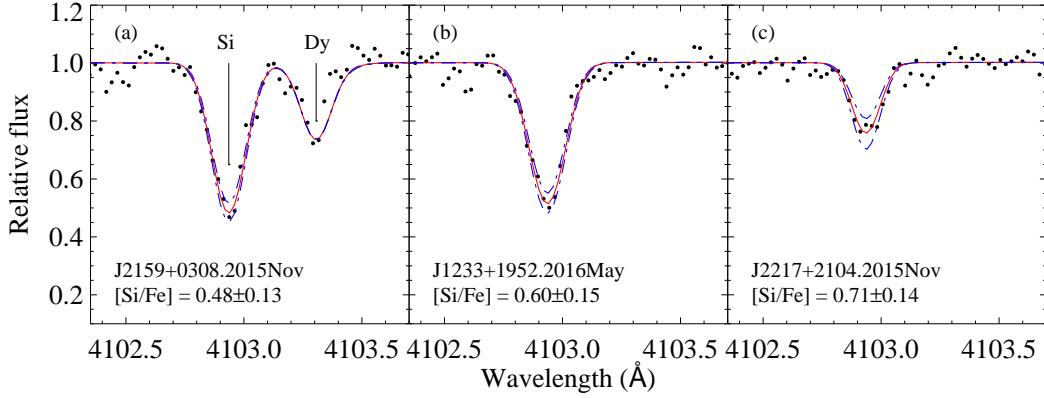


Figure 17. Samples of Subaru/HDS spectra near the 4103 Å Si line, respectively for a VMP (a), an EMP (b), and a UMP (c) program stars. Symbols are the same to that for Figure 7.

partly explain the discrepancy in the $[\text{Ti}/\text{Fe}]$ between the two works. Note that the NLTE correction is negligible for Ti II lines for metal-poor stars (e.g., [Sitnova et al. 2016](#)), while the level of NLTE correction for Fe I lines are comparable for giant and turnoff stars in our sample (e.g., [Lind et al. 2012](#)).

The over-abundances similarly found for the four α -elements suggest that the yields of Fe and these species hold similar ratios at low-metallicity environment, even though the detailed production site of these elements would be different (i.e., synthesis during stellar evolution, incomplete and complete burning during supernova explosions). Meanwhile, being a homogeneously observed and analyzed sample, the small dispersion of the observed abundance ratios of the α elements indicates that the stellar yields of their progenitor SN are rather homogeneous, and/or that the ejecta of the SN are sufficiently well-mixed with the surrounding ISM ([François et al. 2007](#)). Such small scatter could also be used to constrain the stellar mass range of their progenitors.

The slope of the trend along $[\text{Fe}/\text{H}]$ ($|\Delta[\text{X}/\text{Fe}]/\Delta[\text{Fe}/\text{H}]|$) is about 0.1 or shallower. It should be noted, however, that the slopes are negative in any cases. A more detailed inspection indicates that the slopes of $[\text{Mg}/\text{Fe}]$ both for turnoff stars and giants, which are relatively large among these three elements, are mostly caused by the decreases of the ratios at relatively high metallicity. Indeed, the average values of $[\text{Mg}/\text{Fe}]$ for giants and turnoff stars are 0.38 and 0.28 in $[\text{Fe}/\text{H}] > -2.5$, and 0.44 and 0.34 in the region of $[\text{Fe}/\text{H}] \leq -2.5$ (as seen in Table 6 and 7). Our sample extends to $[\text{Fe}/\text{H}] \sim -2.0$, which is not well covered by the FS sample. The difference of the metallicity coverage could be a reason for the difference of the average values and slopes between the FS sample and ours. Moreover, as pointed out by [Bonifacio et al. \(2009\)](#), the Mg abundance derived for the FS giants has been underestimated by about 0.15 dex since [Cayrel et al. \(2004\)](#) has neglected the wings of strong lines. It is also very likely that, at the metallicity region close to $[\text{Fe}/\text{H}] \sim -2.0$, some of the VMP stars are originated from progenitors that have experienced chemical evolution with a longer timescale, which results in low- α element abundances. This is, for example, seen among stars with large retrograde motion ([Matsuno et al. 2019](#)). [Reggiani et al. \(2017\)](#) made a similar discussion, when the traditional Galactic chemical evolution models usually only consider the evolution of in-situ halo but not including the accreted populations cannot fit the low- α population discovered by

Nissen & Schuster (2010). We inspect the stars with low- α element abundances in more details in § 3.5, and will discuss the connection with their kinematics in a forthcoming paper.

3.1.4. Light odd- Z elements

We have derived abundances for two light odd- Z elements, Na and Sc. The abundance ratios of [Na/Fe] exhibit a rather large scatter of about 0.2 dex for both giants and turnoff stars, which is very much consistent with what has been found in the FS sample. On the other hand, conformed to previous LTE abundance analysis, the [Na/Fe] ratio follows quite different trends between metal-poor giants and turnoff stars. It should be noticed, however, that, for VMP and EMP stars, the Na abundance is usually derived from the Na D resonance lines at 5890 Å and 5896 Å, and thus usually suffer rather strong NLTE effect. For example, the NLTE corrections for Na abundance estimated from the Na D lines can be as large as -0.5 dex for EMP stars (Lind et al. 2011). As NLTE effects are usually related to the metallicity, taking NLTE correction into consideration should then derive a different but more reliable abundance trend. Therefore, we have derived the NLTE Na abundances for all program stars whose Na lines are measurable, using the correction provided by Lind et al. (2011) through the INSPECT database³.

Depending on stellar parameters and spectral quality, the Sc abundances have been measured from 1 to 14 Sc II lines covered by our Subaru/HDS spectra. And the derived Sc abundance ratios of our sample are close to or only slightly overabundant compared to the solar value, and show rather small dispersion. Unlike what has been found in the FS sample, there is no clear discrepancy in Sc abundances between giants and turnoff stars in our sample, though the slope of the trend is slightly different.

3.1.5. Iron-peak elements

Iron-peak elements are synthesized in thermonuclear explosions of supernovae (Type Ia supernovae), as well as in incomplete or complete Si-burning during explosive burning of core-collapse supernovae (Woosley & Weaver 1995; Chieffi et al. 1998; Kobayashi et al. 2006) For our sample, abundances of six iron-group elements other than Fe have been measured, i.e., V, Cr, Mn, Co, Ni, and Zn. The V abundance has been derived from the V I 4379 Å line, and Zn has been determined from the two Zn I lines at 4722 and 4810 Å. There are quite a number of usable Cr I and Ni I lines in our spectra, ranging from one to dozens of, to determine the Cr and Ni abundances. One to three lines have been used to derive Mn (4055, 4783, and 4823 Å) and Co (4092, 4118, and 4121 Å).

As shown in Figure 18, for all these six elements, the dispersion of the abundance ratio is smaller than 0.10 dex. Such small dispersion can also be seen among CEMP stars. Abundance trends are more or less in agreement with the FS sample. Especially for the case of Cr, the observed trend agrees well with previous studies, and moreover, extremely small scatter over different metallicity regions can be found, which also supports previous observations (e.g., FS sample, Reggiani et al. 2017), demonstrating that the origin of Cr and Fe may be very closely linked. It should be noticed, however, that decreasing Cr abundance along decreasing metallicities found for giants could be due to the NLTE effect of the Cr I lines. For example, as Bergemann & Cescutti (2010) have pointed out, for metal-poor stars, the NLTE abundance corrections to Cr I lines can be as large as $+0.3 \sim +0.5$ dex, which becomes larger for lower $\log g$ and T_{eff} . Taking the NLTE correction into consideration, the abundance

³ <http://inspect-stars.com/>

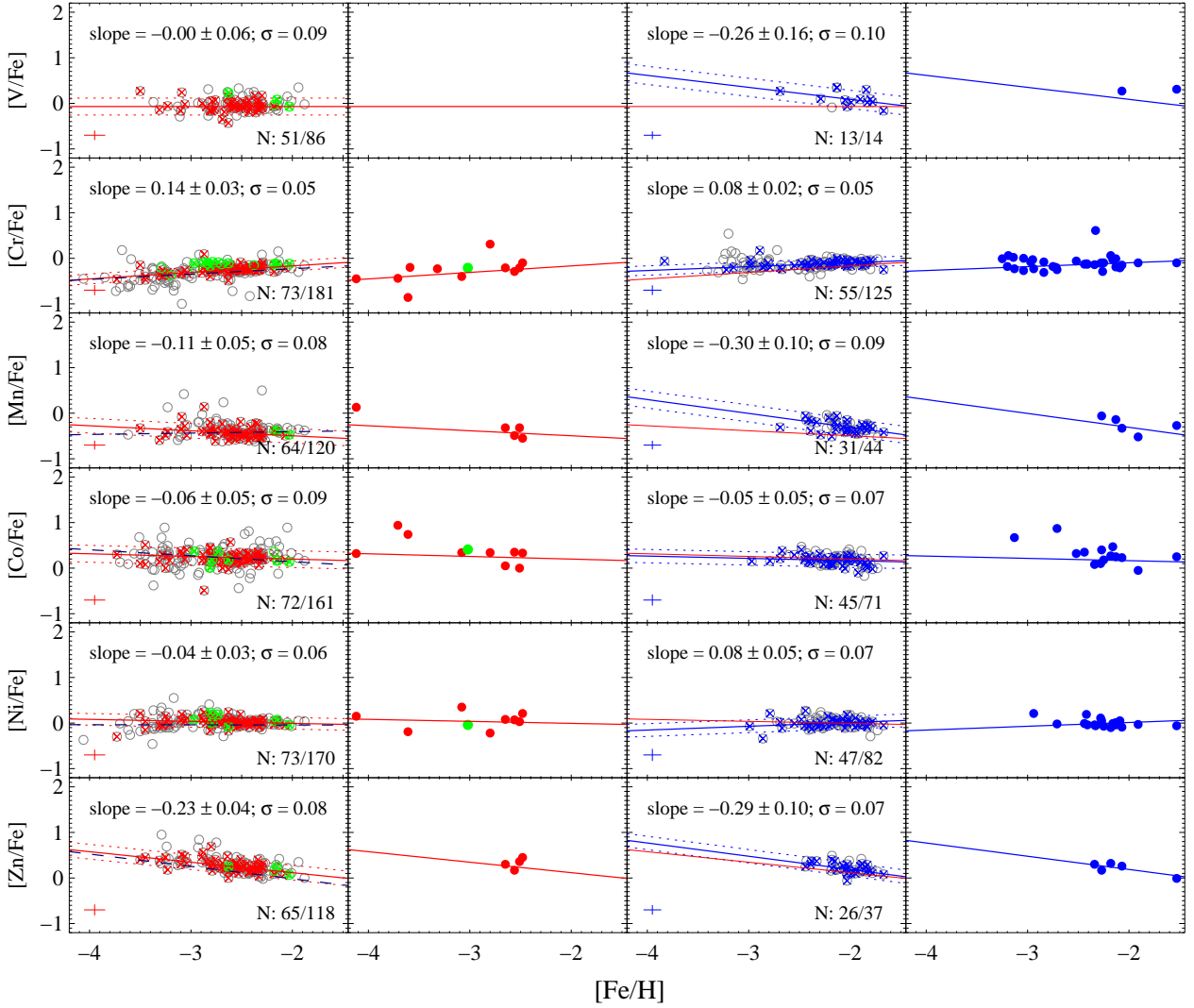


Figure 18. Abundance trend along metallicities for iron-group elements. The meaning of the lines and symbols are the same as in Figure 15.

ratio of $[\text{Cr}/\text{Fe}]$ derived from Cr I is approximately solar, and consistent with the measurement based on Cr II lines. This has also been verified by previous studies on Cr abundance for VMP stars (e.g., Lai et al. 2008, Reggiani et al. 2017).

Both giants and turnoff stars have similar abundance trends for the iron-group elements, except for the low Cr abundances in giants obtained by our LTE analysis as mentioned above. A very good agreement is found for Ni, which is consistent with both FS and Y13 sample. While both literature samples indicate that the abundances of Cr and Co in giants are 0.2 – 0.3 dex lower than those in turnoff stars. As observed in our sample, there is no clear discrepancy in the Co abundance, while for the case of Cr, the discrepancy can be as large as 0.2 dex at $[\text{Fe}/\text{H}] \sim -3.0$, which can be explained by NLTE effect as discussed above. For V, Mn, and Zn, due to the weakness of the absorption features, reliable abundances cannot be derived for EMP turnoff stars, which makes the slope of the

trend uncertain. If we limit the comparisons of the average abundances to the VMP region, giants and turnoff stars are consistent within the measurement uncertainties for V and Zn, while for Mn, a systematic abundance difference of about 0.2 dex is found. Such offset has been found in a number of previous studies (Lai et al. 2008; Bonifacio et al. 2009), and is not fully explained by current studies on NLTE effects.

Among all the measured iron-peak elements, Zn is of special importance to understand the physics of core-collapse supernovae as its main isotope is enhanced in the deepest region of HNe (Umeda & Nomoto 2002). Zn is believed to be mainly produced by complete Si burning at the low-metallicity region (Woosley & Weaver 1995; Kobayashi et al. 2006; Hirai et al. 2018), and the [Zn/Fe] ratio exhibits an increasing trend when the metallicity decreases. The average abundance ratios of [Zn/Fe] for our sample in $[\text{Fe}/\text{H}] > -2.5$ are 0.20 and 0.21 for giants and turnoff stars, respectively, in excellent agreement with the average value of 0.19 from Roederer & Barklem (2018) derived from UV Zn II lines that are less sensitive to NLTE effects to derive the Zn abundance. The observed slope of Zn is quite steep, with -0.23 for giants and -0.29 for turnoff stars, consistent with the measurement from Reggiani et al. (2017), with an average ratio of 0.29. A quite high Zn abundance ($[\text{Zn}/\text{Fe}] = 0.8$) is determined for the hyper metal-poor star HE 1327-2326 ($[\text{Fe}/\text{H}] = -5.2$ including NLTE correction) by the observation of the UV range (Ezzeddine et al. 2019). Interestingly, this data point is on the line of the increasing trend of [Zn/Fe] with decreasing [Fe/H] estimated from our sample (Figure 18).

3.1.6. Heavy elements

Elements heavier than iron-peak elements are mostly synthesized by neutron-capture processes. The s-process (main s-process) in AGB stars is a major contributor to the neutron-capture elements in solar-system material. However, the long timescale of the evolution of low- and intermediate-mass stars results in minor contributions of the main s-process to chemical evolution at very low metallicity (e.g., Kobayashi et al. 2011). It should be noted that some very metal-poor stars show large excess of s-process elements as well as carbon, which are recognized as a result of mass transfer from companion AGB stars that should have already evolved to white dwarfs (see § 3.4). The rapid neutron-capture process (r-process) produces heavy elements including actinides. A small fraction of very metal-poor stars shows a large excess of heavy elements with abundance pattern similar to that of the solar-system r-process component (Snedden et al. 2003), indicating the contribution of the r-process to the early chemical evolution. Mergers of binary neutron stars are considered as the major sites of the r-process, whereas other phenomena including magneto-rotational supernovae are also suggested (Cowan et al. 2021). To explain the light neutron-capture elements (e.g., Sr, Y, Zr) in very metal-poor stars, other processes have been proposed. They have been called LEPP (Travaglio et al. 2004) or weak r-process (Wanajo & Ishimaru 2006), but their mechanism and nucleosynthesis sites are not well determined. Mass loss from rotating massive stars, which could include light neutron-capture elements produced by the s-process during stellar evolution, is also proposed as a source at low metallicity (Choplin et al. 2018).

Among a large number of neutron-capture elements, only limited species can be detected in a sizable sub-sample of our program stars. Others are only found in a small number of stars in which neutron-capture elements are significantly enhanced. In this paper, we focus on six neutron-capture elements, Sr, Y, Zr, Ba, La, and Eu. Abundances for these elements have been derived from one to a few lines of Sr II (4077 and 4215 Å), Y II (4374, 4854, 4883, and 4900 Å), Zr II (4161 and 4209 Å),

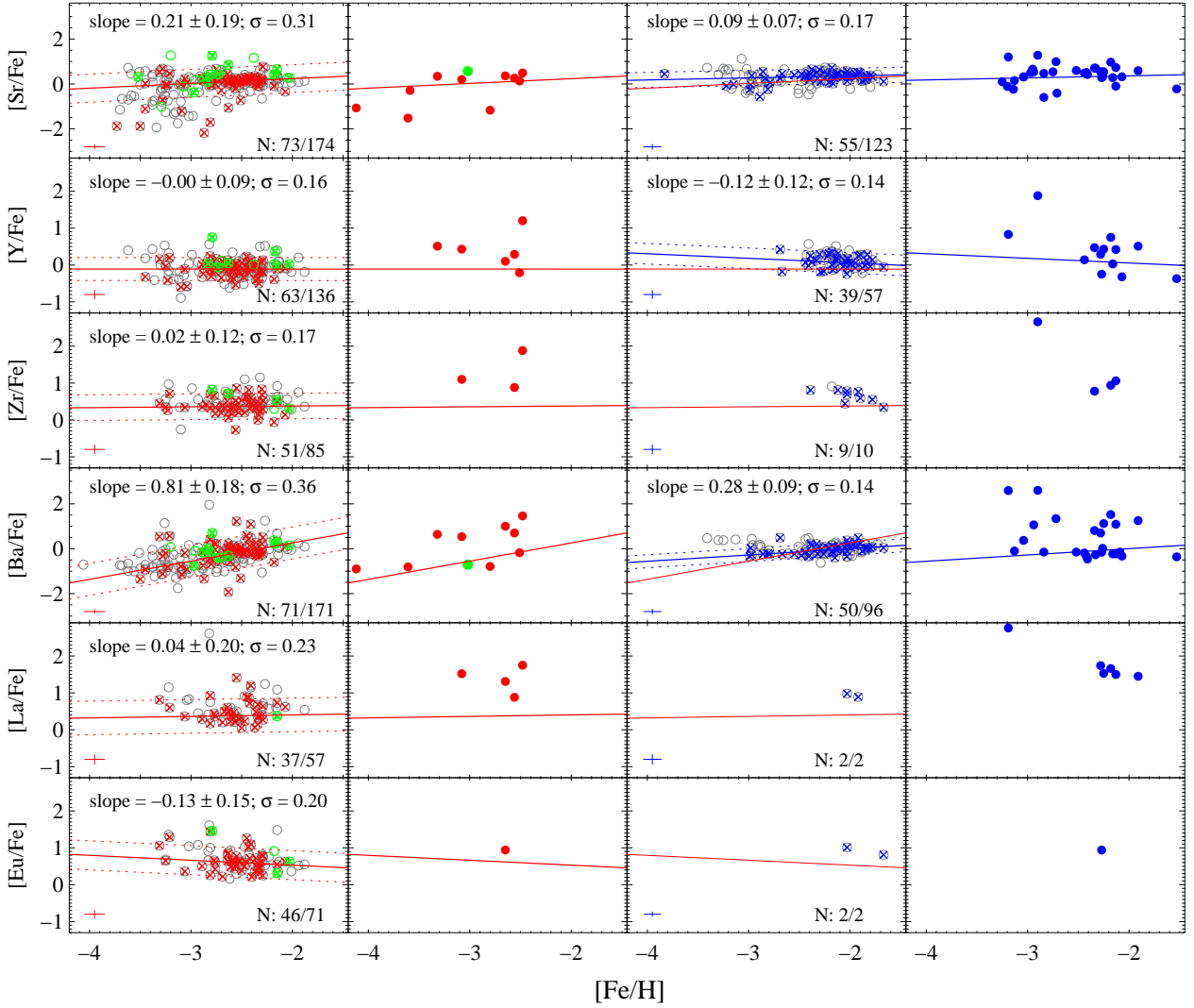


Figure 19. Abundance trend along metallicities for heavy elements. The meaning of the lines and symbols are the same as in Figure 15.

Ba II (4554, 4934, 6141, and 6497 Å), La II (4077, 4086, 4196, and 4921 Å), and Eu II (4129 and 4205 Å). There are about 50 objects for which abundances are derived for all the six elements, and the number becomes 80 if limited to detection of Sr, Ba, and Eu. The sample discussed here adds quite a number of EMP stars with measurement of these heavy elements, especially of Sr, Y, and Ba. Other neutron-capture elements that are measurable for a limited number of stars will be studied separately in future work.

Abundances of Sr, Ba and Eu are discussed in detail in § 3.6. We here provide a brief overview of the abundance trend of the six heavy elements. The objects for which Eu abundances are determined show abundance ratios of [Ba/Eu] similar to that of the r-process component in solar-system material (see § 3.6). We need to take account of the bias in the subsample that abundances of Eu, as well as Zr and La, are only measured in a very limited number of turnoff stars, because corresponding

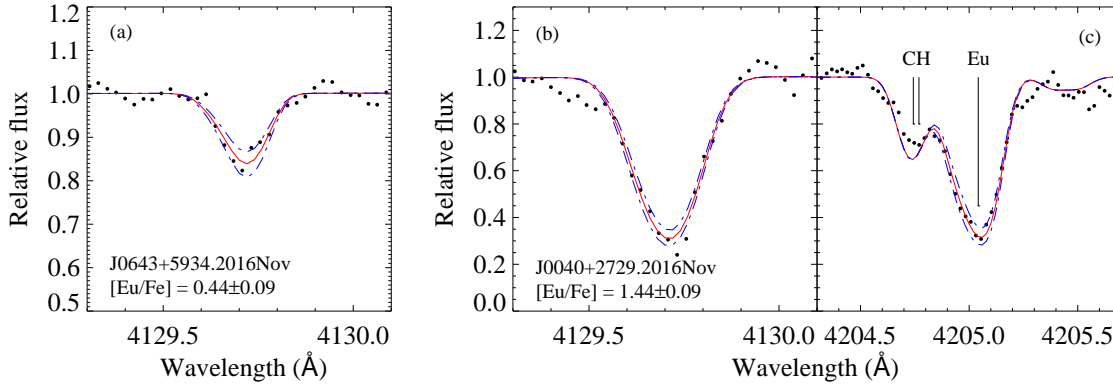


Figure 20. Examples of spectral fitting of the Eu 4129 Å line, for program stars with normal Eu abundance (a) and extreme enhancement (b). In a few case where the Eu 4205 Å line is measurable, Eu abundance has also been derived from fitting that line (c). Definition of symbols are the same as Figure 7.

absorption lines are generally too weak. No strong constraints on the origins of neutron-capture elements in stars with no detection of Eu have been obtained.

Sr is an important element for exploring the early enrichment of neutron-capture elements, since the two resonance lines are strong enough to be detected even in EMP/VMP stars. For our sample, we could derive the Sr abundances for about 96% program stars, including 185 giants, 157 turnoff stars, and 19 horizontal-branch stars. Exceptions are a dozen EMP turnoff stars with too weak lines and a few objects with blends of other species to the Sr lines.

The trend of Sr observed in our sample shown in Figure 19 is similar to those found by previous studies, e.g., a rather flat distribution around the solar values in $[\text{Fe}/\text{H}] \gtrsim -3.0$, and a drop in the abundance ratios below that metallicity range, indicating that the progressive enrichment of this element reaches the solar ratio when it comes to the metallicity of $-3.0 \sim -2.8$ on average. The other prominent feature of the Sr abundance is the large dispersion, especially in $[\text{Fe}/\text{H}] \lesssim -2.5$, which is clearly larger than the typical measurement uncertainties and the scatter found for α and iron-peak elements, indicating the existence of rare events that have provided the early universe with a significant amount of Sr.

The other two light neutron-capture elements Y and Zr show similar trend to Sr, in the sense of presenting a relatively constant distribution at $[\text{Fe}/\text{H}] > -3.0$, which is consistent with previous studies (e.g. Zhao & Magain 1991), but with a much larger sample. However, at lower metallicity region, these species neither exhibit such large dispersion as Sr nor drop in the abundance ratio as claimed by the FS sample. This would be basically due to the limited number of EMP stars (especially EMP turnoff stars) with Y and Zr measurements in our sample.

The three heavier elements Ba, La and Eu exist near the second abundance peak of neutron-capture elements ($Z \sim 52$ and $Z \sim 56$ for the r- and s-processes, respectively). We note that elements at the r-process peak, e.g., Te, have been little measured in stellar atmospheres (Roederer et al. 2012). Eu is a useful element with relatively high abundance that represent the contributions of the r-process. The Ba abundance has also been derived for the majority of our sample, including 181 giants, 122 turnoff stars, and 15 horizontal-branch stars. The dispersion of Ba abundances is as large as that of Sr. The objects with highest $[\text{Ba}/\text{Fe}]$ ratios are carbon-enhanced stars, which could be explained

Table 6. Observed abundance trends from C through Eu for giants

species	Regression line		All		[Fe/H] > -2.5		[Fe/H] ≤ -2.5		N ₁	N ₂
	A	B	mean	σ	mean ₁	σ ₁	mean ₂	σ ₂		
[C/Fe]	0.70±0.32	0.30±0.12	-0.05	0.28	0.01	0.23	-0.09	0.31	25	44
[Na/Fe] _{NLTE}	-0.38±0.19	-0.11±0.07	-0.05	0.14	-0.07	0.15	-0.04	0.13	24	46
[Na/Fe]	0.49±0.22	0.08±0.08	0.28	0.17	0.31	0.16	0.28	0.17	24	46
[Mg/Fe]	0.11±0.08	-0.12±0.03	0.42	0.06	0.38	0.08	0.44	0.06	25	47
[Si/Fe]	0.15±0.13	-0.12±0.05	0.47	0.11	0.46	0.15	0.48	0.09	24	44
[Ca/Fe]	0.31±0.08	0.00±0.03	0.30	0.07	0.31	0.06	0.29	0.07	25	47
[Sc/Fe]	0.09±0.13	-0.03±0.05	0.16	0.09	0.14	0.07	0.16	0.10	25	47
[Ti/Fe]	0.39±0.12	-0.01±0.05	0.40	0.09	0.40	0.06	0.41	0.10	25	47
[V/Fe]	-0.07±0.17	0.00±0.06	-0.06	0.09	-0.04	0.08	-0.07	0.10	21	30
[Cr/Fe]	0.12±0.07	0.14±0.03	-0.25	0.05	-0.21	0.04	-0.27	0.06	25	47
[Mn/Fe]	-0.71±0.14	-0.11±0.05	-0.42	0.08	-0.45	0.06	-0.40	0.09	25	39
[Co/Fe]	0.08±0.13	-0.06±0.05	0.22	0.09	0.24	0.06	0.21	0.11	25	46
[Ni/Fe]	-0.09±0.08	-0.04±0.03	0.02	0.06	-0.00	0.03	0.04	0.07	25	47
[Zn/Fe]	-0.34±0.12	-0.23±0.04	0.27	0.08	0.20	0.06	0.31	0.09	25	40
[Sr/Fe]	0.66±0.51	0.21±0.19	-0.03	0.31	0.16	0.15	-0.09	0.37	25	47
[Y/Fe]	-0.11±0.23	0.00±0.09	-0.12	0.16	-0.12	0.14	-0.13	0.16	25	38
[Zr/Fe]	0.42±0.30	0.02±0.12	0.39	0.17	0.40	0.19	0.38	0.16	23	28
[Ba/Fe]	1.88±0.49	0.81±0.18	-0.22	0.36	0.02	0.27	-0.35	0.40	25	46
[La/Fe]	0.48±0.53	0.04±0.20	0.49	0.23	0.54	0.26	0.45	0.20	16	21
[Eu/Fe]	0.26±0.39	-0.13±0.15	0.63	0.20	0.61	0.20	0.65	0.19	21	25

NOTE—The columns A and B correspond to the intercept and slope of the linear fitting of $[X/Fe] = A + B \times [Fe/H]$ as shown in the first column of Figure 15, 18, and 19.

by mass transfer from companion AGB stars (§ 3.4). Some Ba-enhanced stars are explained as the large contribution of the r-process, taking account of their [Ba/Eu] ratios (~ -0.7 , as presented in § 3.6). The large excess of r-process elements in small fraction of extremely metal-poor stars has been interpreted as a result of insufficient mixing in interstellar matter polluted by r-process events from which low-mass metal-poor stars were formed. Recent discoveries of ultra-faint dwarf galaxies with large excess of r-process elements (e.g., Roederer et al. 2016; Ji et al. 2016), however, suggest that the dispersion could be attributed to the difference of the r-process abundances between small stellar systems in which metal-poor stars were formed and later accreted to the Milky Way (e.g., Hirai et al. 2015).

It should be noted that there are several CEMP stars exhibiting significant enhancement in heavy elements, in particular Ba (Figure 19), which are usually explained by mass-transfer from its companion AGB star in a binary system. The excess of heavy elements in these stars is attributed to the s-process in AGB stars rather than the r-process (§ 3.4).

3.2. Comparison with chemical evolution models

A large sample of VMP stars is very useful to examine and constrain the Galactic chemical evolution models. While previous studies are usually based on comparisons with results from different sets of observational data, which could inevitably involve offset between different data sets and analysis methods. Our sample is thus especially valuable in the sense that it is uniform and the observed

Table 7. Observed abundance trends from C through Eu for turnoff stars

species	Regression line		All		[Fe/H] > -2.5		[Fe/H] ≤ -2.5		N ₁	N ₂
	A	B	mean	σ	mean ₁	σ ₁	mean ₂	σ ₂		
[C/Fe]	-0.27± 0.26	-0.27± 0.12	0.28	0.13	0.29	0.11	0.12	0.44	37	3
[Na/Fe] _{NLTE}	-0.12± 0.18	0.04± 0.08	-0.15	0.15	-0.13	0.14	-0.24	0.19	41	12
[Na/Fe]	1.00± 0.23	0.38± 0.10	0.16	0.21	0.24	0.21	-0.09	0.22	41	12
[Mg/Fe]	0.05± 0.08	-0.11± 0.03	0.29	0.07	0.28	0.06	0.34	0.09	41	13
[Si/Fe] ^a	0.30	0.08	0.30	0.08	3	0
[Ca/Fe]	0.18± 0.06	-0.08± 0.03	0.36	0.06	0.34	0.05	0.39	0.08	41	13
[Sc/Fe]	-0.02± 0.09	-0.09± 0.04	0.19	0.07	0.15	0.06	0.32	0.12	41	12
[Ti/Fe]	0.40± 0.05	-0.03± 0.02	0.48	0.06	0.47	0.06	0.51	0.06	41	13
[V/Fe]	-0.44± 0.32	-0.26± 0.16	0.11	0.10	0.10	0.11	0.27	0.00	12	1
[Cr/Fe]	0.07± 0.06	0.08± 0.02	-0.12	0.05	-0.11	0.04	-0.14	0.07	41	13
[Mn/Fe]	-0.92± 0.20	-0.30± 0.10	-0.30	0.09	-0.30	0.09	-0.31	0.21	30	1
[Co/Fe]	0.06± 0.11	-0.05± 0.05	0.17	0.07	0.16	0.07	0.24	0.08	40	5
[Ni/Fe]	0.18± 0.11	0.08± 0.05	0.00	0.07	0.01	0.06	-0.05	0.12	41	6
[Zn/Fe]	-0.39± 0.20	-0.29± 0.10	0.21	0.07	0.21	0.07	26	0
[Sr/Fe]	0.55± 0.17	0.09± 0.07	0.30	0.17	0.36	0.13	0.09	0.29	41	13
[Y/Fe]	-0.19± 0.26	-0.12± 0.12	0.08	0.14	0.08	0.13	0.12	0.30	37	2
[Zr/Fe] ^a	0.64	0.17	0.64	0.17	9	0
[Ba/Fe]	0.56± 0.20	0.28± 0.09	-0.03	0.14	-0.00	0.15	-0.14	0.14	41	9
[La/Fe] ^a	0.94	0.06	0.94	0.06	2	0
[Eu/Fe] ^a	0.91	0.14	0.91	0.14	2	0

^aFor species with too limited number of objects to derive the fitting trend, the σ refers to the standard deviation of all measurements.

NOTE—The columns A and B correspond to the intercept and slope of the linear fitting of $[X/Fe] = A + B \times [Fe/H]$ as shown in the third column of Figure 15, 18, and 19.

abundance dispersion is able to better reflect chemical inhomogeneity in the interstellar medium at very early epochs of the Galactic evolution.

Model predictions for chemical enrichment in the Galaxy are compared with our observational trends in Figure 21. The selected models shown are R10 (Romano et al. 2010), P18 (Prantzos et al. 2018), and K20 (Kobayashi et al. 2020). R10 has computed 15 models with different sets of nucleosynthesis prescriptions, and the best yield choice Model 15 has been selected for our comparison, which uses the yields by Karakas (2010) for low-to-intermediate mass (LIM) stars, the yields for massive stars limited to the pre-supernova stage, but computed with both mass loss and rotation (Hirschi 2007; Ekström et al. 2008), and the results of explosive nucleosynthesis of Kobayashi et al. (2006) for SN II below $20 M_{\odot}$ and hypernovae above that limit. P18 is based on Goswami & Prantzos (2000), and update by Kubryk et al. (2015), which adopts the stellar IMF of Kroupa (2002) in the mass range $0.1 - 120 M_{\odot}$, the metallicity-dependent yields of Cristallo et al. (2015) for LIM stars and of Limongi & Chieffi (2018) for massive stars, and Iwamoto et al. (1999) for SNIa by interpolating models for $Z = 0$ and Z_{\odot} . Their baseline model with rotating massive star yields has been selected for our comparison. K20 adopts the Kroupa (2008) initial mass function at $0.01 - 50 M_{\odot}$, and the SN Ia model based on the single-degenerate scenario (Kobayashi & Nomoto 2009) with the metallicity effect (Kobayashi et al. 1998). The nucleosynthesis yields from 1D models are taken from Kobayashi et al. (2006) and Kobayashi et al. (2011) for SN and hypernovae (with the metallicity-dependent fraction of

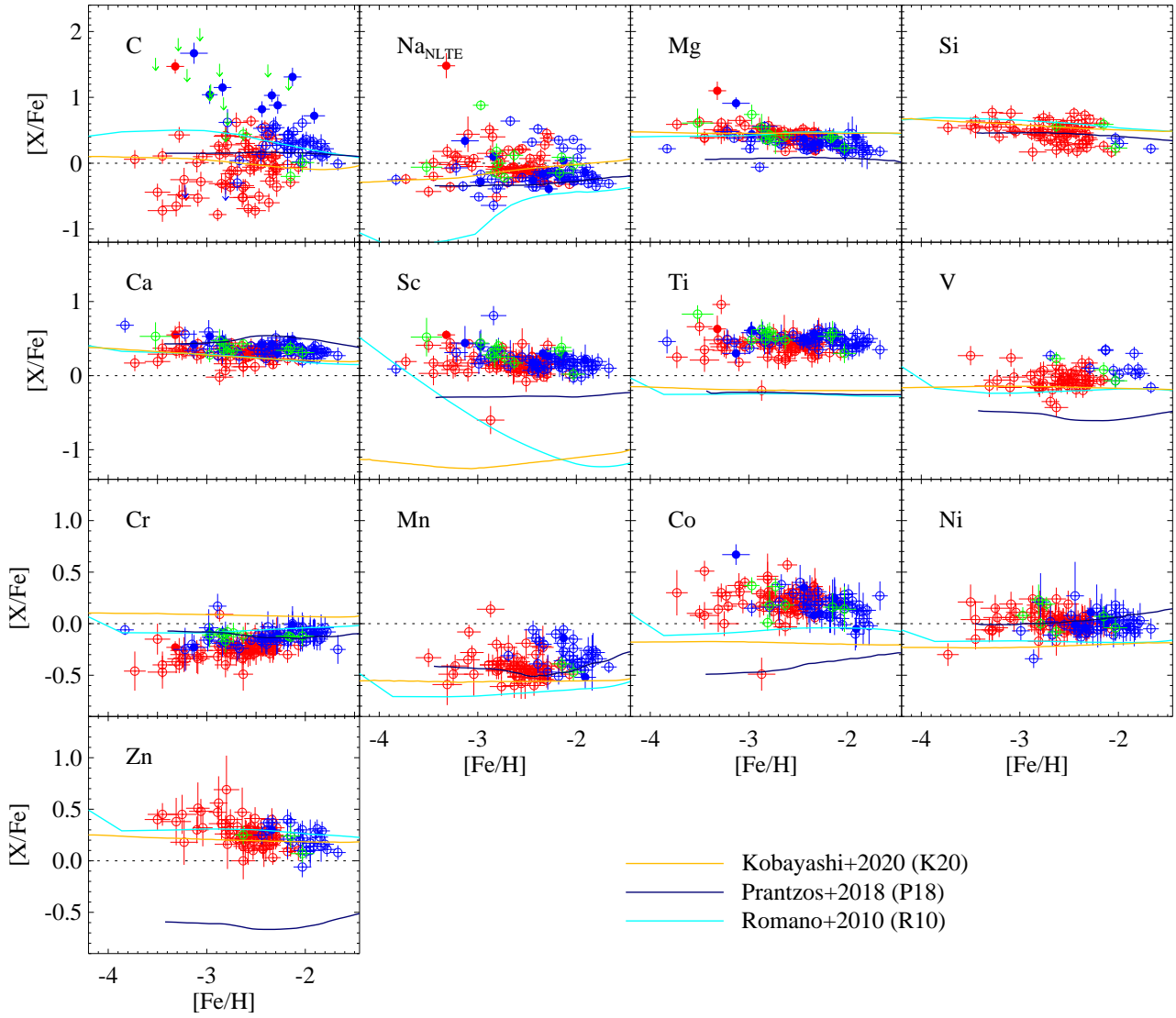


Figure 21. Abundance trend along metallicities for light and iron-peak elements. The meaning of symbols are the same as in Figure 15, and note that only objects with $\text{SNR} > 50$ are included for comparisons with theoretical models. Theoretical predictions from P18, K20, and R10 are shown in solid lines with navy, gold, and cyan, respectively. See the main text in 3.2 for more details.

hypernovae tested), and from Lugaro et al. (2012), Fishlock et al. (2014), and Karakas et al. (2018) for low-metallicity AGB stars. Readers may refer to their papers for more details about the above models.

The three models predict solar abundance ratio or over-abundance of carbon, i.e., $[\text{C}/\text{Fe}] \gtrsim 0$. R10 best fits the observed trend for TO stars, while the other two models predict relatively flatter trend. Here we primarily focus on comparison with turnoff stars, since carbon abundances in giants shall partly reflect results of internal mixing (§3.1.2). R10 exhibit the best agreement with the decreasing

trend of $[\text{C}/\text{Fe}]$ ratios found for turnoff stars (Figure 15), although our sample is not sufficient to constrain the behavior of carbon at the EMP region.

The odd-Z element, Na is synthesized mostly during hydrostatic carbon burning, partly during hydrogen burning through the NeNa cycle, as well as the s -process. As discussed in § 3.1, the LTE approximation can lead to substantial overestimation of Na abundances, and thus the NLTE corrected Na abundances are used for comparison with model predictions. K20 can fit the observed abundance trend in general. P18 also reproduce the trend, although the $[\text{C}/\text{Fe}]$ values predicted are slightly lower than the observational trend. while the sharp decline of Na abundances with decreasing metallicity predicted by R10 is not supported by the result of this work. As discussed in R10, only a set of model without HNe predicts a $[\text{Na}/\text{Fe}]$ ratio in agreement with the halo data, while models (including Model 15 that is adopted here for comparison) including nucleosynthesis from HNe tend to underestimate the $[\text{Na}/\text{Fe}]$ in the low-metallicity region. The discrepancy between R10 and the observation could be as large as 1.4 dex at the extremely low metallicity region, which are mainly driven by the adopted mass cut and energy of the explosion in models of massive stars, and shall reduce to ~ 0.2 dex when it goes up to $[\text{Fe}/\text{H}] \sim -2.0$.

Among the α -elements, R10 and K20 predicted rather similar abundance trend, as they have adopted the similar sets of yields of massive stars and LIM stars. Both models reproduce the observational results well for Ca, and marginally for Mg and Si. P18 fits the trend best for $[\text{Si}/\text{Fe}]$ and partially for Ca, while tends to underestimate the Mg abundance in general. This would be due to the yields adopted by P18, which also underproduce the Mg abundances obtained from Mg isotopes in solar-system material. However, the situation for Ti is very different. We discuss this problem below. All the three models predict a plateau behavior of Ti as generally found for α -elements, but the predicted values are much lower than observations, even though efforts have been made to account for higher Ti abundances, e.g., inclusion of hypernova jets by (Kobayashi et al. 2015). In particular, the very similar level of deficiency resulted from various sets of yields is quite intriguing. The deficiency is unable to be explained by uncertainties of the measurements, including the choice of the species (i.e., Ti I or Ti II) to determine Ti abundance. Although the abundances derived from Ti II lines are in general higher than those from Ti I in the present work, the difference is at most 0.1 – 0.2 dex. Moreover, as discussed in § 3.1.3, the NLTE effect on abundances derived from Ti II lines is negligible, while the NLTE effect of Fe I which would also affect the adopted $[\text{Ti}/\text{Fe}]$ is also about 0.1 – 0.2 dex. Hence, the overabundance of Ti derived by the present work is robust. Previous studies including FS and Y13 also indicate similar discrepancy between observations and models. P18 suggest the importance of further investigation of physical condition where the major Ti isotope ^{48}Ti is produced though ^{48}Cr , in particular the net production out of the equilibrium (some kind of α -rich freeze out). Such condition could be realized by multi-dimensional models of supernovae, including jet-induced explosions (Tominaga 2009).

Meanwhile, the slope found for $[\alpha/\text{Fe}]$, reported in § 3.1, is not well reproduced by chemical evolution models. The discrepancy is distinct in $[\text{Mg}/\text{Fe}]$ (also seen in $[\text{Si}/\text{Fe}]$) at $[\text{Fe}/\text{H}] > -2.5$, where the abundance ratios could be affected by contributions of small stellar systems like dwarf galaxies that usually contain stars with lower $[\alpha/\text{Fe}]$ formed with longer time-scale.

The predicted abundance trends of Sc and V are in overall underabundant for all three selected models. Especially pointed out by R10, the predicted $[\text{Sc}/\text{Fe}]$ ratios severely disagree with observations if the Kobayashi et al. (2006) yields for massive stars are used, independently of the assumed

hypernova (HN) fraction. Tests carried out by P18, which include the contribution of rotating massive stars, show that consideration of this effect could reduce the observation-model discrepancy to a certain degree, but cannot fully solve the overall underproduction. Both R10 and K20 have mentioned that the ν -process can increase the production of these elements. Besides, it is suggested that nucleosynthesis calculations with 2D supernova explosion models are able to solve the problem (Maeda & Nomoto 2003), which might also solve the underproduction problem for Ti.

For iron-peak elements, model prediction can more or less reproduce the observed trends for the cases of Cr, Mn, and Ni, while shows larger discrepancies for Co and Zn. All three models predict an almost constant [Cr/Fe] distribution, which agrees well with the turnoff sample. As discussed in § 3.1.5, the decreasing trend of [Cr/Fe] with decreasing [Fe/H] found for red giants could probably be removed if NLTE correction on the Cr abundances from Cr I lines is included. It is noticed that P18 tends to reproduce the increase of [Mn/Fe] with metallicity at [Fe/H] > -2.0, which is due to the metallicity-dependent yields of Mn from massive stars for the P18 model.

The Co abundance trends seem to be the most difficult case among the iron-peak group, where neither model succeeds to explain the observed trend well. In previous studies, one major puzzle of Co evolution that theoretical models fail to reproduce is the observed increasing trend at [Fe/H] < -2.5 with decreasing [Fe/H]. However, as shown in Figure 18, the slopes of the observed trend in both giants and turnoff stars in our sample are respectively -0.06 and -0.05, not indicating very clear rising trends as observed in previous studies (e.g., FS and other observations compared in R10, K20, and P18). Therefore, the main discrepancy seen here is the Co underproduction in the models, which could become even more significant after considering NLTE corrections (e.g., Figure 15 in R10 paper). The difference may be weakened through enhanced explosion energies which may lead to higher Co production in low-metallicity and high-mass stars (see Umeda & Nomoto 2005; Nomoto et al. 2013, etc., for the discussion)

P18 fails to reproduce the observed trend for Zn, presenting significant underproduction, which seems to be a common feature of the yields from Woosley & Weaver (1995) and Nomoto et al. (2013). In general, all compared models tend to predict a rather flat trend of [Zn/Fe] towards the extremely low-metallicity region. This is inconsistent with the observed increasing trend with decreasing [Fe/H], which may imply that the fraction of HNe/high-energy SN has been larger in the early stages of the Galaxy evolution. For example, as tested by Kobayashi et al. (2020), if large fraction of HNe is applied, the GCE model predicts a typical [Zn/Fe] ratio of about 0.2 in a wide range of metallicity, which is in good agreement with our observation (as described in § 3.1.5). On the other hand, with a metallicity-dependent HNe fraction, the predicted [Zn/Fe] ratio may continuously decrease towards [Fe/H] > -1.0, presenting much lower values than observations (e.g., Saito et al. 2009). In that sense, more realistic modeling of synthesis of Zn in supernova explosions, as well as chemodynamical simulations (e.g., Kobayashi & Nakasato 2011), may be required to better reproduce the observation. Also, synthesis of Zn in a variety of supernova explosions (e.g. hypernovae, electron-capture supernovae) have been explored to solve the problem, (e.g., Nomoto et al. 2013; Hirai et al. 2018). For example, such trend can be explained with the dependence of the swept-up H mass on the explosion energy (e.g., Umeda & Nomoto 2005, Tominaga et al. 2007) and also indicate that the environment is not well mixed, which cannot be reproduced with a one-zone model in all models adopted here.

To briefly summarize, the models are in agreement with the abundance trend for some key elements, including Na, Mg, Si, Ca, Cr, Mn, and Ni, though there remain difficulties to fully explain the

observed slope. For some cases, such discrepancy may have been caused by technical issues of abundance measurements, such as NLTE effect (e.g., for the positive trend of [Cr I/Fe] among giants). Stellar evolution on the upper red-giant branch could affect surface carbon abundances. Some other cases like the decreasing trend of [Mg/Fe] and [Si/Fe] at [Fe/H] > -2.5 would be explained by taking the assembly (dynamical) process of the Milky Way formation into consideration. On the other hand, serious disagreements exist between observations and models for some elements, such as Sc, Ti, V, and Co, which would require further updates of nucleosynthesis yields. It should be kept in mind that the three selected models (the majority of theoretical studies) have been made under the framework of one-zone model (for the local halo), which is based on the assumption of a unique relation between the metallicity (e.g., [Fe/H]) and time, and is thus clearly an oversimplification of the real situation. For example, due to the well-known large scatter in the age-metallicity relation of field stars, it is difficult to define at what metallicity a long-lived source, e.g., AGB stars, started to enrich the Galactic interstellar medium. Comparisons of the observations with the results of recent chemo-dynamic simulations will be helpful to examine these effects.

3.3. Abundance correlations

Correlations among different species are able to reflect the relation between the site or mechanisms that produce these elements. We here present the abundance correlations among α -elements, Sc, and Zn, as well as correlations among the six heavy elements that have been measured for this sample, aiming at exploring the relations and differences of the origins of these species (Figures 22 and 23). Note that when discussing about the abundance correlations, we have excluded program stars that are located beyond 3σ of the abundance trend as defined in § 3.1, and thus the following discussion is based on the bulk of the sample which are regarded the so-called “general” population of VMP/EMP stars. In Figures 22 and 23, however, objects excluded from the statistics are also shown by open circles for completeness.

Figure 22 shows correlations of abundances between α -elements, Sc and Zn, which are key elements to constrain the early star formation history and the properties of core-collapse supernovae. Correlations between the four α -elements (Mg, Si, Ca and Ti) are clearly seen, which is expected from the (relevant) production sites of these species. More detailed inspection reveals that correlations between Mg and Si, and between Ca and Ti are stronger, whereas correlations between Mg (or Si) and Ca (or Ti) are weaker or insignificant. This suggests that the origins between the two lighter elements (Mg and Si) and heavier ones (Ca and Ti) are similar with each other, but slightly different between the two groups. This is also expected from theories of massive star evolution and supernova explosions: Mg mainly comes from hydrostatic carbon burning and explosive Ne burning; Si is mostly produced during hydrostatic burning and explosive O burning; Ca is directly contributed from explosive incomplete Si and O burning; the main isotope of Ti (^{48}Ti) is mainly synthesized during explosive complete and incomplete Si burning (Woosley & Weaver 1995; Chieffi et al. 1998; Kobayashi et al. 2006).

Interestingly, Sc abundances show relatively strong correlations with all the four α -elements. This correlation would support the prediction by nucleosynthesis models that Sc is produced both during Ne burning and in explosive O and Si burning, which shares similar origins with these α -elements. The slight overabundance in Sc is also in agreement with the general overabundance in α -elements as seen in Figure 15. A correlation is also found between Zn and Ti, whereas the correlation is not clear between Zn and other α -elements. Note that Zn is mainly produced during explosive complete

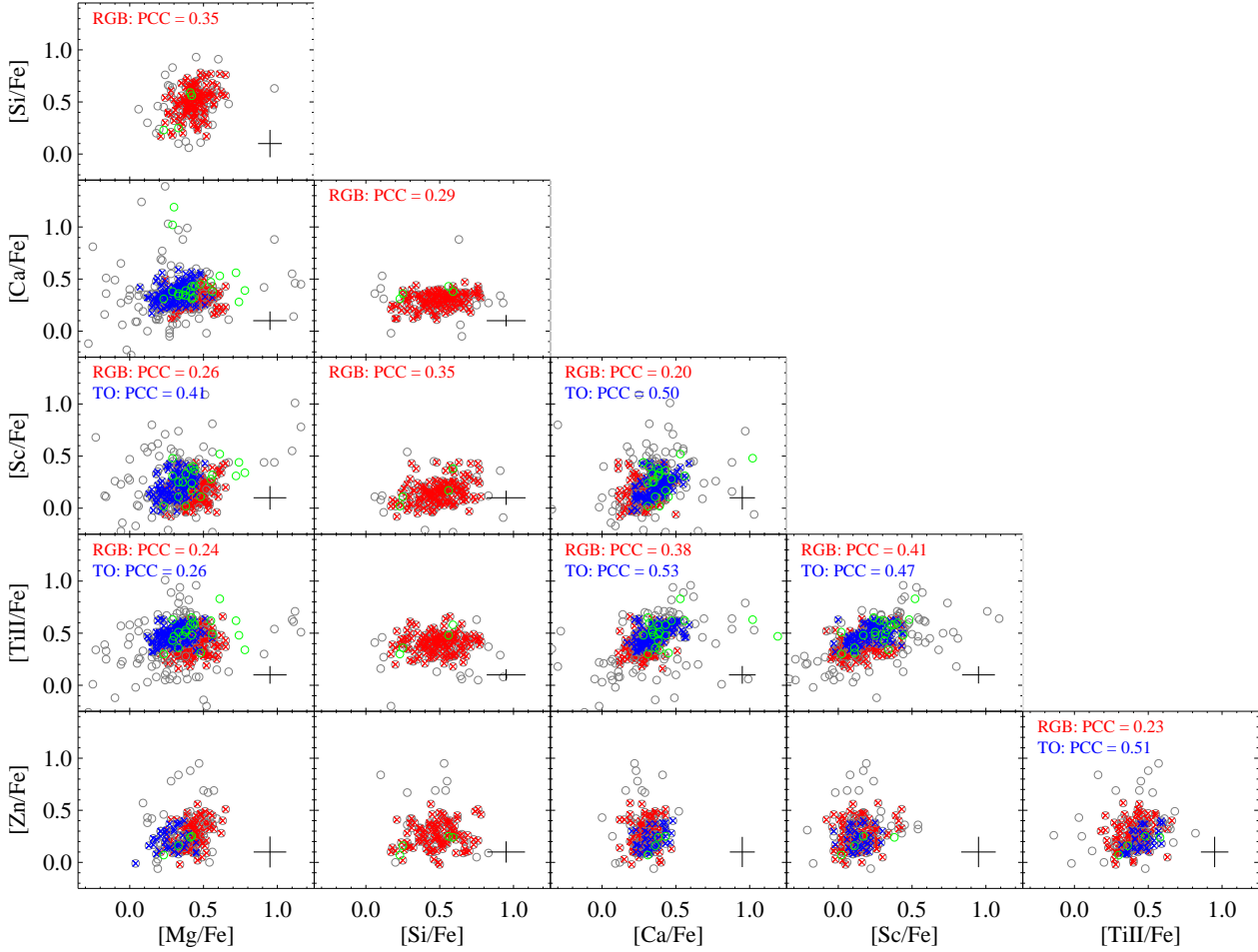


Figure 22. Abundance correlation between α -elements, Sc and Zn. The Pearson correlation coefficient (PCC) calculated for each set is presented in the plot in cases that exhibit potential correlation, e.g., $\text{PCC} > 0.20$, separately for giant (red) and turnoff (blue) stars. Open circles indicate objects whose abundance ratios are beyond the 3σ of the general trend of $[\text{X}/\text{Fe}]$ and are thus excluded for the calculation of the correlation (see text). Horizontal-branch stars (green) are also shown here for reference.

Si burning, which is similar to the production site of Ti. Moreover, with the higher explosion energy, the explosive O and incomplete Si burning layers just shift, while the complete Si burning layer increases. This may explain the unclear correlation between Zn and the other three elements (Mg, Si, and Ca).

Abundance correlation among Sr, Y, Zr, Ba, La, and Eu are presented in Figure 23. Correlations are found between most of these six heavy elements, and a stronger correlation is usually detected between elements having similar atomic numbers, i.e., relatively stronger correlation between the lighter neutron-capture elements Sr and Y, and that between the heavier ones Ba and Eu. This strong correlation between elements with similar atomic (mass) numbers reflect the nuclear physics. The weak, or non-detectable, correlations between lighter and heavier neutron-capture elements suggest variations of conditions in the nucleosynthesis sites, or contributions of more than one processes.

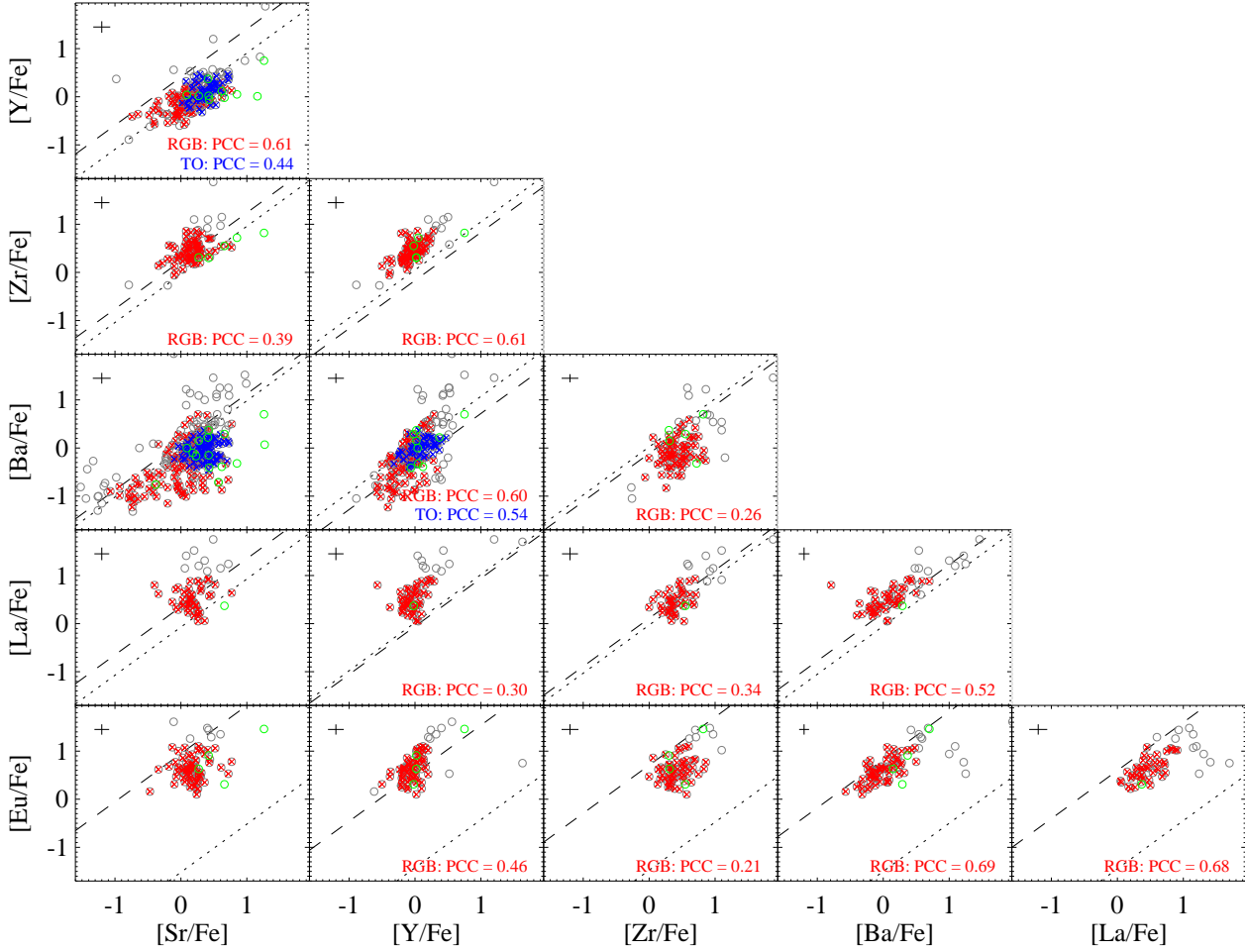


Figure 23. Abundance correlation between heavy elements Sr, Y, Zr, Ba, La, and Eu. Definition of symbols are the same as that of Figure 22. The dashed and dotted lines represent the abundance ratios of the r -process and s -process components in solar-system material, respectively.

We note again that the correlation between Ba and Eu abundances can be studied only for objects with Eu measurements, i.e. those having relatively high abundances of neutron-capture elements. Whereas the Ba and Eu abundances of most of these stars are well explained by the r -process, no useful information is obtained for other stars from our sample.

As reported by previous studies, abundance ratios between Ba and lanthanides show clear correlations following the r -process ratios, where $[\text{Ba}/\text{Eu}]$ and $[\text{La}/\text{Eu}]$ are excellent indicators to distinguish contributions of the r - and s -processes. Among them, the $[\text{La}/\text{Eu}]$ ratios show a small departure from the solar r -process ratio (Fig. 23, which suggests partial contribution from the s -process). No signature of s -process contribution is, however, found in the $[\text{Ba}/\text{Eu}]$ ratios. Further studies are required to understand the departure of $[\text{La}/\text{Eu}]$ ratios in these stars.

Among the abundance ratios between light neutron-capture elements, $[\text{Sr}/\text{Y}]$ ratios better agree with the solar s -process ratio than that of the r -process (e.g., see Simmerer et al. 2004, for the solar s - and r - process ratios). On the other hand, the $[\text{Zr}/\text{Y}]$ ratios are even higher than those

of the s -process as well as of the r -process. Hence, we are not able to conclude which process can better explain the abundance ratios of these light neutron-capture elements. A clear observational result is that Y is underabundant compared to Zr. This could be a constraint on nucleosynthesis models that is responsible for light neutron-capture elements in the early stage of chemical evolution, which would be different from the usual r -process (e.g., Travaglio et al. 2004; Wanajo & Ishimaru 2006).

3.4. CEMP stars

A remarkable feature found in very metal-poor stars is the high frequency of objects with high carbon abundances, called carbon-enhanced metal-poor (CEMP) stars. Previous studies have reported that the frequency is as high as 20% in the metallicity range of $[\text{Fe}/\text{H}] < -2$, and it increases with decreasing metallicity (e.g., Placco et al. 2014a). The dependence of the CEMP frequency on the distribution in the Milky Way halo has been also studied based on large spectroscopic survey data, reporting higher frequency in the outer halo region (Lee et al. 2017). CEMP stars are classified into s -process-enhanced ones (CEMP-s) characterized by high Ba abundances, those with low Ba abundance (CEMP-no), and other minor sub-classes (e.g., Beers & Christlieb 2005).

Figure 24 (top and middle) shows carbon abundance ratio ($[\text{C}/\text{Fe}]$) as a function of luminosity (Table 2) and metallicity ($[\text{Fe}/\text{H}]$), separating the objects into turnoff stars (filled circles) and red giants (open circles). The CEMP criterion given in § 3.1.2 is shown by the dotted line in the top panel.

Carbon abundances are determined from the CH bands at around 4315 and 4322 Å for 281 objects in the present work. The numbers of turnoff stars and giants for which carbon abundances are determined are 109 and 172, respectively (Table 8). The CH molecular band is not detected in spectra of the remaining stars, for which upper-limit is estimated by comparison of synthetic spectra with the observed ones. The molecular absorption is weaker in general in turnoff stars, and, hence, the upper limit of carbon abundances estimated for objects with no detection of the CH bands are relatively high, in particular for extremely metal-poor stars. The limit of carbon abundances ($[\text{C}/\text{H}]$) for which the CH band is detectable is shown in Figure 16. Among the objects for which upper limits of carbon abundances are determined, most of the giants and some turnoff stars have the upper limits lower than the criterion for CEMP stars (see Table 8).

In Figure 24 (middle and bottom), CEMP stars with large excess of Ba ($[\text{Ba}/\text{Fe}] > 1$; CEMP-s stars) are indicated by large open circles whereas objects with lower Ba abundances, including those having upper-limit of $[\text{Ba}/\text{Fe}]$ lower than this criterion, are shown by large squares. The numbers of CEMP-s and CEMP-no stars are given in Table 8. CEMP stars with no useful constraint on Ba abundances are indicated in the figure by large open triangles overplotted. Most of these objects are main-sequence turn-off stars with extremely low metallicity ($[\text{Fe}/\text{H}] \lesssim -3$), for which high SNR spectra are required to determine Ba abundances if Ba is not enhanced ($[\text{Ba}/\text{Fe}] < 1$).

The numbers of CEMP-s turnoff stars and giants are 8 and 2, respectively. Four of the turnoff stars have very high $[\text{C}/\text{Fe}]$ values (> 2). The $[\text{C}/\text{Fe}]$ values of others are not extreme, but some of these stars have high $A(\text{C})$ values given the relatively high metallicity (the lower panel of Figure 24). Their high carbon abundance corresponds to the CEMP Group I stars in the classification by Yoon et al. (2016).

By contrast, most of the CEMP-no stars (20 turnoff stars and 9 giants) have $[\text{C}/\text{Fe}]$ (and $[\text{C}/\text{H}]$) not as high as those of CEMP-s stars. This is known as the feature of Group II and III in Yoon et al.

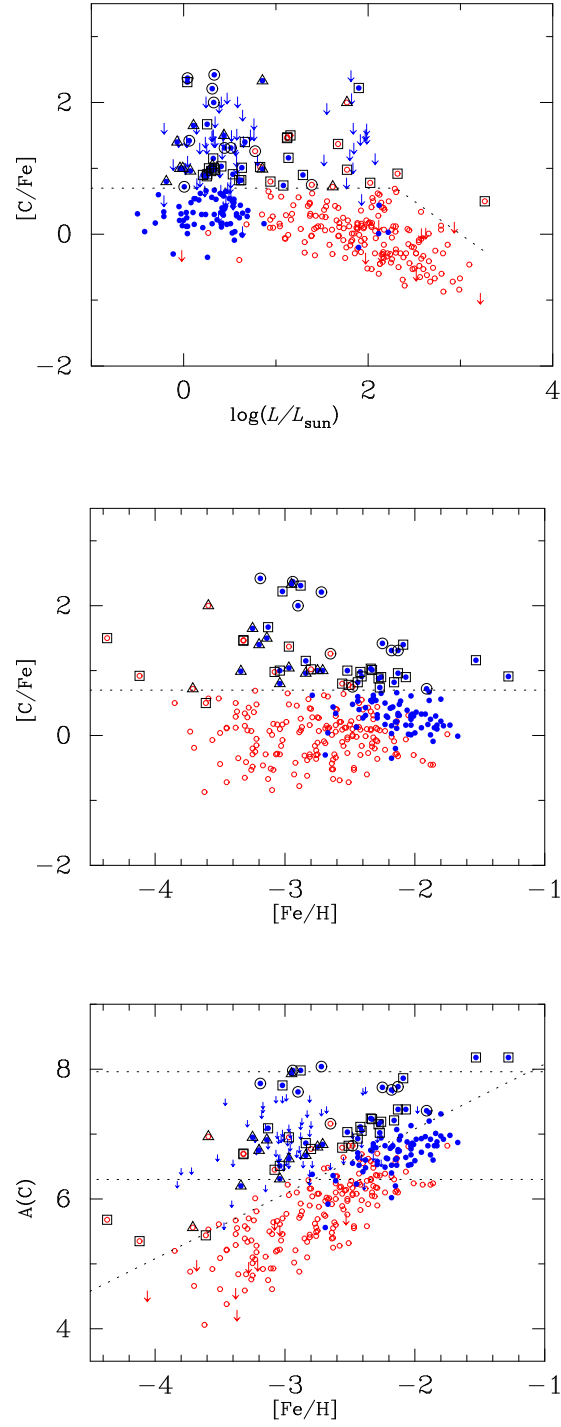


Figure 24. (top) $[C/Fe]$ as a function of luminosity for our sample. Filled (blue) and open (red) circles indicate warm turnoff stars ($T_{\text{eff}} > 5500$ K) and cool giants, respectively. CEMP-s and CEMP-no stars are indicated by large circles and squares, respectively. Triangles mean CEMP stars for which classification is not available. Arrows mean upper limits. The dotted line indicates that criterion of CEMP stars. (middle and bottom) $[C/Fe]$ and $A(C)$ as a function of $[Fe/H]$ for our sample with the same symbols for the top panel.

(2016). The distribution of these stars extends to extremely low metallicity ($[\text{Fe}/\text{H}] < -3.5$), whereas that of CEMP-s stars show lower bound at around $[\text{Fe}/\text{H}] = -3$. Many CEMP-no stars are also found in $[\text{Fe}/\text{H}] > -2.5$ in our sample. This is not the case of the sample of Aoki et al. (2007), who discussed that CEMP-no stars appear at lower metallicity. This would be due to a bias in their sample selection. The present work includes many turnoff stars with $[\text{Fe}/\text{H}] > -2.5$, some of which have slightly higher $[\text{C}/\text{Fe}]$ than the CEMP criterion. Such stars are not well covered by Aoki et al. (2007) who focused on stars with strong CH bands. Indeed, ten of the 14 CEMP-no turnoff stars with $[\text{Fe}/\text{H}] > -2.5$ have $0.7 < [\text{C}/\text{Fe}] < 1.0$ in our sample. These stars have similar abundance ratios (e.g., α/Fe) to those of non-CEMP stars.

Most of the CEMP stars for which Ba abundances are not determined are turnoff stars having $[\text{Fe}/\text{H}] \sim -3$ and $[\text{C}/\text{Fe}] < 2$. The distribution of Fe and C abundances overlaps with that of CEMP-no stars, suggesting that most of them are CEMP-no objects.

The fraction of CEMP stars among giants is $14/179 = 7.8\%$. We note that six objects among the seven for which CH band is not detected have upper limits of carbon abundance lower than the CEMP criterion. Hence, the estimate is not affected by the detection limit of CH bands for giants.

The fraction of CEMP turnoff stars is nominally $37/120 = 31\%$. Nine objects with the upper limit of $[\text{C}/\text{Fe}] < 0.7$ are included in C-normal stars in this calculation. If all other stars for which CH bands are not detected are assumed not to be carbon-enhanced, the fraction is $37/172 = 22\%$. This could be the lower limit of the frequency of CEMP stars in turnoff stars. It should also be noted that there are many CEMP stars with $[\text{C}/\text{Fe}]$ close to the criterion. This is found in the previous sample as the Group II stars of Yoon et al. (2016). If we adopt $[\text{C}/\text{Fe}] = +1$ as the criterion, the CEMP fraction in turnoff stars decreases to 11%.

Even if these factors are taken into consideration, the frequency of CEMP stars is higher in turnoff stars than in giants. In particular, the frequency of CEMP-s stars is clearly high in turnoff stars, and the excess of carbon in most of them is remarkable (i.e. Group I stars). The origin of carbon excess of CEMP-s stars is presumed to be mass transfer from companion AGB stars. The accreted carbon-rich material could be significantly diluted in the stellar envelope in giants. If the mixing during the turn-off phase is not effective, carbon abundances are expected to be higher in turn-off stars than in giants. An extreme example of CEMP main-sequence turn-off star is J0119-0121 which has $[\text{C}/\text{Fe}] = +2.4$ and $[\text{Fe}/\text{H}] = -3.2$. This star was studied by Zhang et al. (2019) as an extreme CEMP-s star having the largest excess of neutron-capture elements ($[\text{Ba}/\text{Fe}] = +2.6$) with the abundance pattern well explained by the s-process. There are three other CEMP-s turnoff stars that have similarly large excess of carbon (J0824+3025, J0949+2707 and J1020+4046), though the excess of Ba shows wide distribution. No such extreme object is found among CEMP-s giants in our sample: the giant having the highest $[\text{C}/\text{Fe}]$ is J2257+3859 ($[\text{C}/\text{Fe}] = 1.3$). We note that mixing during turn-off phase is proposed for carbon-enhanced stars by mass accretion (e.g., thermohaline mixing, Stancliffe et al. (2007)). Our result does not deny existence of such mixing, but suggests that such mixing is not effective in many cases of carbon-enhanced turn-off stars.

The frequency of CEMP-no turnoff stars is also higher than CEMP-no giants, although the contrast is not as significant as found for CEMP-s stars. CEMP-no stars have been interpreted as stars formed from C-enhanced cloud to which some progenitors (e.g., faint supernovae, rotating massive stars) have contributed (e.g., Meynet et al. 2006; Tominaga et al. 2014). Even in such cases, the surface C abundances might be reduced in highly evolved red giants as suggested from C-normal red

Table 8. Numbers of CEMP and C-normal stars

	Giants ^a	turnoff ^a
CEMP-s	2(1)	8(5)
CEMP-no	8(5)	19(8)
CEMP (unclassified)	2(2)	10(6)
C-normal ^b	160 + 6	72 + 11
C upper-limit ^c	1	52

^aNumbers of objects showing radial velocity variations in parenthesis

^bIncluding objects with [C/Fe] upper-limit lower than the CEMP criterion

^cObjects with [C/Fe] upper-limit higher than the CEMP criterion

giants (§ 3.1). The C abundances of about half of CEMP-no turnoff stars is $0.7 < [\text{C}/\text{Fe}] < 1.0$. This relatively small excess could be erased by mixing with internal material affected by the CNO-cycle, resulting in lower frequency of CEMP-no stars in evolved giants.

An alternative possibility is that some of the CEMP-no stars have been formed by mass-accretion of C-enhanced material from companion AGB stars in which s-process is not active (Suda et al. 2004). The surface C-enhanced material could be diluted through the first dredge-up as in the case of CEMP-s stars. To confirm this possibility, radial velocity monitoring to examine the binarity for these stars is useful. Paper I reports radial velocity variations from the measurements with LAMOST and Subaru. Although the measurements are not sufficient to definitively identify binary systems for most of the stars in our sample, the fraction of stars with radial velocity variations would provide some hint on the binary frequency of each class of CEMP stars. The number of stars that show radial velocity variations larger than 20 km s^{-1} is given in Table 8. More than half of CEMP-s stars show radial velocity variations, supporting the scenario that carbon-excesses are caused by mass transfer in binary systems. Interestingly, the fraction of stars showing radial velocity variations is about half also in CEMP-no stars. This is higher than the fraction for the whole sample reported in Paper I (35%). This result might support the scenario that some of CEMP-no stars are also formed through binary mass transfer. It should be noted that the fraction is also quite high in CEMP stars that are yet classified (8/12). Binaries of CEMP-s and CEMP-no stars have also been investigated in previous studies, e.g., Hansen et al. (2016a) and Hansen et al. (2016b) which have discovered a binary fraction of 82% and 17% respectively for extremely metal-poor CEMP-s and CEMP-no stars. Our results are consistent in the fact that such fraction is higher in CEMP-s than CEMP-no stars, though showing different fractions for each class, which may be caused by different metallicity coverage of the two works, and inclusion of more moderately C-enhanced stars in our sample.

There are two CEMP-no turnoff stars with $[\text{C}/\text{Fe}] > 2$ showing no excess of Ba (J0150+2149 and J1313–0552). The carbon-excess of these stars is as large as the “physically motivated” criterion of C-Enhanced EMP stars ($[\text{C}/\text{Fe}] = +2.3$) proposed by Chiaki et al. (2017), above which carbon grains are dominant coolant in the process of low-mass star formation. Further studies of detailed abundance patterns of these stars would be useful to constrain the condition of star formation in the early Galaxy.

3.5. α -peculiar stars

As shown in Figure 25, the bulk of metal-poor stars in our sample present similar overabundance of α elements (e.g., $[\text{Mg}/\text{Fe}] \sim 0.35$) with small scatter. However, a small number of stars deviate from the majority by showing extreme enhancement or significant deficiency in α -element abundances. For example, there are 11 program stars showing sub-solar Mg abundances with $[\text{Mg}/\text{Fe}] < 0$ (hereafter the “Mg-poor” stars), and four objects showing extreme enhancement in Mg with $[\text{Mg}/\text{Fe}] > 1$ (hereafter the “Mg-rich” stars). The Mg-poor stars cover the metallicity range from $[\text{Fe}/\text{H}] = -3.7$ to -2.3 , overlapping with the majority of the sample which shows typical enhancement of $[\text{Mg}/\text{Fe}] \sim 0.3 \sim 0.4$ (as shown in § 3.1). Our discovery of three Mg-poor stars with $[\text{Fe}/\text{H}] < -3.1$ extends the distribution of such objects to lower metallicity region. Although no Mg-poor stars with $[\text{Fe}/\text{H}] < -3.8$ have yet been found in either our sample or previous studies, this could probably be due to the limited sample size of such extremely low-metallicity stars as well as the rarity of Mg-poor stars. Larger sample of EMP stars with $[\text{Fe}/\text{H}] < -3.8$ will be necessary to determine or better constrain whether there exist a lower limit in metallicity for such Mg-poor stars.

The Mg-rich stars with $[\text{Mg}/\text{Fe}] > 1.0$ distribute in the metallicity range from -4.1 to -2.9 dex, consistent with previously known metal-poor stars with extremely enhanced Mg (e.g., CS22949–037: Norris et al. 2002; CS 29498–043: Aoki et al. 2002). It is interesting that most outliers for Mg have normal Ca abundances, resulting in a large scatter in the plot of $[\text{Mg}/\text{Ca}]$ as a function of metallicity (see Figure 26). The $[\text{Ca}/\text{Fe}]$ of Mg-rich stars are only slightly higher than that of the comparison stars (see below for more details). Only three Mg-poor stars have sub-solar $[\text{Ca}/\text{Fe}]$, one of which presents the lowest Mg abundance among our sample (J1220+1637: $[\text{Mg}/\text{Fe}] = -0.45$), as well as a relatively low Ca abundance ($[\text{Ca}/\text{Fe}] = -0.34$) in comparison with other stars around this low metallicity ($[\text{Fe}/\text{H}] = -2.72$). The other two Mg-poor stars (J1542+2115 and J1349+1551) also have sub-solar $[\text{Ca}/\text{Fe}]$ ratios. For J1349+1551, however, the Ca abundance is more deficient than that of Mg, making it a unique Mg-poor star with a positive $[\text{Mg}/\text{Ca}]$.

On the other hand, there are a few Ca-peculiar stars showing relatively high or sub-solar $[\text{Ca}/\text{Fe}]$ ratios but with normal Mg abundances. However, most of their Ca abundances are determined from the single Ca I line at 4226 Å, which are not as reliable as abundances determined from more than one Ca lines. Therefore for this work, we only consider Mg-poor and Mg-rich stars as candidate α -peculiar objects. The absorption lines of Mg have been visually checked for each object to ensure their distinctive $[\text{Mg}/\text{Fe}]$ ratios.

The 11 Mg-poor program stars include five EMP and six VMP stars. Stars with similarly deficiency in Mg have been found in the field halo (e.g., Ivans et al. 2003; Aoki et al. 2014) and nearby dwarf spheroidal galaxies (e.g., Tolstoy et al. 2009; Shetrone et al. 2003). Ivans et al. (2003) suggests that these objects would have been formed in environment with larger contributions from SN Ia yields in comparison with other halo stars with similar metallicities. Since Mg is mainly produced during massive star evolution while Ca is produced by both type Ia and type II SN, Mg is expected to be more deficient than Ca in this scenario. As shown in the right panel of Figure 26, most of the Mg-poor stars in our sample have sub-solar $[\text{Mg}/\text{Ca}]$ ratios, which is consistent with increased contribution from SN Ia. However, J0908+3119, the most metal-poor object in our Mg-poor stars has a metallicity of $[\text{Fe}/\text{H}] = -3.74$, and there are four other Mg-poor EMP stars in our sample. It is not clear whether SN Ia could have significantly contributed to stars with such extremely low metallicity, because the time-scale of the contribution of SN Ia to chemical evolution is much longer

than that of SN II. A possible scenario is that these Mg-poor stars are originated from classical or ultra-faint dwarf galaxies that had very low star formation rates. In such stellar systems, the onset of SN Ia might occur at much lower metallicities than that in the MW. Indeed, EMP α -poor stars have been found in some dwarf galaxies (e.g., [Aoki et al. 2009b](#)). The [Mn/Fe] ratios are expected to be low for stars formed from cloud enriched only by SN II (e.g., [Tominaga et al. 2014](#)). J1542+2115 ([Fe/H]= -3.07) is the only one with Mn measurement in our Mg-poor sample. Its relatively high [Mn/Fe] in comparison with other EMP stars implies that SN Ia may have enriched the gas before the formation of some EMP stars. Similar low Mg abundances have been found in two EMP stars by [Caffau et al. \(2013\)](#). They also suggest that contributions from SN Ia are responsible for the Mg deficiencies. On the other hand, [Kobayashi et al. \(2014\)](#) argued that the yields of core-collapse supernovae, i.e. 13-25 M_{\odot} SN, could explain the low [Mg/Fe] ratios of EMP stars from [Caffau et al. \(2013\)](#) without contribution from SN Ia, although very low [Mn/Fe] ratios are still predicted by their models. In addition, Pair-instability supernovae (PISN) could also lead to sub-solar [Mg/Fe] in VMP stars by contributing larger amount of iron than core-collapse supernovae ([Aoki et al. 2014](#)). [Takahashi et al. \(2018\)](#) demonstrated that high [Ca/Mg] $\sim 0.5 - 1.3$ abundance ratios could be prominent PISN signatures compared with abundances of normal metal-poor star, which have been found in four of our Mg-poor stars. However, extremely low [C/Fe] and [Na/Fe] abundances are expected to be produced by PISN in the meanwhile, which have not been discovered in our Mg-poor sample stars.

The Mg-poor sample collected by [Ivans et al. \(2003\)](#) shows unusually low abundances of Na, Sr, and Ba with respect to Fe, e.g., the average [(Sr,Ba)/Fe] is more than 1.0 dex lower than the typical values, indicating possible association between the low-[Mg/Fe] ratios and the low [Sr/Fe] (and [Ba/Fe]). However, recent discoveries on Mg-poor stars (e.g., [Xing et al. 2019](#); [Sakari et al. 2019](#); [Ezzeddine et al. 2020](#)) suggest that these objects do not necessarily to be deficient in Sr and Ba, and they could be with normal abundances of neutron-capture elements, or even r -process enhanced. As shown in [Figure 25](#), the Mg-poor stars in our sample consists of objects with both normal and deficient Na and Sr abundances. No r -process enhanced Mg-poor stars have been found in our sample, which may be due to the rarity of such objects.

The fraction of Mg-rich stars in our sample is about 1.0% (four out of 385). All of them are enhanced in Na (with the NLTE corrected [Na/Fe] > 1 for three of them, as seen in [Figure 25](#)), while their Ca abundances seem to be normal, leading to high [Mg/Ca] ratios. Such high [Mg/Ca] and [Na/Fe] have been found by previous studies for a couple of halo stars: e.g., CS 22949-037 ([Mg/Ca]=1.2; [Norris et al. 2002](#), [Na/Fe]=1.57; [Andrievsky et al. 2007](#)), HE 1327-2326 ([Mg/Ca]=0.99, [Na/Fe]=0.94; [Frebel et al. 2008](#)), and J 2217+2104 ([Mg/Ca]=1.3, [Na/Fe]=1.33; [Aoki et al. 2018](#)) that is also included in our sample, suggesting that there exist a population of EMP Mg-rich stars. Several stars with high [Mg/Ca] ratios have also been discovered in the ultra faint dwarf galaxy Hercules ([Koch et al. 2008](#)) and Grus II ([Hansen et al. 2020](#)). Both of these two studies argue that the property of metal-poor stars with high [Mg/Ca] ratios may be caused by massive ($\geq 20M_{\odot}$) stars. Moreover, all of the four Mg-rich stars in our sample are also highly enhanced in C, with the [C/Fe] ratios ranging from 0.92 to 2.42 dex. Two of them are CEMP-s stars with enhanced Ba abundances ([Ba/Fe] > 1). Only one of these four stars, J2217+2104 does not possess large [Sr/Fe] or [Ba/Fe], but rather shows significantly low [Sr/Fe] and [Ba/Fe] in comparison with other known

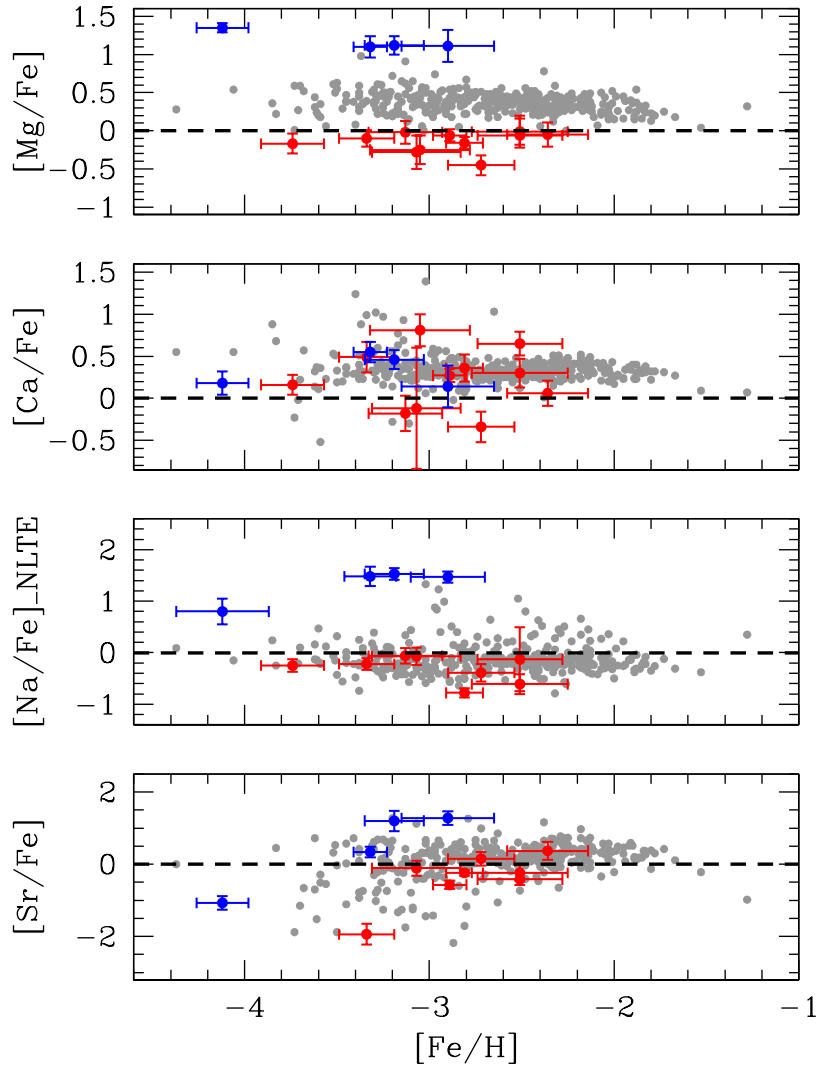


Figure 25. Comparison of Mg, Ca, Na (NLTE corrected) and Sr of Mg-poor stars (filled red circles) and Mg-rich stars (filled blue circles) with those of other metal-poor stars (filled gray circles) in our sample.

Mg-rich CEMP stars, suggesting that the excess of C and Mg may not be caused by the event related to neutron-capture processes (Aoki et al. 2018).

3.6. Abundance distributions of neutron capture elements

We here focus on the three neutron-capture elements Sr, Ba and Eu, which are measured in a relatively large number of stars in our sample. These are also key elements to constrain the nucleosynthesis processes that produce heavy elements in the universe. Detailed abundance patterns of neutron-capture elements that are determined for a small number of stars will be discussed separately in a future work in this series.

3.6.1. Eu-rich stars

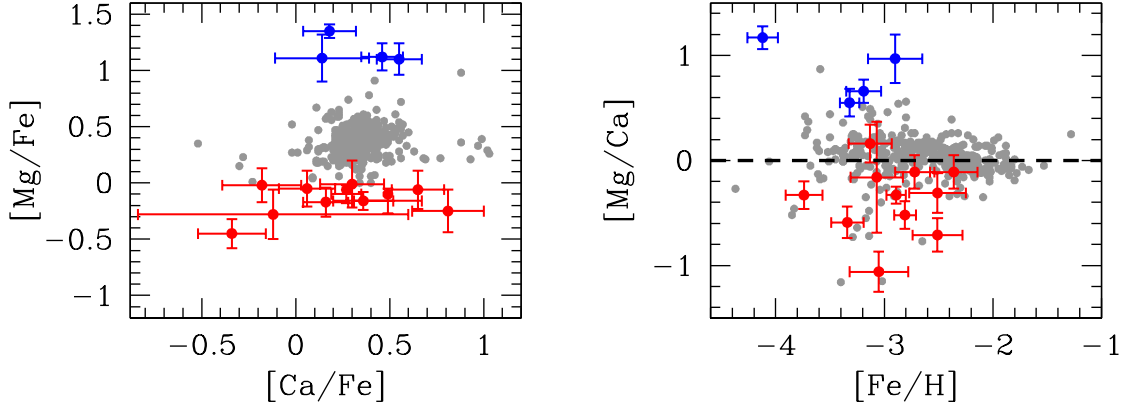


Figure 26. Left: $[\text{Mg}/\text{Fe}]$ as a function of $[\text{Ca}/\text{Fe}]$. Right: $[\text{Mg}/\text{Ca}]$ versus $[\text{Fe}/\text{H}]$. The same symbols are used as in Figure 25.

Eu abundances are determined for 79 stars in our sample. Since Eu is not as abundant as Sr or Ba, it is detectable only for cool giants or Eu-enhanced warm stars among our sample. Figure 27(a) shows the $[\text{Eu}/\text{Fe}]$ values as a function of $[\text{Fe}/\text{H}]$. As seen in this figure, Eu is detected in only several stars in $[\text{Fe}/\text{H}] < -3$.

Twelve stars are identified to have $[\text{Eu}/\text{Fe}] > +1$ and $[\text{Ba}/\text{Eu}] < 0$ (Figure 27b). There is no evidence of carbon-excess for these stars. These stars are classified into “r-II stars” (Beers & Christlieb 2005) whose heavy elements are enhanced by the r-process (filled symbols in Figure 27a,b). Similarly, the objects with $[\text{Eu}/\text{Fe}] > +0.5$ and $[\text{Ba}/\text{Eu}] < 0$ are classified into “r-I stars” (plus symbols in the figure). There are 34 such objects in our sample.

The $[\text{Fe}/\text{H}]$ values of the four most Eu-enhanced stars are lower than -2.5 . J 1109+0754 is one of the most metal-poor example of r-II stars known to date ($[\text{Eu}/\text{Fe}] = +1.4$ and $[\text{Fe}/\text{H}] = -3.3$). The detailed abundances of this object will be reported separately (Honda et al., in preparation). The abundances of this object have also been reported by Li et al. (2015b) and Mardini et al. (2020). Very recently, Yong et al. (2021b) reported the discovery of an r-II star with $[\text{Fe}/\text{H}] = -3.5$, for which they suggest a magnetorotational hypernova as the progenitor, taking the long delay time expected for binary neutron star merger events into consideration. The low-metallicity tail of the metallicity distribution of r-II stars would be a key to constraining the origin of the r-process in the early Universe.

Other four r-II stars have $-2.5 < [\text{Fe}/\text{H}] < -2.0$, and the $[\text{Eu}/\text{Fe}]$ values are between 1.0 and 1.2. Such less metal-poor r-II stars have been identified by recent studies (e.g., Roederer et al. 2018; Xing et al. 2019), indicating the existence of efficient processes to enrich r-process elements in ISM at this metallicity.

The frequency of r-II stars estimated by previous studies is 3-5% (e.g., Barklem et al. 2005). The frequency of r-II stars in our sample is $12/380 \sim 3\%$, which is similar to, or slightly lower than the previous estimates. The value is, however, should be a lower limit because there could be many warm stars that have high Eu abundances but their Eu lines are yet detected due to the limitation of data quality. The frequency could be better estimated for giants, in which Eu is detectable in most cases if it is enhanced. The frequency of stars with $[\text{Eu}/\text{Fe}] > +1$ is $10/211$ ($\sim 5\%$) for giants. We note

that the two r-II main-sequence turn-off stars found in this study are J0948+0000 ($[\text{Eu}/\text{Fe}] = +1.5$ and $[\text{Fe}/\text{H}] = -2.8$) and J1044+3713 ($[\text{Eu}/\text{Fe}] = +1.0$ and $[\text{Fe}/\text{H}] = -2.0$).

3.6.2. Sr and Ba abundances

Ba and Sr are detected in most of the stars in our sample, i.e., 318 and 362 stars for Ba and Sr, respectively, of the 385 stars, thanks to the existence of strong resonance lines in the optical range. Note that we include the remaining stars in the discussion on Sr and Ba deficient stars below. The Ba and Sr abundances as a function of $[\text{Fe}/\text{H}]$ are shown in Figure 27(c). The objects with highest Ba abundances ($[\text{Ba}/\text{Fe}] > 2$) are CEMP-s stars (triangles). The r-II stars discussed above (filled circles) have $0.5 < [\text{Ba}/\text{Fe}] < 1.0$ as expected from the high Eu abundance ($[\text{Eu}/\text{Fe}] > 1$) and the r-process abundance ratio ($[\text{Ba}/\text{Eu}] \sim -0.7$). The r-I stars (plus symbols with open circles) have Ba abundances that are almost indistinguishable from most of the other stars.

Excluding the CEMP-s and r-II stars, a majority of stars in our sample have $[\text{Ba}/\text{Fe}] \sim 0$ with some increasing trend with increasing metallicity as already pointed out in § 3.1. There are, however, some fraction of stars that have very low Ba abundances ($[\text{Ba}/\text{Fe}] < -0.5$). These stars are discussed below. The Sr abundances also show a wide distribution like Ba (Figure 27(e)). Majority of stars have $[\text{Sr}/\text{Fe}] = 0.0\text{--}0.5$ and show no clear trend for metallicity. The CEMP-s stars and r-II stars are not well separated from the bulk of the other stars in the $[\text{Sr}/\text{Fe}]$ distribution. This indicates that light neutron-capture elements are not enhanced as significantly as heavy neutron-capture elements by the r-process and the main s-process, and that another source of these light neutron-capture elements plays more important role at such very low metallicity. There are also a small fraction of stars that have very low $[\text{Sr}/\text{Fe}]$ as found for $[\text{Ba}/\text{Fe}]$.

Figures 27(d and f) show $[\text{Sr}/\text{Ba}]$ as functions of $[\text{Fe}/\text{H}]$ and $[\text{Ba}/\text{H}]$, respectively. The large scatter of $[\text{Sr}/\text{Ba}]$ at lower metallicity is evident. The scatter is primarily caused by the dependence of $[\text{Sr}/\text{Ba}]$ on $[\text{Ba}/\text{H}]$ in $[\text{Ba}/\text{H}] > -4$ found in Figure 27(f), that reflects decreasing $[\text{Sr}/\text{Ba}]$ with increasing Ba by the r-process. The large scatter of $[\text{Sr}/\text{Ba}]$ found in objects with low Ba abundances ($[\text{Ba}/\text{H}] \lesssim -4$) is another factor.

Most of the stars have $[\text{Sr}/\text{Ba}]$ higher than the value of r-process component in solar-system material ($[\text{Sr}/\text{Ba}] = -0.4$). Objects with high abundances of heavy neutron-capture elements including Ba, which have $[\text{Ba}/\text{Eu}]$ explained by the r-process (panel b), have relatively low $[\text{Sr}/\text{Ba}]$ ratios close to the r-process value (panel f). This indicates that light neutron-capture elements including Sr in these stars are also originated from the r-process. On the other hand, many objects with lower Ba abundances ($[\text{Ba}/\text{H}] < -2$, see panel f) exhibit large scatter in $[\text{Sr}/\text{Ba}]$ ratios. To explain objects with high $[\text{Sr}/\text{Ba}]$, contributions of processes that efficiently produce light neutron-capture elements than r-process and main s-process (§ 3.1.6). We note that such processes could also have contributed to objects with stars with high $[\text{Ba}/\text{H}]$ ratios, however, the larger contributions of the r-process would dominate in $[\text{Sr}/\text{Ba}]$ ratios of these stars. The remaining small number of stars with $[\text{Sr}/\text{Ba}] < -0.4$ need different explanations. A possible source is the main s-process at low metallicity, for which production of large amount of heavy neutron-capture elements like Ba is expected (Aoki et al. 2013a). Indeed, about a half of objects with $[\text{Sr}/\text{Ba}] < -0.4$ are CEMP-s stars presented by triangles in the figure. Although no clear excess of C is found for the remaining stars, small contribution of the s-process is not excluded as a possible source of the low Sr/Ba ratios. Further studies for them based on better quality spectra will be useful to examine the possible contributions of the s-process.

Figure 28 shows histograms of the abundance ratios $[\text{Sr}/\text{Fe}]$ and $[\text{Ba}/\text{Fe}]$, as well as the average of the two values, of giants for the two metallicity ranges $[\text{Fe}/\text{H}] < -3.0$ and $-3.0 < [\text{Fe}/\text{H}] < -2.5$. In the higher metallicity range, both $[\text{Sr}/\text{Fe}]$ and $[\text{Ba}/\text{Fe}]$ have peaks of the distributions at around 0.0. We note that the peak is much sharper in $[\text{Sr}/\text{Fe}]$, and the distribution of $[\text{Ba}/\text{Fe}]$ shows longer tail toward higher values. By contrast, the $[\text{Ba}/\text{Fe}]$ distribution in $[\text{Fe}/\text{H}] < -3.0$ is significantly lower with a peak at around -1.0 . Although majority of stars have $[\text{Sr}/\text{Fe}] > -1$ even in this metallicity range, the distribution shows a tail toward lower $[\text{Sr}/\text{Fe}]$. The average of $[\text{Sr}/\text{Fe}]$ and $[\text{Ba}/\text{Fe}]$ shows more smooth distributions having peaks at around 0.0 and -0.7 for $-3.0 < [\text{Fe}/\text{H}] < -2.5$ and $[\text{Fe}/\text{H}] < -3.0$, respectively.

The difference of the distribution in $[\text{Fe}/\text{H}] < -3.0$ reflects the difference of the origins of these two neutron-capture elements. Ba in the metallicity range $-3.0 < [\text{Fe}/\text{H}] < -2.5$ would be mostly provided by the r-process (e.g., Ishimaru et al. 2015) with possible small contribution of the s-process. Their contributions would be smaller to stars with lower metallicity ($[\text{Fe}/\text{H}] < -3.0$), reflecting relatively long timescale of the evolution of progenitors. Sr is also produced by the r-process, however, it should have another source in the early universe for which many models of the production process and site have been proposed (e.g., Cowan et al. 2021, and references therein), resulting in higher $[\text{Sr}/\text{Fe}]$ ratios than $[\text{Ba}/\text{Fe}]$ in $[\text{Fe}/\text{H}] < -3.0$ as found in Figure 28.

There are relatively small number of stars that have very low Ba and/or Sr abundances. The numbers of stars having $[\text{Ba}/\text{Fe}] < -1.0$ and $[\text{Sr}/\text{Fe}] < -1.0$ are 29 and 16, respectively. Among them 13 stars have $[\text{Sr}/\text{Fe}] < -1.0$ and $[\text{Ba}/\text{Fe}] < -1.0$. All of them are red giants, and most of them are extremely metal-poor ($[\text{Fe}/\text{H}] \lesssim -3$). The frequency of these objects is, hence, higher than 10% in this metallicity range. The low, but non-zero, abundances of neutron-capture elements in these stars suggest the existence of a kind of neutron-capture reaction that operates as often as the process responsible for lighter elements (Roederer 2013), or small and ubiquitous pollution of r-process elements in the very early phase of chemical evolution.

4. SUMMARY AND CONCLUDING REMARKS

The joint project between LAMOST and Subaru has provided us with a homogeneous sample of 386 VMP stars with stellar parameters and abundances for more than 20 species that have been determined based on high-resolution spectra, and high-precision astrometry which is used to estimate the surface gravity for most objects. The sample covers a rather wide range in both metallicities and evolutionary status, and thus an unprecedentedly valuable sample to better constrain the Galactic chemical evolution models, as well as the production of elements in the early time.

Our abundance measurements mostly confirm the abundance trends and distributions found by previous studies, but provide some updates. We here summarize the results obtained by our abundance measurements.

- The Li abundances of main-sequence turnoff stars ($T_{\text{eff}} > 5500$ K) with $[\text{Fe}/\text{H}] > -2.5$ show a clear plateau with $A(\text{Li})=2.2$, whereas those with lower metallicity have lower values ($A(\text{Li})=2.0$ on average) showing possible decreasing trend with decreasing metallicity as found by previous studies. Red giants ($T_{\text{eff}} < 5500$ K) with $\log g \gtrsim 2$ have an almost constant value of $A(\text{Li})=1.0$ regardless of metallicity. More evolved giants with $\log g \lesssim 1.5$ do not show Li absorption features, except for an anomalously Li-enhanced object, suggesting additional

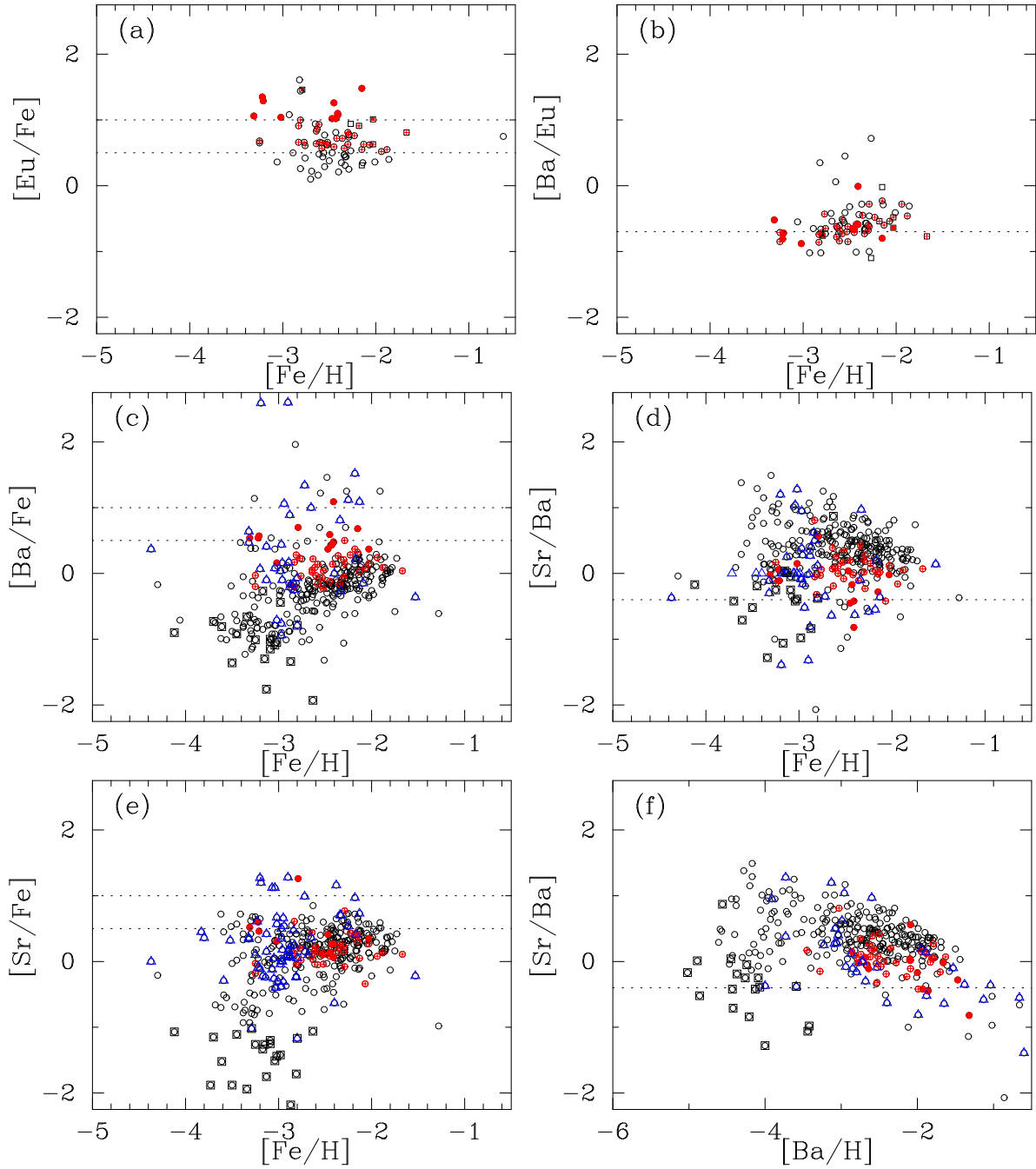


Figure 27. Abundance ratios of neutron-capture elements. Left panels: Abundance ratio with respect to Fe as a function of $[\text{Fe}/\text{H}]$ for Eu, Ba, and Sr. (a) Circles and squares mean turnoff and giant stars, respectively. r-II and r-I stars are shown by (red) filled symbols and (red) plus symbols, respectively. The dotted lines indicate the criteria of r-I and r-II stars. (c, e) r-I and r-II stars are shown by the same symbols as the top panel. CEMP stars and Ba-deficient stars ($[\text{Ba}/\text{Fe}] < -1$) are presented by overplotting large triangles and squares, respectively. Right panels: (b) $[\text{Ba}/\text{Eu}]$ as a function of $[\text{Fe}/\text{H}]$. The symbols are the same as for the panel for $[\text{Eu}/\text{Fe}]$. The dotted line indicates the value expected for the r-process. (d and f) $[\text{Sr}/\text{Ba}]$ as a function of $[\text{Fe}/\text{H}]$ and $[\text{Ba}/\text{H}]$, respectively. The symbols are the same as for the panel for $[\text{Ba}/\text{Fe}]$ and $[\text{Sr}/\text{Fe}]$ in the left panels. The dotted line is the value of the r-process component in solar-system material.

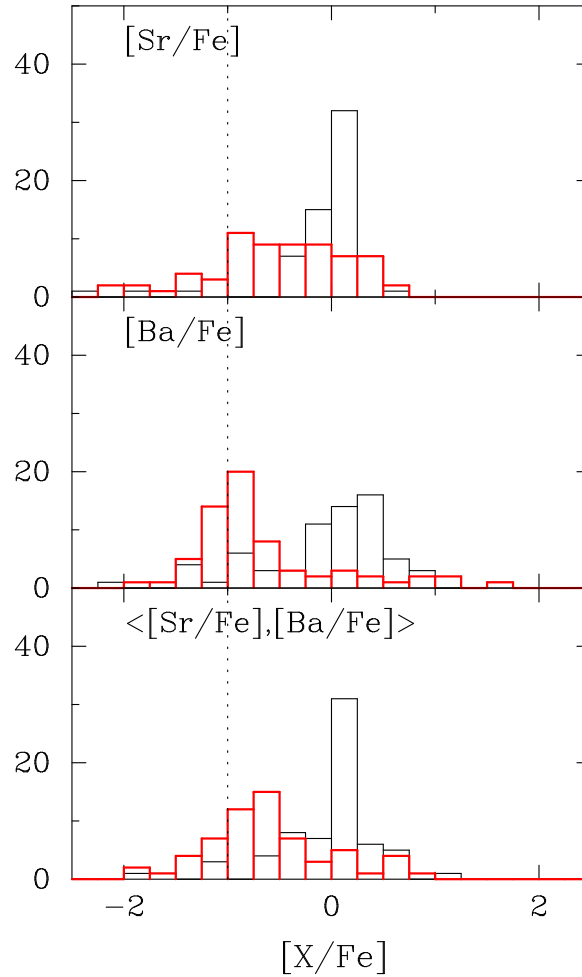


Figure 28. Distributions of $[\text{Sr}/\text{Fe}]$, $[\text{Ba}/\text{Fe}]$ and their average ($\langle [\text{Sr}/\text{Fe}], [\text{Ba}/\text{Fe}] \rangle$). Thin (black) and thick (red) lines mean those of stars with $-3.0 < [\text{Fe}/\text{H}] < -2.5$ and $[\text{Fe}/\text{H}] < -3.0$, respectively.

internal mixing in such highly evolved stars. Li is not detected in horizontal branch stars ($T_{\text{eff}} > 5500$ K and $\log g < 3.0$) in our sample.

- The frequency of CEMP stars ($[\text{C}/\text{Fe}]$) estimated from the main-sequence turnoff stars is 20–30%. The frequency of CEMP is much lower ($\sim 8\%$) in giants. The frequency of CEMP-s stars is much lower in giants as expected from dilution of carbon-enhanced material provided by companion AGB stars by the first dredge-up. The frequency of CEMP-no in giants are also lower than that in turnoff stars, although the difference is not as significant as found for CEMP-s stars. The CEMP-no stars with $0.7 < [\text{C}/\text{Fe}] < 1.0$ are not well separated from other (carbon-normal) stars, suggesting a continuous distribution of $[\text{C}/\text{Fe}]$ upto 1.0. This relatively small excess of carbon may disappear when they evolve to cool red giants by extra mixing.
- Over-abundances of α -elements (Mg, Si, Ca, and Ti) with respect to Fe in very metal-poor stars are confirmed. Among them, Mg (and Si) abundance ratios show a decreasing trend with increasing metallicity, which is not well reproduced by current Galactic chemical evolution models. Correlations of abundance ratios between Mg and Si and between Ca and Ti are found while the correlation between the two groups (Mg-Si and Ca-Ti) is weaker, suggesting

the enrichment processes are different between them to a certain extent. We have identified 12 low-Mg stars ($[\text{Mg}/\text{Fe}] < 0$) in a wide range of metallicity ($-3.8 < [\text{Fe}/\text{H}] < -1.7$). The over-abundances of Ti and Sc are not reproduced at all by current chemical evolution models, and some essential revision of nucleosynthesis modeling would be required to solve the discrepancy.

- The abundance ratios of iron-peak elements are approximately solar values, taking the possible NLTE effects into account for the Cr abundances derived for giants. An exception is Zn, which shows increasing trend with decreasing metallicity in $[\text{Fe}/\text{H}] < -2.5$. The high Zn abundance ratios, as well as the small over-abundances of Co, are not well reproduced by chemical evolution models.
- The frequency of r-process-enhanced stars (r-II stars) estimated from giants is about 5%, which agrees with previous estimates. The r-II stars with the most significant excess of Eu are found at $[\text{Fe}/\text{H}] \sim -3$, but r-II stars are also identified at higher metallicity ($[\text{Fe}/\text{H}] > -2.5$). Sr and Ba abundances show large dispersion, but their distribution is significantly different in $[\text{Fe}/\text{H}] < -3$, suggesting the existence of extra sources to produce Sr at such low metallicity.

This work provides the largest uniform sample of VMP stars with detailed chemical abundances, which should be a valuable data set for studies on the formation and evolution history of our Galaxy. The full data file of parameters and abundances presented in Table 2 and 3 will be available online. Combined with analysis of kinematic properties of this sample, which will be reported in the next paper of this series, we will be able to investigate the nature of these old stars and halo components of our Milky Way from a chemo-dynamical view, e.g., the relation between the accreted halo components and the decreasing trend with increasing metallicity for Mg (and Si) abundances.

ACKNOWLEDGMENTS

We thank the anonymous referee for the careful reading of the manuscript and useful comments. This research is based on data collected at Subaru Telescope, which is operated by the National Astronomical Observatory of Japan. We are honored and grateful for the opportunity of observing the Universe from Maunakea, which has the cultural, historical and natural significance in Hawaii. Guoshoujing Telescope (the Large Sky Area Multi-Object Fiber Spectroscopic Telescope, LAMOST) is a National Major Scientific Project built by the Chinese Academy of Sciences. Funding for the project has been provided by the National Development and Reform Commission. It is operated and managed by the National Astronomical Observatories, Chinese Academy of Sciences. This work was supported by the National Key R&D Program of China No.2019YFA0405502, the JSPS - CAS Joint Research Program, the National Natural Science Foundation of China grant Nos. 11988101, 11973049, and 11625313, and the science research grants from the China Manned Space Project with No. CMSCSST-2021-B05. H.L. and Q.X. acknowledge support from the Strategic Priority Research Program of Chinese Academy of Sciences, Grant No. XDB34020205 and the Youth Innovation Promotion Association of the CAS (id. Y202017 and 2020058). This work was also supported by a Grant-in-Aid for Scientific Research (KAKENHI) (JP16H02168, JP17K14249, JP19HP8019, JP20H05855, and JP20HP8012) from the Japan Society for the Promotion of Science.

Facilities: LAMOST, Subaru

REFERENCES

- Aguado, D. S., González Hernández, J. I., Allende Prieto, C., & Rebolo, R. 2017, *A&A*, 605, A40
— 2019, *ApJL*, 874, L21
- Aguado, D. S., et al. 2021, *MNRAS*, 500, 889
- Alonso, A., Arribas, S., & Martínez-Roger, C. 1996, *A&AS*, 117, 227
- Alonso, A., Arribas, S., & Martínez-Roger, C. 1999, *A&AS*, 140, 261
- Amarsi, A. M., Lind, K., Asplund, M., Barklem, P. S., & Collet, R. 2016, *MNRAS*, 463, 1518
- Andrievsky, S. M., Spite, M., Korotin, S. A., Spite, F., Bonifacio, P., Cayrel, R., Hill, V., & François, P. 2007, *A&A*, 464, 1081
- Aoki, W., Barklem, P. S., Beers, T. C., Christlieb, N., Inoue, S., García Pérez, A. E., Norris, J. E., & Carollo, D. 2009a, *ApJ*, 698, 1803
- Aoki, W., Beers, T. C., Christlieb, N., Norris, J. E., Ryan, S. G., & Tsangarides, S. 2007, *ApJ*, 655, 492
- Aoki, W., Matsuno, T., Honda, S., Ishigaki, M. N., Li, H., Suda, T., & Kumar, Y. B. 2018, *PASJ*, 70, 94
- Aoki, W., Norris, J. E., Ryan, S. G., Beers, T. C., & Ando, H. 2002, *PASJ*, 54, 933
- Aoki, W., Suda, T., Boyd, R. N., Kajino, T., & Famiano, M. A. 2013a, *ApJL*, 766, L13
- Aoki, W., Tominaga, N., Beers, T. C., Honda, S., & Lee, Y. S. 2014, *Science*, 345, 912
- Aoki, W., et al. 2009b, *A&A*, 502, 569
— 2013b, *AJ*, 145, 13
- Asplund, M., Grevesse, N., Sauval, A. J., & Scott, P. 2009, *ARA&A*, 47, 481
- Asplund, M., Lambert, D. L., Nissen, P. E., Primas, F., & Smith, V. V. 2006, *ApJ*, 644, 229
- Barklem, P. S., et al. 2005, *A&A*, 439, 129
- Beers, T. C., & Christlieb, N. 2005, *ARA&A*, 43, 531
- Beers, T. C., Preston, G. W., & Shectman, S. A. 1985, *AJ*, 90, 2089
— 1992, *AJ*, 103, 1987
- Bergemann, M., & Cescutti, G. 2010, *A&A*, 522, A9
- Bonifacio, P., et al. 2009, *A&A*, 501, 519
— 2018, *A&A*, 612, A65
- Borghs, G., de Bisschop, P., van Hove, M., & Silverans, R. E. 1983, *Hyperfine Interactions*, 15, 177
- Caffau, E., et al. 2011, *Nature*, 477, 67
— 2013, *A&A*, 560, A15
- Castelli, F., & Kurucz, R. L. 2003, in *IAU Symposium*, Vol. 210, *Modelling of Stellar Atmospheres*, ed. N. Piskunov, W. W. Weiss, & D. F. Gray, A20
- Cayrel, R., et al. 2004, *A&A*, 416, 1117
- Charbonnel, C., & Primas, F. 2005, *A&A*, 442, 961
- Chiaki, G., Tominaga, N., & Nozawa, T. 2017, *MNRAS*, 472, L115
- Chieffi, A., Limongi, M., & Straniero, O. 1998, *ApJ*, 502, 737
- Chopin, A., Hirschi, R., Meynet, G., Ekström, S., Chiappini, C., & Laird, A. 2018, *A&A*, 618, A133
- Christlieb, N., Gustafsson, B., Korn, A. J., Barklem, P. S., Beers, T. C., Bessell, M. S., Karlsson, T., & Mizuno-Wiedner, M. 2004, *ApJ*, 603, 708
- Christlieb, N., Schörck, T., Frebel, A., Beers, T. C., Wisotzki, L., & Reimers, D. 2008, *A&A*, 484, 721
- Christlieb, N., et al. 2002, *Nature*, 419, 904
- Cohen, J. G., Christlieb, N., Thompson, I., McWilliam, A., Shectman, S., Reimers, D., Wisotzki, L., & Kirby, E. 2013, *ApJ*, 778, 56
- Collet, R., Asplund, M., & Trampedach, R. 2006, *ApJL*, 644, L121
- Cowan, J. J., Sneden, C., Lawler, J. E., Aprahamian, A., Wiescher, M., Langanke, K., Martínez-Pinedo, G., & Thielemann, F.-K. 2021, *Reviews of Modern Physics*, 93, 015002
- Cristallo, S., Straniero, O., Piersanti, L., & Gobrecht, D. 2015, *ApJS*, 219, 40
- Cybert, R. H., Fields, B. D., Olive, K. A., & Yeh, T.-H. 2016, *Reviews of Modern Physics*, 88, 015004
- De Silva, G. M., et al. 2015, *MNRAS*, 449, 2604
- Ekström, S., Meynet, G., Chiappini, C., Hirschi, R., & Maeder, A. 2008, *A&A*, 489, 685
- Ezzeddine, R., et al. 2019, *ApJ*, 876, 97

- . 2020, *ApJ*, 898, 150
- Fields, B. D., Olive, K. A., Yeh, T.-H., & Young, C. 2020, *JCAP*, 2020, 010
- Fishlock, C. K., Karakas, A. I., Lugaro, M., & Yong, D. 2014, *ApJ*, 797, 44
- François, P., et al. 2007, *A&A*, 476, 935
- Frebel, A., Casey, A. R., Jacobson, H. R., & Yu, Q. 2013, *ApJ*, 769, 57
- Frebel, A., Collet, R., Eriksson, K., Christlieb, N., & Aoki, W. 2008, *ApJ*, 684, 588
- Frebel, A., & Norris, J. E. 2015, *ARA&A*, 53, 631
- Frebel, A., et al. 2005, *Nature*, 434, 871
- Fu, X., Bressan, A., Molaro, P., & Marigo, P. 2015, *MNRAS*, 452, 3256
- Gaia Collaboration et al. 2016, *A&A*, 595, A1
- . 2018, *A&A*, 616, A1
- . 2021, *A&A*, 649, A1
- Gallagher, A. J., Caffau, E., Bonifacio, P., Ludwig, H. G., Steffen, M., Homeier, D., & Plez, B. 2017, *A&A*, 598, L10
- Gao, X., et al. 2020, *MNRAS*, 497, L30
- Gilmore, G., et al. 2012, *The Messenger*, 147, 25
- Goswami, A., & Prantzos, N. 2000, *A&A*, 359, 191
- Gratton, R. G., Sneden, C., Carretta, E., & Bragaglia, A. 2000, *A&A*, 354, 169
- Hansen, T. T., Andersen, J., Nordström, B., Beers, T. C., Placco, V. M., Yoon, J., & Buchhave, L. A. 2016a, *A&A*, 586, A160
- . 2016b, *A&A*, 588, A3
- Hansen, T. T., et al. 2020, *ApJ*, 897, 183
- Hartwig, T., Ishigaki, M. N., Klessen, R. S., & Yoshida, N. 2019, *MNRAS*, 482, 1204
- Hartwig, T., & Yoshida, N. 2019, *ApJL*, 870, L3
- Heger, A., & Woosley, S. E. 2010, *ApJ*, 724, 341
- Helmi, A., Babusiaux, C., Koppelman, H. H., Massari, D., Veljanoski, J., & Brown, A. G. A. 2018, *Nature*, 563, 85
- Helmi, A., White, S. D. M., de Zeeuw, P. T., & Zhao, H. 1999, *Nature*, 402, 53
- Hirai, Y., Ishimaru, Y., Saitoh, T. R., Fujii, M. S., Hidaka, J., & Kajino, T. 2015, *ApJ*, 814, 41
- Hirai, Y., Saitoh, T. R., Ishimaru, Y., & Wanajo, S. 2018, *ApJ*, 855, 63
- Hirschi, R. 2007, *A&A*, 461, 571
- Hollek, J. K., Frebel, A., Roederer, I. U., Sneden, C., Shetrone, M., Beers, T. C., Kang, S.-j., & Thom, C. 2011, *ApJ*, 742, 54
- Holmbeck, E. M., et al. 2020, *ApJS*, 249, 30
- Honda, S., Aoki, W., Kajino, T., Ando, H., Beers, T. C., Izumiura, H., Sadakane, K., & Takada-Hidai, M. 2004a, *ApJ*, 607, 474
- Honda, S., et al. 2004b, *ApJS*, 152, 113
- Ibata, R. A., Gilmore, G., & Irwin, M. J. 1994, *Nature*, 370, 194
- Iben, Icko, J. 1967, *ApJ*, 147, 624
- Ishimaru, Y., Wanajo, S., & Prantzos, N. 2015, *ApJL*, 804, L35
- Ivans, I. I., Sneden, C., James, C. R., Preston, G. W., Fulbright, J. P., Höflich, P. A., Carney, B. W., & Wheeler, J. C. 2003, *ApJ*, 592, 906
- Iwamoto, K., Brachwitz, F., Nomoto, K., Kishimoto, N., Umeda, H., Hix, W. R., & Thielemann, F.-K. 1999, *ApJS*, 125, 439
- Jacobson, H. R., et al. 2015, *ApJ*, 807, 171
- Ji, A. P., Frebel, A., Chiti, A., & Simon, J. D. 2016, *Nature*, 531, 610
- Jones, S., Côté, B., Röpke, F. K., & Wanajo, S. 2019, *ApJ*, 882, 170
- Kang, W., & Lee, S.-G. 2012, *MNRAS*, 425, 3162
- Karakas, A. I. 2010, *MNRAS*, 403, 1413
- Karakas, A. I., Lugaro, M., Carlos, M., Cseh, B., Kamath, D., & García-Hernández, D. A. 2018, *MNRAS*, 477, 421
- Keller, S. C., et al. 2007, *PASA*, 24, 1
- . 2014, *Nature*, 506, 463
- Kobayashi, C., Ishigaki, M. N., Tominaga, N., & Nomoto, K. 2014, *ApJL*, 785, L5
- Kobayashi, C., Karakas, A. I., & Lugaro, M. 2020, *ApJ*, 900, 179
- Kobayashi, C., Karakas, A. I., & Umeda, H. 2011, *MNRAS*, 414, 3231
- Kobayashi, C., & Nomoto, K. 2009, *ApJ*, 707, 1466
- Kobayashi, C., Nomoto, K., & Hachisu, I. 2015, *ApJL*, 804, L24
- Kobayashi, C., Tsujimoto, T., Nomoto, K., Hachisu, I., & Kato, M. 1998, *ApJL*, 503, L155
- Kobayashi, C., Umeda, H., Nomoto, K., Tominaga, N., & Ohkubo, T. 2006, *ApJ*, 653, 1145
- Koch, A., McWilliam, A., Grebel, E. K., Zucker, D. B., & Belokurov, V. 2008, *ApJL*, 688, L13
- Koppelman, H. H., Helmi, A., Massari, D., Price-Whelan, A. M., & Starkenburg, T. K. 2019, *A&A*, 631, L9
- Korn, A. J., Grundahl, F., Richard, O., Barklem, P. S., Mashonkina, L., Collet, R., Piskunov, N., & Gustafsson, B. 2006, *Nature*, 442, 657

- Kroupa, P. 2002, *Science*, 295, 82
- Kroupa, P. 2008, in *Astronomical Society of the Pacific Conference Series*, Vol. 390, *Pathways Through an Eclectic Universe*, ed. J. H. Knapen, T. J. Mahoney, & A. Vazdekis, 3
- Kubryk, M., Prantzos, N., & Athanassoula, E. 2015, *A&A*, 580, A127
- Kumar, Y. B., Reddy, B. E., Campbell, S. W., Maben, S., Zhao, G., & Ting, Y.-S. 2020, *Nature Astronomy*, 4, 1059
- Lai, D. K., Bolte, M., Johnson, J. A., Lucatello, S., Heger, A., & Woosley, S. E. 2008, *ApJ*, 681, 1524
- Lawler, J. E., Bonvallet, G., & Sneden, C. 2001a, *ApJ*, 556, 452
- Lawler, J. E., Wickliffe, M. E., den Hartog, E. A., & Sneden, C. 2001b, *ApJ*, 563, 1075
- Lee, Y. S., Beers, T. C., Kim, Y. K., Placco, V., Yoon, J., Carollo, D., Masseron, T., & Jung, J. 2017, *ApJ*, 836, 91
- Li, H., Aoki, W., Matsuno, T., Bharat Kumar, Y., Shi, J., Suda, T., & Zhao, G. 2018a, *ApJL*, 852, L31
- Li, H., Aoki, W., Zhao, G., Honda, S., Christlieb, N., & Suda, T. 2015a, *PASJ*, 67, 84
- Li, H., Tan, K., & Zhao, G. 2018b, *ApJS*, 238, 16
- Li, H.-N., Aoki, W., Honda, S., Zhao, G., Christlieb, N., & Suda, T. 2015b, *Research in Astronomy and Astrophysics*, 15, 1264
- Li, H.-N., Zhao, G., Christlieb, N., Wang, L., Wang, W., Zhang, Y., Hou, Y., & Yuan, H. 2015c, *ApJ*, 798, 110
- Limongi, M., & Chieffi, A. 2012, *ApJS*, 199, 38
- , 2018, *ApJS*, 237, 13
- Lind, K., Asplund, M., Barklem, P. S., & Belyaev, A. K. 2011, *A&A*, 528, A103
- Lind, K., Bergemann, M., & Asplund, M. 2012, *MNRAS*, 427, 50
- Lind, K., Primas, F., Charbonnel, C., Grundahl, F., & Asplund, M. 2009, *A&A*, 503, 545
- Liu, X.-W., Zhao, G., & Hou, J.-L. 2015, *Research in Astronomy and Astrophysics*, 15, 1089
- Lugaro, M., Karakas, A. I., Stancliffe, R. J., & Rijs, C. 2012, *ApJ*, 747, 2
- Maeder, A., Meynet, G., & Chiappini, C. 2015, *A&A*, 576, A56
- Mardini, M. K., et al. 2020, *ApJ*, 903, 88
- Mashonkina, L., Christlieb, N., Barklem, P. S., Hill, V., Beers, T. C., & Velichko, A. 2010, *A&A*, 516, A46
- Masseron, T., Johnson, J. A., Lucatello, S., Karakas, A., Plez, B., Beers, T. C., & Christlieb, N. 2012, *ApJ*, 751, 14
- Matsuno, T., Aoki, W., Beers, T. C., Lee, Y. S., & Honda, S. 2017a, *AJ*, 154, 52
- Matsuno, T., Aoki, W., & Suda, T. 2019, *ApJL*, 874, L35
- Matsuno, T., Aoki, W., Suda, T., & Li, H. 2017b, *PASJ*, 69, 24
- McWilliam, A., Preston, G. W., Sneden, C., & Searle, L. 1995, *AJ*, 109, 2757
- Meléndez, J., Casagrande, L., Ramírez, I., Asplund, M., & Schuster, W. J. 2010, *A&A*, 515, L3
- Meynet, G., Ekström, S., & Maeder, A. 2006, *A&A*, 447, 623
- Mucciarelli, A., Salaris, M., & Bonifacio, P. 2012, *MNRAS*, 419, 2195
- Mucciarelli, A., Salaris, M., Monaco, L., Bonifacio, P., Fu, X., & Villanova, S. 2018, *A&A*, 618, A134
- Myeong, G. C., Evans, N. W., Belokurov, V., Sanders, J. L., & Koposov, S. E. 2018, *ApJL*, 856, L26
- Naidu, R. P., Conroy, C., Bonaca, A., Johnson, B. D., Ting, Y.-S., Caldwell, N., Zaritsky, D., & Cargile, P. A. 2020, *ApJ*, 901, 48
- Nissen, P. E., & Schuster, W. J. 2010, *A&A*, 511, L10
- Nomoto, K., Kobayashi, C., & Tominaga, N. 2013, *ARA&A*, 51, 457
- Norris, J. E., Ryan, S. G., Beers, T. C., Aoki, W., & Ando, H. 2002, *ApJL*, 569, L107
- Norris, J. E., Ryan, S. G., & Stringfellow, G. S. 1994, *ApJ*, 423, 386
- Norris, J. E., & Yong, D. 2019, *ApJ*, 879, 37
- Norris, J. E., et al. 2013, *ApJ*, 762, 25
- Osorio, Y., & Barklem, P. S. 2016, *A&A*, 586, A120
- Placco, V. M., Frebel, A., Beers, T. C., Christlieb, N., Lee, Y. S., Kennedy, C. R., Rossi, S., & Santucci, R. M. 2014a, *ApJ*, 781, 40
- Placco, V. M., Frebel, A., Beers, T. C., & Stancliffe, R. J. 2014b, *ApJ*, 797, 21
- Prantzos, N., Abia, C., Limongi, M., Chieffi, A., & Cristallo, S. 2018, *MNRAS*, 476, 3432
- Reggiani, H., Meléndez, J., Kobayashi, C., Karakas, A., & Placco, V. 2017, *A&A*, 608, A46
- Richard, O. 2012, *Memorie della Societa Astronomica Italiana Supplementi*, 22, 211

- Richard, O., Michaud, G., & Richer, J. 2005, *ApJ*, 619, 538
- Roederer, I. U. 2013, *AJ*, 145, 26
- Roederer, I. U., & Barklem, P. S. 2018, *ApJ*, 857, 2
- Roederer, I. U., & Gnedin, O. Y. 2019, *ApJ*, 883, 84
- Roederer, I. U., Preston, G. W., Thompson, I. B., Shectman, S. A., Sneden, C., Burley, G. S., & Kelson, D. D. 2014, *AJ*, 147, 136
- Roederer, I. U., Sakari, C. M., Placco, V. M., Beers, T. C., Ezzeddine, R., Frebel, A., & Hansen, T. T. 2018, *ApJ*, 865, 129
- Roederer, I. U., et al. 2012, *ApJL*, 747, L8
- 2016, *AJ*, 151, 82
- Romano, D., Karakas, A. I., Tosi, M., & Matteucci, F. 2010, *A&A*, 522, A32
- Ruiz-Lara, T., Matsuno, T., Sofie Lövdal, S., Helmi, A., Dodd, E., & Koppelman, H. H. 2022, arXiv e-prints, arXiv:2201.02405
- Ryan, S. G., Norris, J. E., & Beers, T. C. 1999, *ApJ*, 523, 654
- Sakari, C. M., et al. 2018, *ApJ*, 868, 110
- 2019, *ApJ*, 874, 148
- Salvadori, S., Bonifacio, P., Caffau, E., Korotin, S., Andreevsky, S., Spite, M., & Skúladóttir, Á. 2019, *MNRAS*, 487, 4261
- Salvadori, S., Skúladóttir, Á., & Tolstoy, E. 2015, *MNRAS*, 454, 1320
- Sbordone, L., et al. 2010, *A&A*, 522, A26
- Sestito, F., et al. 2019, *MNRAS*, 484, 2166
- 2020, *MNRAS*, 497, L7
- 2021, *MNRAS*, 500, 3750
- Shetrone, M., Venn, K. A., Tolstoy, E., Primas, F., Hill, V., & Kaufer, A. 2003, *AJ*, 125, 684
- Shetrone, M., et al. 2019, *ApJ*, 872, 137
- Simmerer, J., Sneden, C., Cowan, J. J., Collier, J., Woolf, V. M., & Lawler, J. E. 2004, *ApJ*, 617, 1091
- Sitnova, T. M., Mashonkina, L. I., & Ryabchikova, T. A. 2016, *MNRAS*, 461, 1000
- Sneden, C. 1973, *ApJ*, 184, 839
- Sneden, C., et al. 2003, *ApJ*, 591, 936
- Sobeck, J. S., Lawler, J. E., & Sneden, C. 2007, *ApJ*, 667, 1267
- Sobeck, J. S., et al. 2011, *AJ*, 141, 175
- Spite, F., & Spite, M. 1982, *A&A*, 115, 357
- Spite, M., et al. 2005, *A&A*, 430, 655
- 2006, *A&A*, 455, 291
- Stancliffe, R. J., Glebbeek, E., Izzard, R. G., & Pols, O. R. 2007, *A&A*, 464, L57
- Starkenbug, E., et al. 2017, *MNRAS*, 471, 2587
- Suda, T., Aikawa, M., Machida, M. N., Fujimoto, M. Y., & Iben, Jr., I. 2004, *ApJ*, 611, 476
- Suda, T., Yamada, S., Katsuta, Y., Komiya, Y., Ishizuka, C., Aoki, W., & Fujimoto, M. Y. 2011, *MNRAS*, 412, 843
- Suda, T., et al. 2008, *PASJ*, 60, 1159
- 2017, *PASJ*, 69, 76
- Takahashi, K., Yoshida, T., & Umeda, H. 2018, *ApJ*, 857, 111
- Takeda, Y. 2019, *A&A*, 622, A107
- Thorburn, J. A. 1994, *ApJ*, 421, 318
- Tolstoy, E., Hill, V., & Tosi, M. 2009, *ARA&A*, 47, 371
- Tominaga, N. 2009, *ApJ*, 690, 526
- Tominaga, N., Iwamoto, N., & Nomoto, K. 2014, *ApJ*, 785, 98
- Tominaga, N., Umeda, H., & Nomoto, K. 2007, *ApJ*, 660, 516
- Travaglio, C., Gallino, R., Arnone, E., Cowan, J., Jordan, F., & Sneden, C. 2004, *ApJ*, 601, 864
- Umeda, H., & Nomoto, K. 2002, *ApJ*, 565, 385
- 2005, *ApJ*, 619, 427
- Venn, K. A., et al. 2012, *ApJ*, 751, 102
- 2020, *MNRAS*, 492, 3241
- Wanajo, S. 2018, *ApJ*, 868, 65
- Wanajo, S., & Ishimaru, Y. 2006, *NuPhA*, 777, 676
- Woosley, S. E., & Weaver, T. A. 1995, *ApJS*, 101, 181
- Xing, Q.-F., Zhao, G., Aoki, W., Honda, S., Li, H.-N., Ishigaki, M. N., & Matsuno, T. 2019, *Nature Astronomy*, 3, 631
- Yamada, S., Suda, T., Komiya, Y., Aoki, W., & Fujimoto, M. Y. 2013, *MNRAS*, 436, 1362
- Yan, H.-L., et al. 2021, *Nature Astronomy*, 5, 86
- Yanny, B., et al. 2009, *AJ*, 137, 4377
- Yong, D., et al. 2013, *ApJ*, 762, 26
- 2021a, *MNRAS*, 507, 4102
- 2021b, *Nature*, 595, 223
- Yoon, J., et al. 2016, *ApJ*, 833, 20
- Yuan, Z., et al. 2020, *ApJ*, 891, 39
- Zhang, S., Li, H., Zhao, G., Aoki, W., & Matsuno, T. 2019, *PASJ*, 71, 89
- Zhao, G., & Chen, Y. 2021, *Science China Physics, Mechanics, and Astronomy*, 64, 239562

Zhao, G., Chen, Y., Shi, J., Liang, Y., Hou, J.,
Chen, L., Zhang, H., & Li, A. 2006, Chinese
Journal of Astronomy and Astrophysics, 6, 265
Zhao, G., & Magain, P. 1991, A&A, 244, 425

Zhao, G., Zhao, Y.-H., Chu, Y.-Q., Jing, Y.-P., &
Deng, L.-C. 2012, Research in Astronomy and
Astrophysics, 12, 723

APPENDIX

A. VALIDATION OF STELLAR PARAMETERS DERIVED FROM LAMOST

Comparisons of stellar parameters derived from Subaru/HDS and LAMOST low-resolution spectra can be helpful to understand the efficiency of VMP selection from the LAMOST database, which has been shown in Figure 3 for the effective temperature. Here the comparison for $\log g$ and $[\text{Fe}/\text{H}]$ are shown in Figure 29. As can be seen in the bottom panels, rather good agreement can be found for $[\text{Fe}/\text{H}]$ with a small offset and reasonably low measurement uncertainty of -0.05 ± 0.26 dex. Rather good consistency can be found even at the extremely low metallicity region. Agreement of the surface gravity is also good in general, showing a very small offset of -0.04 , which is mostly because that the parallax-derived surface gravity has been adopted as the initial guess for most of the program stars to derive stellar parameters from LAMOST spectra. The relatively large scatter of the uncertainty for $\log g$ (~ 0.39) is not unexpected, since even with high-resolution spectroscopy, the uncertainty in estimating surface gravity is relatively large compared to T_{eff} and $[\text{Fe}/\text{H}]$, for objects that have no parallax measurements. However, the surface gravity estimated based on LAMOST spectra is generally consistent with the high-resolution analyses, which is sufficient to separate stars located in different evolutionary stages. Involving parallaxes obtained from further *Gaia* data releases will help improve the accuracy of $\log g$ estimates based on LAMOST low-resolution spectra. To sum, the stellar parameters derived from LAMOST low-resolution spectra are generally robust and reliable for a large sample of VMP and EMP stars.

B. UPDATING THE SURFACE GRAVITY WITH GAIA EDR3

Gaia has just published its latest data release, EDR3 (Gaia Collaboration et al. 2021), which provides more accurate measurements on the parallax and proper motion for Galactic stars. Although the main purpose of this paper is exploring the chemical abundances, it is still necessary to understand how much the results would be affected (mainly on $\log g$) if the new parallax measurement is adopted. Therefore, we have cross-matched our sample with Gaia EDR3, and found that there could be 43 objects (mostly giants) whose $\log g$ have been derived based on the correction described in Section 2.2 now have reliable parallax measurement from Gaia EDR3. Comparisons of the two sets of $\log g$ based on Gaia DR2 and EDR3 are shown in Figure 30.

As for objects whose $\log g$ have been derived from parallax, DR2 and EDR3 are in good agreement, e.g., with an average difference of 0.01 ± 0.07 as shown in the right panel of Figure 30. Larger difference can be seen for objects for which the $\log g$ correction has been adopted. The DR2-based-corrected and EDR3-parallax-derived $\log g$ are in general consistent for the majority of the 43 objects with reliable parallax measurements from EDR3, i.e., the dashed distribution in red in the right panel of Figure 30. There are ten program stars showing a difference larger than 0.3 between the adopted (Gaia DR2-based) and the EDR3-based $\log g$, which are marked in red in the left panel, and all of them are more distant than 6 kpc (based on the EDR3 parallax).

As can be seen from the right panel of Figure 30, It will only be the ten program stars (“spec-component2”) that could have noticeably different $\log g$ if the EDR3 parallax is adopted. While for the majority of our sample, including the 315 objects that have parallax-derived $\log g$ (“plx-derived”) and 59 objects with corrected spectroscopic $\log g$ (“spec-component1”), the stellar parameters would

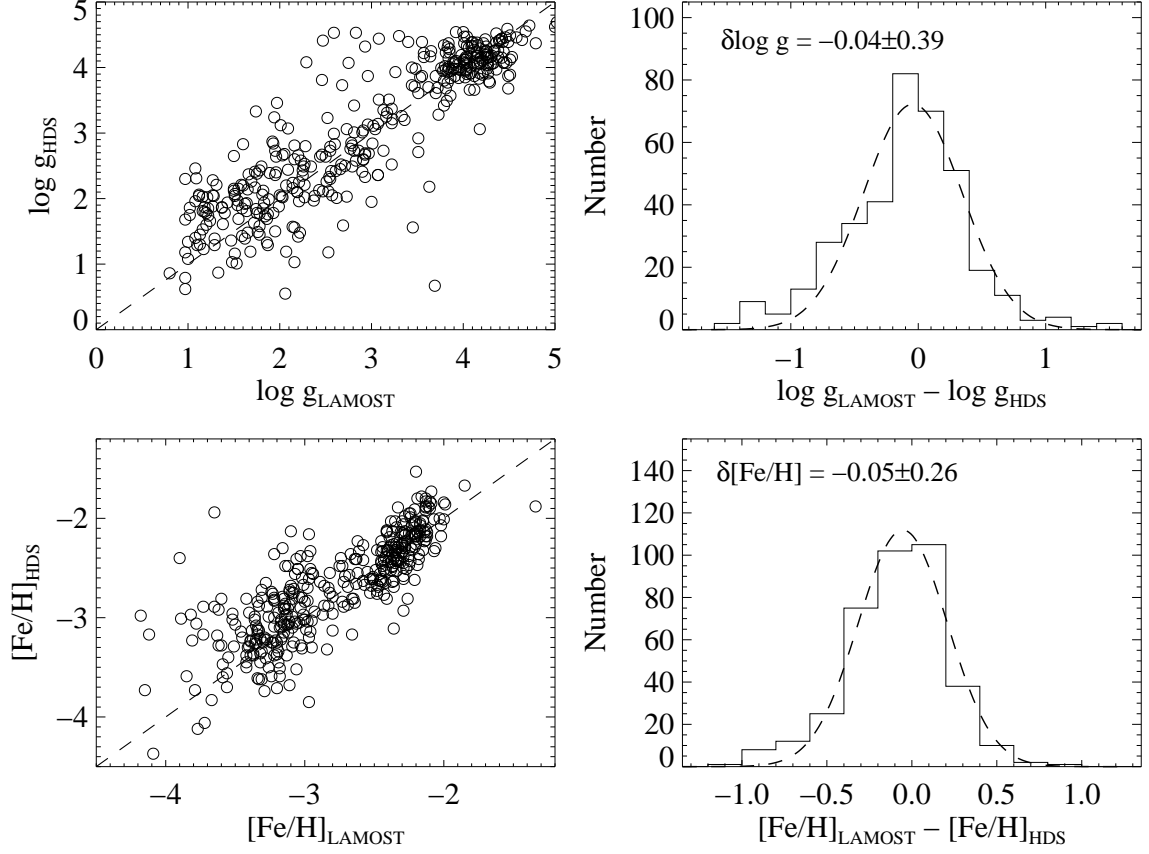


Figure 29. Top left: Comparison between $\log g$ derived from the LAMOST low-resolution spectra and that from Subaru/HDS spectra as adopted in this paper, i.e. including parallax-derived $\log g$ for 315 objects and corrected spectroscopic $\log g$ for 70 program stars. The one-to-one line is also plotted for reference. Top right: Distribution of the $\log g$ difference, together with a best-fit Gaussian to indicate the measurement error. The bottom panels are similar, but for comparison of the metallicity.

not vary much, e.g., with a change smaller or comparable to the uncertainty for $\log g$. According to the error budget estimation in § 2.4, even for objects whose uncertainty in $\log g$ is as large as 0.30, the resulted variation in abundances is smaller than the total uncertainty of abundances. We therefore decide to keep the $\log g$ estimation based on DR2 parallax measurement for current work. For the next paper of this series, which is going to study the kinematics of the sample, the latest version of Gaia measurement shall be used.

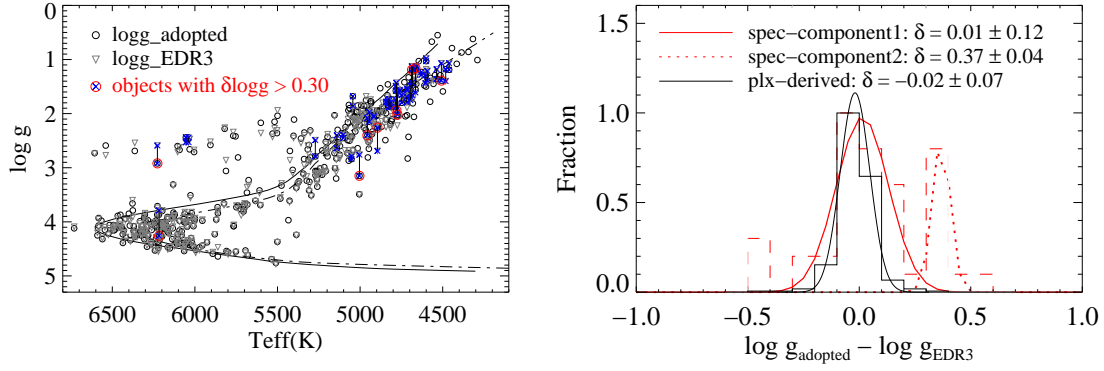


Figure 30. Left: comparison of the adopted $\log g$ (circle) and those derived from the parallax from *Gaia* EDR3 (triangle). Open symbols represent objects for which $\log g$ is directly derived from the parallax, and crosses stand for those whose $\log g$ is corrected from the spectroscopic result. Two values of $\log g$ are connected for the 43 objects which have reliable parallax measurements in EDR3 but not in DR2. Ten program stars whose EDR3-based $\log g$ differ from the DR2-based values with more than 0.3 has been marked out with a large red circle. Right: difference of the two sets of $\log g$. Solid histogram refer to the distribution of the parallax-derived sub-sample, and the dashed histogram refers to that of spectroscopic-corrected $\log g$ sub-sample. Note that the latter can be fit with two Gaussian distributions (dashed for component 1 and dotted for component 2), with the typical offset and dispersion shown on the top of the panel.